3-22-2012

Desensitizing Flame Structure and Exhaust Emissions to Flow Parameters in an Ultra-Compact Combuster

Adam K. Parks

DESENSITIZING FLAME STRUCTURE AND EXHAUST EMISSIONS TO FLOW PARAMETERS IN AN ULTRA-COMPACT COMBUSTOR

THESIS

Adam K. Parks, Captain, USAF

AFIT/GAE/ENY/12-M33

DEPARTMENT OF THE AIR FORCE
AIR UNIVERSITY
AIR FORCE INSTITUTE OF TECHNOLOGY

Wright-Patterson Air Force Base, Ohio

AFIT/GAE/ENY/12-M33

DESENSITIZING FLAME STRUCTURE AND EXHAUST EMISSIONS TO FLOW PARAMETERS IN AN ULTRA-COMPACT COMBUSTOR

THESIS

Presented to the Faculty

Department of Aeronautics and Astronautics

Graduate School of Engineering and Management

Air Force Institute of Technology

Air University

Air Education and Training Command

In Partial Fulfillment of the Requirements for the

Degree of Master of Science in Aeronautical Engineering

Adam K. Parks

Captain, USAF

March 2012

AFIT/GAE/ENY/12-M33

DESENSITIZING FLAME STRUCTURE AND EXHAUST EMISSIONS TO FLOW PARAMETERS IN AN ULTRA-COMPACT COMBUSTOR

Adam K. Parks

Captain, USAF

Approved:

_____	_____
M. Polanka, PhD (Chairman)	date
_____	_____
M. Reeder, PhD (Member)	date
_____	_____
Capt J. Rutledge, PhD (Member)	date

Abstract

A major thrust of turbine engine research is to improve both efficiency and thrust-to-weight ratio of the engine. A promising solution to this challenge is the Ultra-Compact Combustor (UCC). The UCC shortens the axial length of the combustor by performing combustion circumferentially on the outer diameter of the engine. The reduction in axial length yields significant weight savings and increases the thrust-to-weight ratio. The design also increases combustion efficiency by performing the combustion in a centrifugally loaded environment which allows unreacted particles to remain in the combustor sufficiently long enough to become combustion products. The Air Force Institute of Technology (AFIT) and the Air Force Research Laboratory (AFRL) have been jointly researching the fundamental dynamics of the UCC. To aid in integrating the UCC into a turbine engine, the current objective is to desensitize the exhaust characteristics of the combustor to changes in operating parameters. The following report documents modifications to the AFIT sectional test rig to improve its replication of the AFRL full annulus. High speed video was captured to document flame shape, location, intensity, and stability within the core section. Carbon monoxide, carbon dioxide, oxygen, nitrous oxides, and unburnt hydrocarbon emissions measurements were recorded to quantify the combustors exhaust constituents. A novel vane concept was implemented to desensitize the flame shape, location, intensity, and its exhaust products with changes in operating parameters. The design represents the next step toward creating a UCC vane that can migrate the flow effectively and consistently from the UCC cavity into the core flow. Furthermore, this vane concept represents the first attempt at a design that can be effectively cooled for application in a realistic turbine engine.

Acknowledgements

First, I would like to thank my advisor, Dr. Marc D. Polanka, for giving me the opportunity to work on this project. I appreciate his technical insights, guidance, and the freedom he offered me to explore my particular interests. I would also like to thank Dr. Kenneth LeBay for his technical assistance into my project. Dr. LeBay provided much needed depth not only about the laboratory and its capabilities but also the previous research that had occurred in the laboratory.

I would like to thank Mr. Jacob Wilson for his continuous help with component modeling and drawings. Mr. Wilson's help in getting test equipment fabricated from the model shop was instrumental in my research being accomplished. I would like to thank Mr. John Hixenbaugh for his unending assistance in purchasing supplies and equipment as well as his technical expertise in the laboratory. Without Mr. Wilson and Mr. Hixenbaugh's assistance, my research would never have been accomplished.

I would like to thank my parents, Mr. Russell Parks and Mrs. Janice Parks, for inspiring me to always do my best. They have always provided the best opportunities for me, and I appreciate their love and support during this undertaking.

Finally and most importantly, I would like to thank my wife, Megan, for enduring with my late nights, stress, and hardheadedness with grace and poise. I appreciate all of her patience, love, and support she's given me in order to allow me to succeed in my endeavors.

Adam K. Parks

Table of Contents

Page

List of Figures

List of Tables

Table Page

List of Symbols

List of Abbreviations

DESENSITIZING FLAME STRUCTURE AND EXHAUST EMISSIONS TO FLOW PARAMETERS IN AN ULTRA-COMPACT COMBUSTOR

I. Introduction

1.1 Ultra-Compact Combustor

The principles in designing axial turbine engine combustors have remained relatively constant since the introduction of the jet engine in 1929. A typical modern combustor diffuses compressed, straightened air to a Mach number near 0.1. The air then passes through a combustion chamber where it fully oxidizes the fuel. The combustion products then enter the high-pressure turbine inlet guide vanes (IGV) on their way to the high-pressure turbine. A typical modern combustor generally completes the combustion process at a fuel-to-air ratio less than stoichiometric [1]. Therefore, the length of the combustor must be merely long enough to allow the fuel to mix with incoming air, evaporate, and completely combust before reaching the turbine IGV.

Combustion and turbine engine efficiency is largely dependent on the turbine inlet temperature (T_{T4}). As T_{T4} increases, engine efficiency also increases. Over the last 60 years, material and coating improvements have allowed the turbine blades to be exposed to increasingly high temperatures. Accordingly, the increased T_{T4} allowed the combustor to operate at higher temperatures, thus increasing the combustors efficiency [1]. Advancements in manufacturing capabilities allow complex turbine blade film cooling schemes to be developed. The film cooling schemes enable the turbine blades to exceed the materials and coatings failure temperatures. Again, this has allowed the combustor to increase its operating temperature and efficiency. Improving engine efficiency helps meet the current military and commercial requirements for reduced turbine engine

emissions, but it does little to meet improved thrust-to-weight ratio demands. In an effort to meet the desired thrust-to-weight ratios, turbine engine combustors are becoming shorter and lighter [2]. One potential solution to the improved thrust-to-weight ratio, increased T_{T4}, and increased efficiency requirements is the Ultra-Compact Combustor (UCC). The Air Force Research Laboratory (AFRL) and the Air Force Institute of Technology (AFIT) have been jointly developing the UCC. This revolutionary design shortens the axial length of the combustor by combining the outlet guide vane of the compressor with the turbine IGV into a combined vane. The combustion process is then completed in a circumferential cavity above the combined vanes. Figure 1.1 qualitatively represents the reduced axial length on a modern turbine engine. The UCC achieves the necessary resident distance to complete the combustion process by forcing the reactions to occur on the outer diameter (OD) of the engine. It is estimated that by joining the two guide vanes into a combined vane and reacting circumferentially above this vane, the UCC could be 66% shorter than a traditional combustor [2, 3]. Inherent in the reduced length is a significant weight savings.

One method of inducing the swirled flow in the circumferential cavity is to inject air and fuel along the OD of the engine. By traveling along the OD, the combustion process is subject to a centrifugal force as the flow's tangential velocity vector is constantly changing. The centrifugal force, commonly referred to as a gravitational loading (g-loading) provides two benefits to the combustion process. First, g-loading above a minimum threshold increases combustion flame speeds as reported by Lewis [4] in 1973. The increased flame speeds are indicative of increased reaction rates, which allow a decreased combustor volume for the same mass flow. The second benefit comes

from the buoyancy phenomenon. The heavier particles (unburned fuel, cool air, etc.) are pulled to the OD of the circumferential cavity. This allows unreacted particles to remain in the circumferential cavity until these particles can combust. The lighter, combusted particles are pushed to the inner diameter (ID) of the section causing a density gradient to be established in the circumferential cavity. The buoyancy effect then forces the lighter particles to exit into the core section in between the guide vanes. The unreacted particles remain in the circumferential cavity sufficiently long enough for them to react and become combustion products. Theoretically, the unreacted particles experience an infinite residence time within the circumferential cavity, allowing the UCC to occupy a fraction of the traditional combustor volume in a turbine engine.

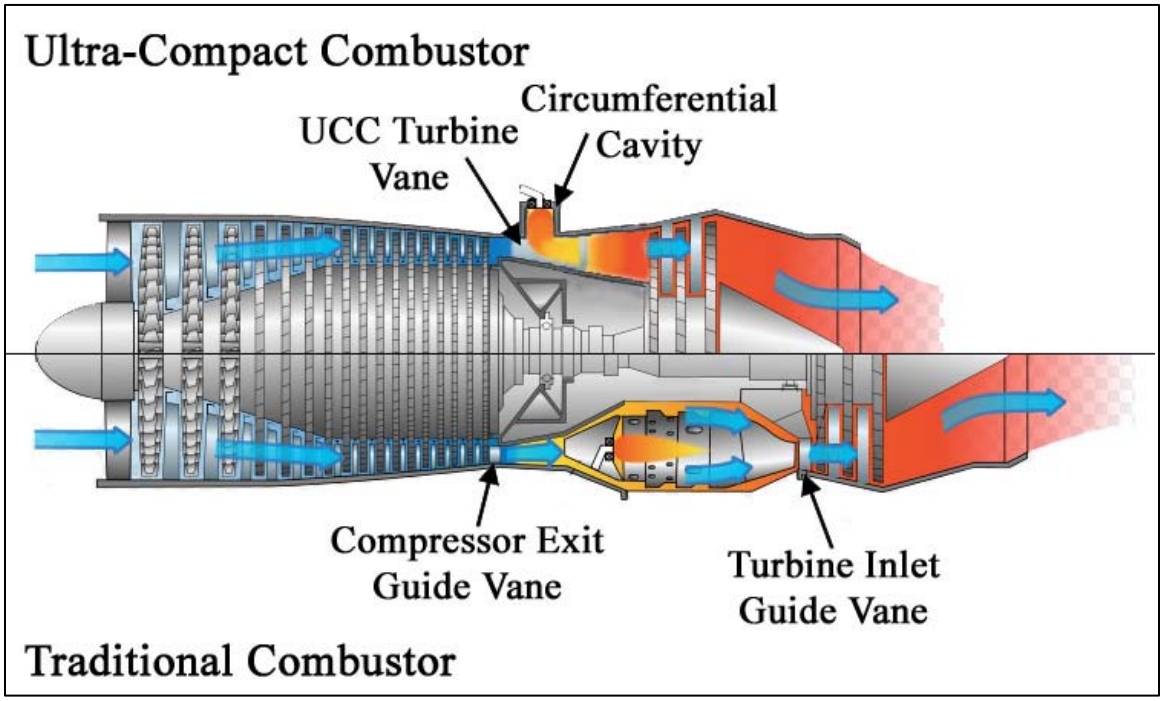

Figure 1.1: Reduced axial length in a modern turbine engine [3]

In addition to being a main combustor replacement, an interest has arisen in using the UCC as a second-stage combustor. A second-stage combustor, or inter-turbine burner (ITB), is located between the high-pressure and low-pressure turbines. With a modest

rise in temperature, high levels of low-pressure energy can be extracted in the low-pressure turbine [5]. The additional energy could be used to operate a large fan for an ultra-high bypass engine, or to drive a generator to create large amounts of electrical power for aircraft sensors, electronics, and weapons.

The UCC provides some unique challenges such as producing a uniform temperature distribution across the combined vane at off-design conditions. To be a replacement for a turbine engine main combustor, the UCC is designed to operate above stoichiometric fuel-to-air conditions in order to obtain an appropriate heat release in the combustor to produce the necessary work from the turbine. The above stoichiometric design condition has the potential to cause undesired heat releases when the UCC flow interacts with the axial (core) flow. The secondary heat releases could cause large variations in exit temperature profiles. In addition, recent research has shown that the ratio of velocities between the circumferential section and the axial section cause the combustion products to change ejection trajectories at the interface of the UCC and core section [6]. This causes drastic changes in the axial flow path creating varying locations of potential temperature increases. The challenge is to extract combustion products from the UCC section, mix them with the axial flow, and evenly distribute the mixture prior to exiting the axial section at all operating conditions.

1.2 Turbine Engine Emissions

Turbine engine emissions measurements grew in popularity in the early 1970's as part of the Climatic Impact Assessment Program (CIAP) [7]. While the purpose of the program was to establish the environmental impact of turbine engine emissions, it started a wave of new research areas. As the interest in engine exhaust emissions increased, the

need for standardized practices arose. In 1981, the methodology for calculating Emissions Index (EI) for combustion products was established [8]. This created a method for the emission products from different engines to be compared. Then in 1994, the modern standard for determining the efficiency of a combustor was established by the Society of Automotive Engineers [9]. With these practices instituted, a direct comparison between traditional combustors and the UCC emissions can be completed.

*1.3 **Objectives***

The main objective of this research was to show a desensitization of the ejection trajectory of the UCC flow into the axial flow at off-design scenarios. In order to accomplish the primary objective, two other tasks had to be completed. The first task was to determine the effects of changing the location of the main vane in the current UCC apparatus. By understanding the effects of moving the placement of the vane, correlations could be made between operating parameters and the effect they have on ejection trajectory. The second task was to implement a novel vane design to control the ejection trajectory of the UCC flow. The ejection trajectory for multiple operating parameters would be explored to ensure a uniform temperature distribution at the exit of the core section. In addition, the quantification of emission products also had to occur. Unburned hydrocarbons present in the exhaust are an indicator that secondary heat releases could occur in the downstream turbine. The tasks and objective laid out were all accomplished in an experimental investigation.

II. Background

2.1 Ultra-Compact Combustor

In 1997, Sirignano et al. [10] proposed a solution to achieving higher thrust-to-weight ratios while maintaining engine efficiency. Sirignano et al. showed that by introducing an ITB, the traditional turbine engine augmenter could be removed completely, thus becoming more fuel efficient without sacrificing any thrust. The UCC was one effort at satisfying the ITB proposal. The initial UCC design was completed by Anthenien et al. [11] in 2001. The Anthenien et al. design employed buoyancy effects through the use of centrifugal loading. Centrifugal loading, as documented by Lewis [4], facilitates combustion by increasing the reaction rates and ultimately the flame speed of a reaction. Lewis discovered that at centrifugal loading (g's) above 200 g's, a bubble of combusted gases would travel ahead of the flame front. At loadings less than 200 g's, the centrifugal loading is not high enough to propel the buoyant gases ahead of the flame front. Consequently, the flame speed is determined by the velocity of the flame front (turbulent flame speed). However, at loadings between 500 to 3500 g's, the flame speed increases with the square root of g because the centrifugal loading pulls the buoyant gases ahead of the flame front causing the flame speed to increase. Based on these observations, Lewis surmised that if the bubble velocity (S_B) is greater than the turbulent flame speed (S_T), then the flame will propagate at the bubble velocity as described in Equation 2.1. If the bubble velocity is less than the turbulent flame speed then the turbulent flame speed propagates the reaction.

In Equation 2.1, Lewis defined S_B to have units of ft/s and g to be the centrifugal loading normalized by the gravitational constant, g_c. Zelina et al. [5] modified Lewis'

definition to better suit their research on an UCC and defined normalized centrifugal loading with Equation 2.2. The radius of the circumferential section, r_{UCC}, is a designated value while tangential velocity, U_{tan}, is defined by Equation 2.3 [5]. In Equation 2.3, $\dot{m}_{UCC}$ is the mass flow through the circumferential section, ρ_{UCC} is the fluid density in the circumferential section, A_{exit} is the cross-sectional area of the section, and β is the swirl angle of the flow in the circumferential section.

$$S_B = 1.25\sqrt{g} \tag{2.1}$$

$$g = \frac{U_{tan}^2}{g_c r_{UCC}} \tag{2.2}$$

$$U_{tan} = \frac{\dot{m}_{UCC}}{\rho_{UCC} A_{exit} \tan\beta} \tag{2.3}$$

Figure 2.1 depicts the two cases Lewis proposed. The dark circles represent the bubbles of combusted gases that are moving at a velocity, S_B, in the time, Δt. The dashed line represents the flame front where on the left, the bubble is driving the reaction and on the right, the turbulent flame speed is driving the reaction.

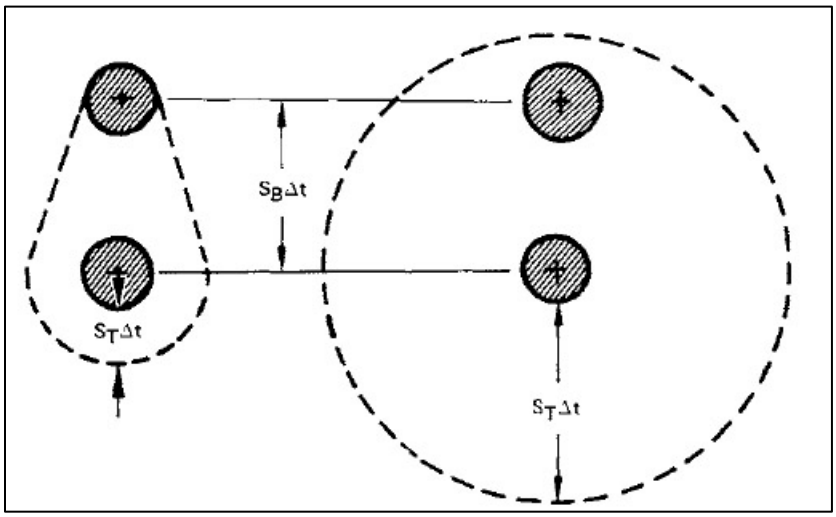

Figure 2.1: Bubble velocity dominated flame (left) versus turbulent velocity dominated flame (right) [4]

Lewis observed that above 3500 g's, the flame speed decreased significantly until blowout occurred between centrifugal loadings of 7000 – 8000 g's. Figure 2.2 shows the predicted bubble velocity and the observed flame speed of propane and air. This was corroborated by Zelina et al. [2] who conducted a series of lean blowout (LBO) tests on a small scale, full annulus UCC system. Zelina et al. found that the UCC had much wider LBO characteristics than conventional systems. More importantly, the flame remained stable up to 7000 to 8000 g's at an equivalence ratio of one. Figure 2.3 shows the flame stability region extrapolated from the experimental results as a function of g-loading and the maximum g-loading between 7000 – 8000 g's.

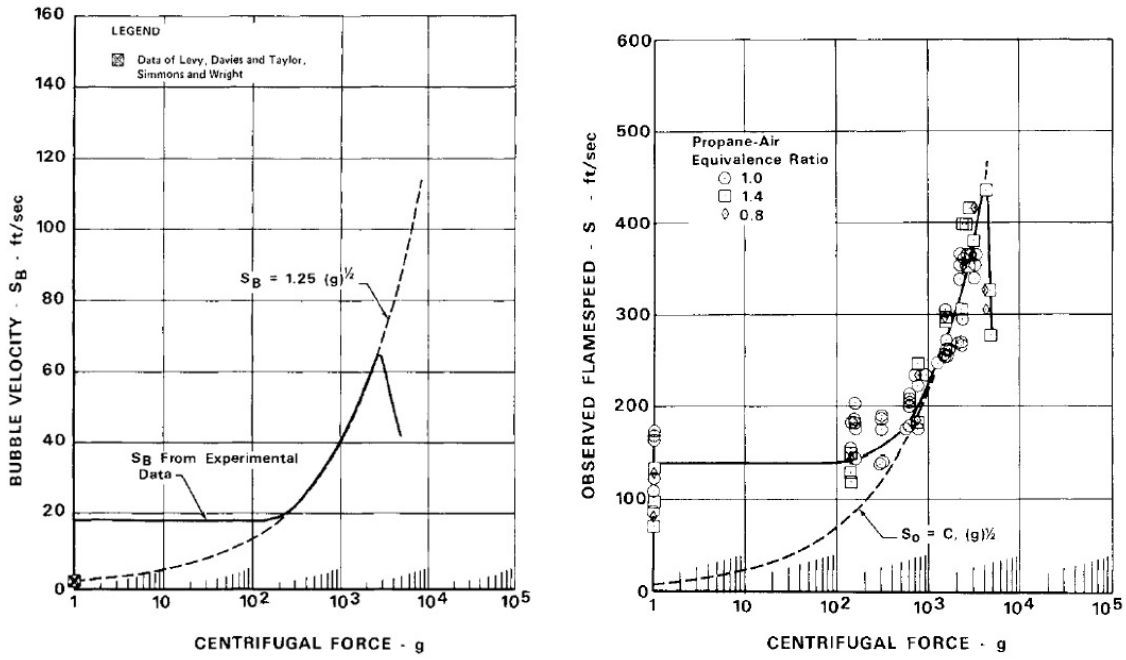

(a) (b)

Figure 2.2: Centrifugal loading effects on (a) predicted and experimental bubble velocity and (b) propane in air flame speed [4]

In addition to running the LBO experiments, Zelina et al. [2] attempted to computationally recreate Lewis' experimental results. Using the Unsteady Ignition and

Combustion with Reactions (UNICORN) code, flame propagation in a 0.05 m tube under two different g-loadings was modeled. The model used a hydrogen-air mixture at an equivalence ratio of 0.8 under the conditions of 10 g's, and 500 g's. The two loading conditions were chosen to illustrate when Lewis believed a bubble velocity was or was not a factor. Figure 2.4 depicts the flame front propagation at three points in time under the two loading conditions. Figure 2.4b easily shows that the increased g-loading nearly doubles the flame speed over the uniform flame front seen in Figure 2.4a.

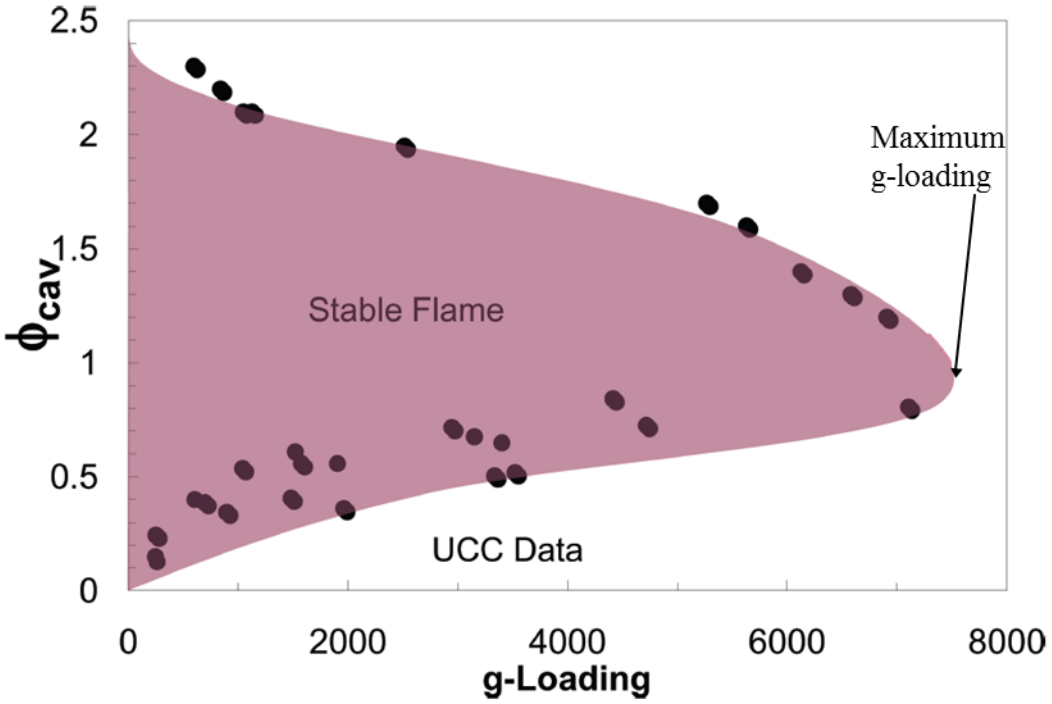

Figure 2.3: UCC LBO as a function of section g-loading using JP-8+100 as fuel [2]

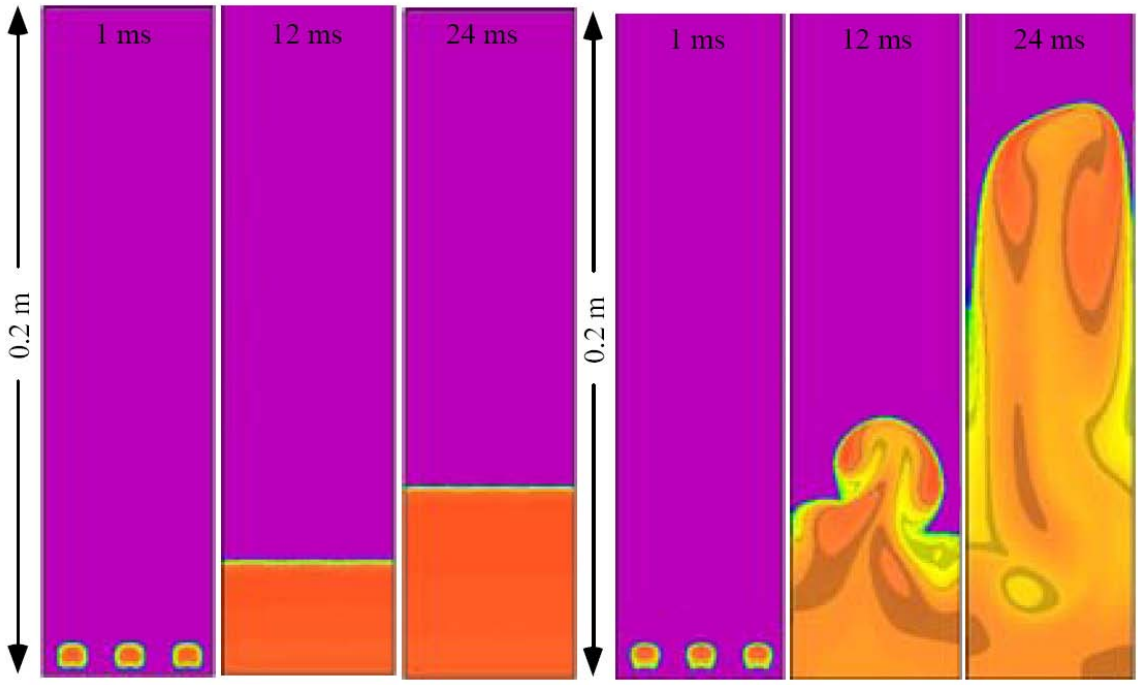

(a) (b)

Figure 2.4: UNICORN model of hydrogen in air flame front propagation under the loading condition (a) 10 g's and (b) 500 g's [2]

2.2 Mass Transport from Circumferential to Axial Section

A significant research area of the UCC was to address the migration of products from the circumferential section into the core section and then quantify the amount of mass entering the core section. Migrating the products from the UCC section to the core section is critical in establishing favorable temperature profiles for the turbine components. Without adequate migration, the potential exist for destructive temperature characteristics to enter the high pressure turbine. The following two sections describe an attempt to migrate the circumferential flow into the core section. The latter section addresses several of the factors affecting how the migration occurs.

2.2.1 Radial Vane Cavity

AFRL investigated using a notched airfoil in a trapped vortex combustor to help migrate products into the free stream. This notch, dubbed the radial vane cavity (RVC), was intended to create a low pressure zone within the airfoil to draw constituents into the notch. Once in the RVC, the core air cross-flow would transport the constituents through the core section. AFRL conducted a numerical investigation into the benefits of the RVC [12]. Mawid et al. found that the shape of the RVC could allow or inhibit the transport of combustion products from the UCC section to the core section. The shape also influenced the speed at which the products from the UCC section mixed with the core section. It was determined that the RVC became the critical component in the overall performance of the UCC. The final shape of the RVC was determined to be a parallelogram angled downstream as shown in Figure 2.5.

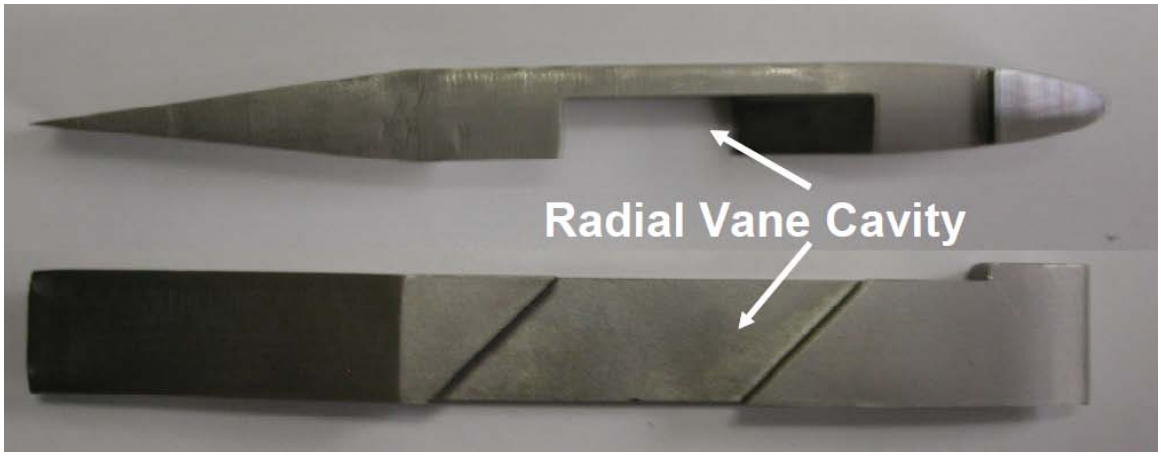

Figure 2.5: RVC as implemented by AFRL to increase circumferential flow migration from combustor OD to ID [2]

Zelina et al. [2] implemented the RVC into the AFRL UCC experimental research. The RVC was machined in accordance with Mawid et al. [12] and is seen in Figure 2.5. AFRL located the RVC such that it faced into the circumferential flow. Zelina et al. [2]

recorded bulk CO EI (Figure 2.6) to discern the amount of air entrained by the solid and RVC main vanes. Figure 2.6 shows that less CO was emitted at varying equivalence ratios when the RVC was used than by the solid vane. The lower CO levels is indicative of CO burnout occurring. The burnout of CO was interpreted as the RVC transporting the circumferential flow away from the circumferential cavity and into the freestream where the CO could finish reacting with O_2 from the core air. Zelina et al. did note that there appeared to be a trade-off between combustion efficiency and LBO [5]. While the radial vane increased the LBO characteristics, Zelina et al. saw a decrease in combustion efficiency at certain loading parameters. Anderson et al. confirmed the results, but noted that above $\Phi = 1.2$, the combustion efficiency exceeds 99 %, as seen in Figure 2.7 [13]. All three studies used JP-8 +100, the standard Air Force turbine engine fuel.

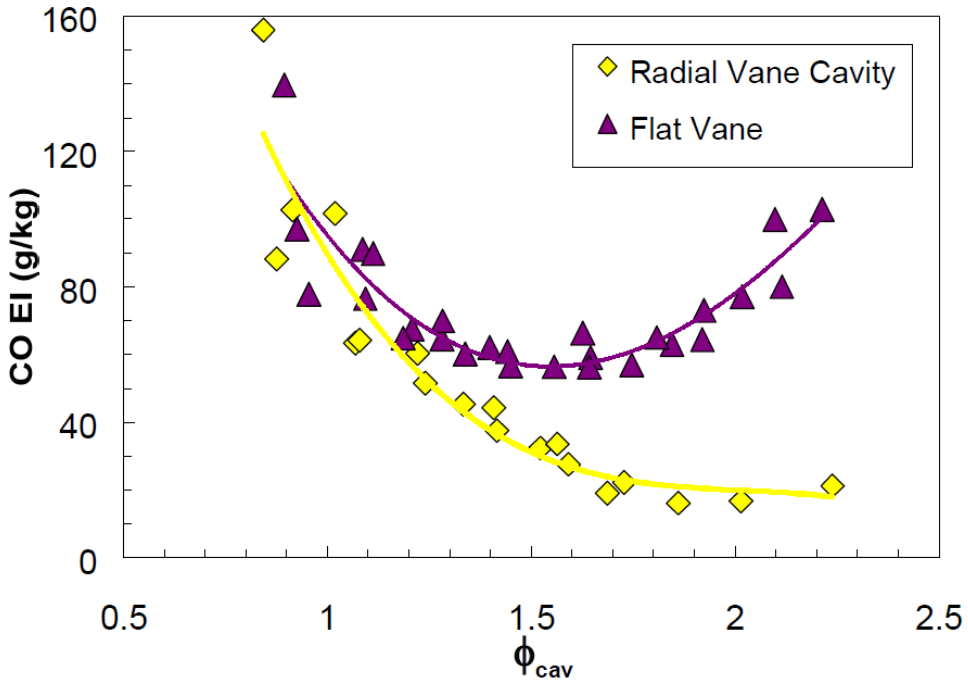

Figure 2.6: Decrease in CO EI in RVC as opposed to the flat vane for multiple equivalence ratios [2]

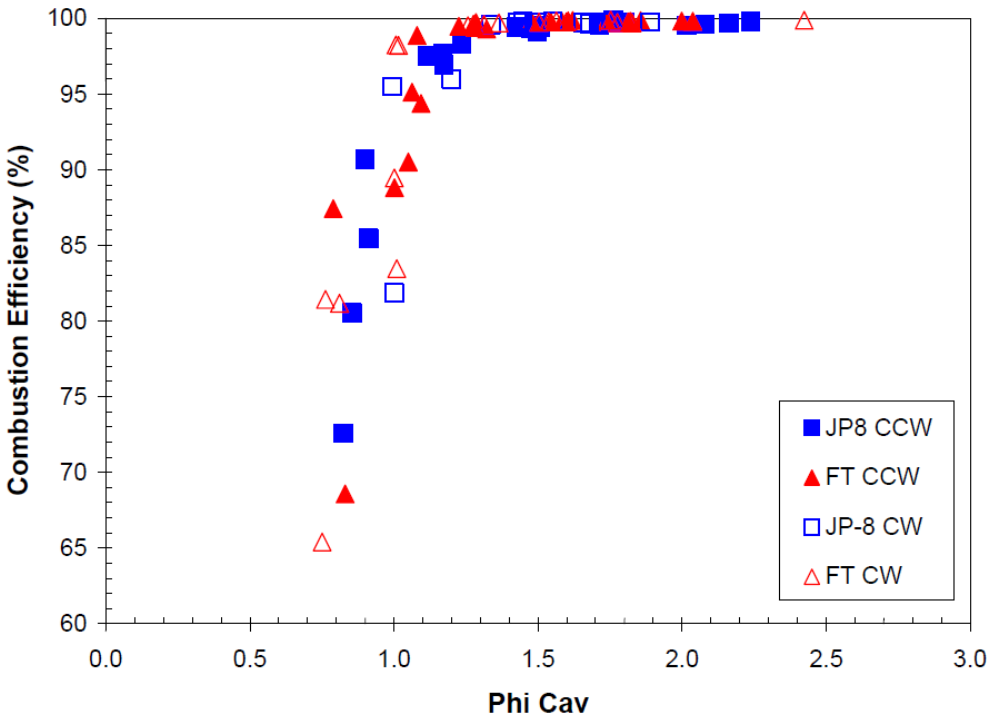

Figure 2.7: A near constant combustion efficiency of the UCC at an equivalence ratio above 1.2 [13]

The RVC was adopted in the experimental test configuration used by Drenth [14] and Thomas [15]. For these experiments, the RVC was located so it faced away from the circumferential flow as denoted in Figure 2.8. Drenth explored the behavior of the AFIT UCC section for equivalence ratios between 0.5 and 1.5. Using a Testo 350 gas analyzer, Drenth recorded combustor efficiencies around 99 %. These results correlated well with the results of Zelina et al. [5] indicating that the RVC increased combustion efficiency in the process of migrating hot products to the ID of the core section. Thomas observed very high vorticity levels within the RVC and concluded that the angle of the RVC enhanced mixing between the circumferential cavity and the core flow. Radtke [16] explored the effects of operating the RVC facing into and away from the circumferential flow on the AFRL full annulus. As stated previously, Figure 2.8 shows the RVC when it

is facing away from the circumferential flow; the RVC would be facing into the circumferential flow if it was located on the opposite side of the vane. Radtke noticed minimal differences in bulk emission performance, but did note that on average the combustion efficiency was slightly higher when the RVC was facing into the circumferential flow direction. Radtke also observed that with the RVC facing into the circumferential flow, the combustor efficiencies remained higher over a wider range of operating parameters like Zelina et al. [5] observed.

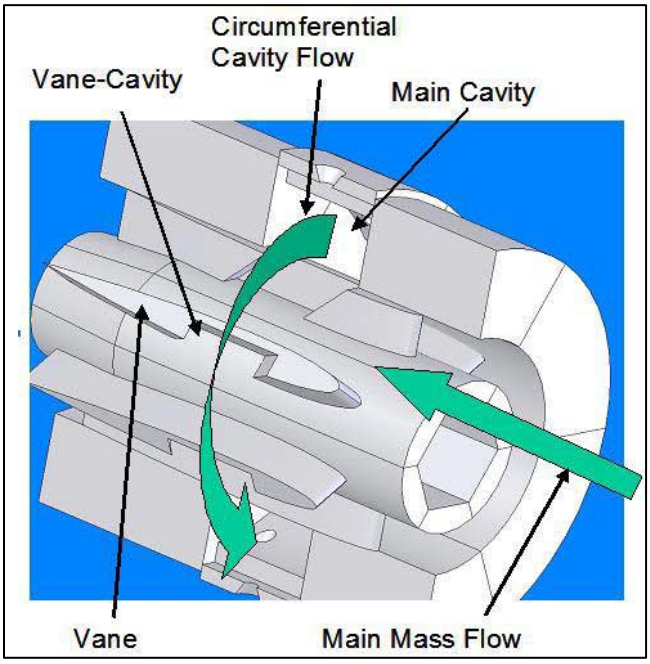

Figure 2.8: The RVC as employed at AFIT with radial cavity facing away from the circumferential flow [15]

2.2.2 Flame Trajectory

Mawid et al. [12] identified a significant challenge with the RVC. It was observed that the temperature profiles created by the RVC were unorthodox, as shown in Figure 2.9. A typical turbine vane temperature profile would contain only one temperature peak; however, the profiles in Figure 2.9 contain multiple temperature peaks

causing them to be unorthodox for turbine designers. Additional research would have to occur to create a temperature profile more conducive to the turbine components. The unusual temperature profiles correlate directly to the location of the flame in the core section. Therefore, if the location of the flame could be controlled, a method to influence the temperature profile could be investigated. In order to determine the location of the flame, it was imperative to determine operating conditions that affect not only the way the RVC operates but also how the flow migrates from the OD to ID of the core section.

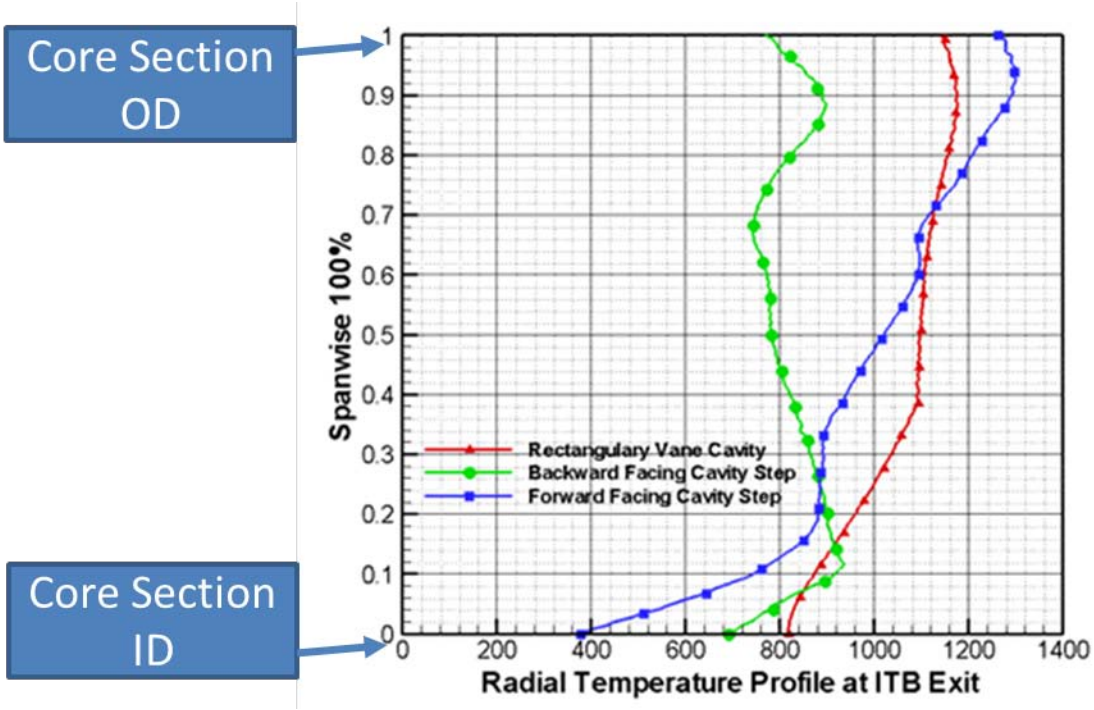

Figure 2.9: CFD computed radial temperature (K) at UCC exit plane showing potential for multiple peak temperatures [12]

LeBay et al. [6] began to experimentally determine the UCC operating parameters affecting the RVC's performance. Key to the combustor's success was migrating enough hot products away from the OD so it would be easy to cool; however, it was also important not to transport too much hot products such that additional cooling was needed

on the ID. Therefore, it was of particular interest which parameters caused the products to travel completely from the OD to the ID of the core section. LeBay et al. found that the centrifugal loading minimally affected the way the flame migrated into the core section. Instead, the mass flow ratio (MFR) between the UCC and core section heavily dictated the angle at which the flame impinged upon the core section. The MFR was defined as the ratio of the mass flow in the circumferential cavity to the mass flow in the core cavity as seen in Equation 2.4. LeBay et al. found that at very low MFRs (i.e. 0.05) the flame entered the core section at a very shallow angle. As MFR increased, so did the angle at which the flame impinged on the core section as seen in Figure 2.10

$$MFR = \frac{\dot{m}_{cavity}}{\dot{m}_{core}} \tag{2.4}$$

LeBay et al. also found that MFR affected the magnitude of flame impingement into the core cavity. As shown in Figure 2.10, at low MFRs, the flame travels about 1/3 of the RVC span; however, at high MFRs, not only does the flame traverse the RVC span, but it also collides with the core section ID. From these results, LeBay concluded that the best operating conditions for the AFIT UCC sector model was at an MFR = 0.2 in which the flame reaches the ID of the core section, but does not reach it as violently as in the MFR = 0.3 case where substantial ID cooling would have to be considered in order to counteract the migration of the UCC flame. Ideally, the flow would exit the UCC section and cross the vane span without impinging on the core section ID. This would reduce the pressure losses associated with hitting the ID wall as well as alleviate some of the cooling issues associated with having hot products localized on the ID. Therefore, a mechanism that could consistently coerce hot products out of the UCC section, turn the

flow axial, and evenly distribute the products across the airfoil span would be quintessence.

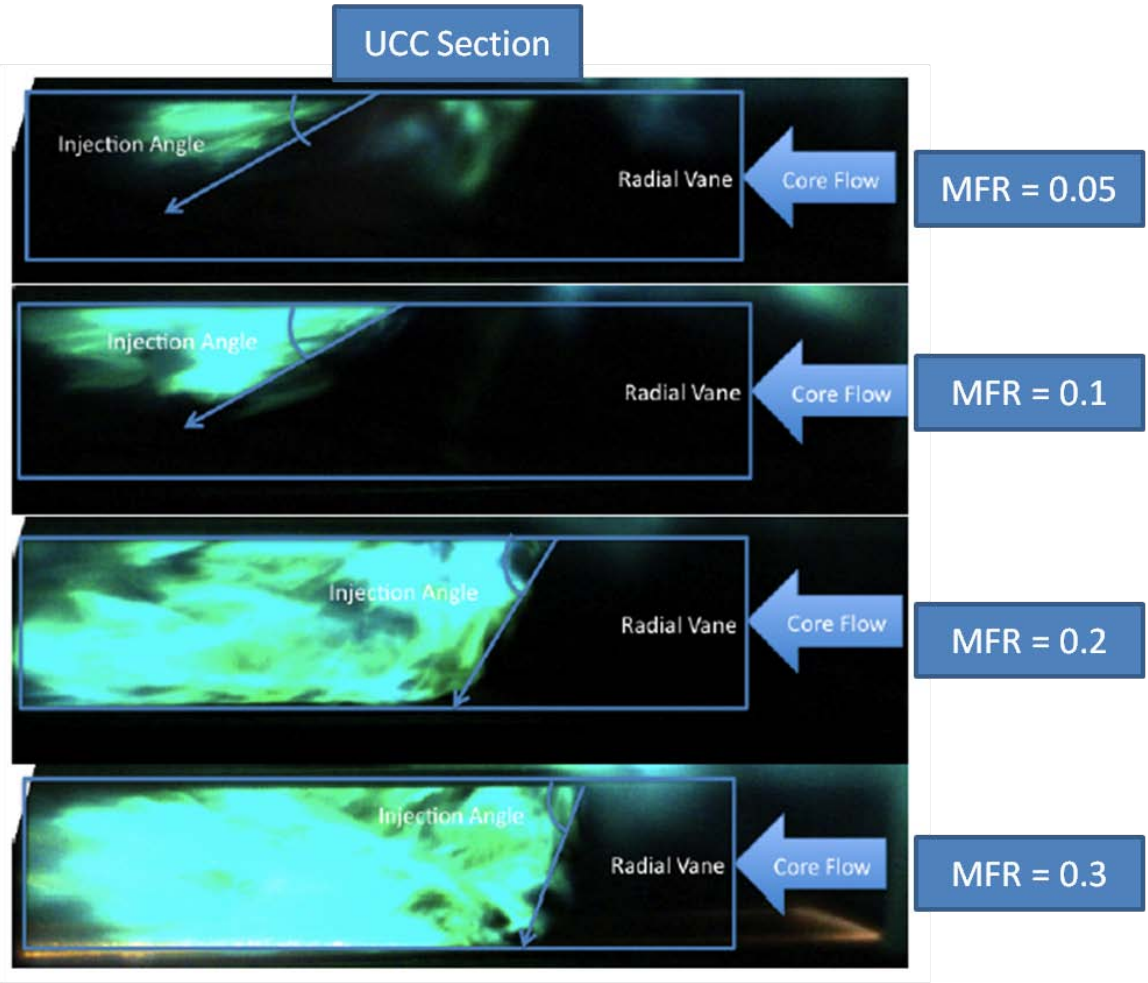

Figure 2.10: Changes in flame migration into the core section based on MFR [6]

In order to quantify the amount of mass entering the core section, LeBay [17] applied a simple mass conservation analysis to estimate the amount of mass that was transferring between the circumferential and axial cavities. LeBay controlled the amount of air and fuel mass entering into the circumferential cavity; therefore, the upstream conditions were known quantities. LeBay then placed a pressure transducer and thermocouple at the ignition site of the circumferential cavity to be able to estimate the

density of the fluid. LeBay then took particle image velocimetry (PIV) data at the exit plane of the circumferential cavity. Knowing the velocity and area at the exit plane of the circumferential cavity, LeBay was able to estimate the amount of mass exiting the circumferential cavity to atmosphere. Knowing the amount of mass entering the UCC section and experimentally estimating the amount of mass exiting the UCC section to atmosphere allowed LeBay to estimate the quantity of mass entering the axial cavity.

2.3 Emission Index and Combustor Efficiency

One method of quantifying emissions is to collect the concentration either in parts per million (ppm) or percent of sample. The Society of Automotive Engineers (SAE) published Aerospace Recommended Practice (ARP) 1533A in 1994 which established a standard method of taking concentration data and converting it to EI. Emissions Index allows developers and regulators to have a standardized number that takes into account both concentrations of constituents and the constituent's effect on the environment [9]. Emission Index, as defined in Equation 2.5, is the ratio of as constituent's mass per unit mass of fuel. When considering the emissions data is recorded as concentrations Equation 2.5 is modified to Equation 2.6 for ease of calculation.

$$EI_Z = \left(\frac{m_Z}{m_{fuel}}\right)(1000) \tag{2.5}$$

$$EI_Z = \left(\frac{[Z]}{[CO]+[CO_2]+[UHC]}\right)\left(\frac{10^3 MW_Z}{MW_c+\frac{y}{x}MW_H}\right)\left(1+\frac{0.00034X}{m}\right) \tag{2.6}$$

Once the EI process had been established, the efficiency of that process can be determined. SAE ARP 1533A [9] uses an enthalpy based definition of efficiency. The definition compares the amount of energy released by the process to the amount of energy which would be realized if all the fuel were oxidized into carbon dioxide and

water vapor. Combustor efficiency, represented as a percentage, can be found in Equation 2.7. Carbon monoxide and UHC are inefficiency identifies in the combustion process; therefore they are the only constituents that appear in Equation 2.7. The heat of combustion of the process fuel is represented by H_C in Equation 2.7.

$$\eta_b = \left[1.00 - 4.346\frac{EI_{CO}}{H_c} - \frac{EI_{UHC}}{1000}\right] * 100 \tag{2.7}$$

2.4 Expression of Air-Fuel and Equivalence Ratios

Pre-mixed combustion is typically classified into one of three categories: lean ($\Phi < 1$), rich ($\Phi > 1$), or stoichiometric ($\Phi = 1$), where Φ is defined as the equivalence ratio. A stoichiometric mixture occurs when the quantity of available oxidizer is the precise amount needed to completely react a quantity of fuel [18]. Turns [18] offers Equation 2.8 to represent a stoichiometric relationship for hydrocarbon fuels mixed with air. Equation 2.8 relays that *a* moles of air are needed to exactly combust one mole of C_xH_y fuel. To find the stoichiometric air-fuel ratio (A / F), Equation 2.9 relates the mass of air and fuel (m_X) to their respective molecular weights (MW_X). Equation 2.9 can then be written in terms of the mass flow rates of air and fuel as seen in Equation 2.10. Equivalence ratio is defined as the stoichiometric air-fuel mixture normalized by the air-fuel ratio available, as found in Equation 2.11.

$$C_xH_y + a(O_2 + 3.76N_2) \rightarrow xCO_2 + (y/2)H_2O + 3.76aN_2 \tag{2.8}$$

$$(A/F)_{stoic} = \left(\frac{m_{air}}{m_{fuel}}\right)_{stoic} = \frac{4.76a}{1}\frac{MW_{air}}{MW_{fuel}} \tag{2.9}$$

$$(A/F)_{stoic} = \left(\frac{\dot{m}_{air}}{\dot{m}_{fuel}}\right)_{stoic} \tag{2.10}$$

$$\Phi = \frac{\left(\frac{\dot{m}_{air}}{\dot{m}_{fuel}}\right)_{stoic}}{\left(\frac{\dot{m}_{air}}{\dot{m}_{fuel}}\right)} \tag{2.11}$$

The research in this document, as well as several previous documents, used an air-propane mixture [3, 6, 14, 15]. The stoichiometric equation and air-fuel ratio for the air-propane mixture is Equation 2.12 and Equation 2.13, respectively [18]. Equivalence ratio will be used extensively in this document to describe mixtures as rich, lean, or stoichiometric in nature.

$$C_3H_8 + 5(O_2 + 3.76N_2) \rightarrow 3CO_2 + 4H_2O + 18.8N_2 \tag{2.12}$$

$$\left(\frac{\dot{m}_{air}}{\dot{m}_{fuel}}\right)_{stoic} = (A/F)_{stoic} = \frac{4.76(5)}{1}\frac{28.85\frac{kg}{kmol}}{44.096\frac{kg}{kmol}} = 15.571 \tag{2.13}$$

2.5 Jets in a cross-flow

The fuel and air injectors used in the AFIT UCC section act as jets in a cross-flow. Therefore, it is important to understand the behavior of jets in a cross-flow. This topic has been studied extensively in film cooling applications. The first property that affects the way a jet reacts in a cross-flow is the blowing ratio, M. Equation 2.14 shows the relationship between the jet properties, denoted with a 'j', and the cross-flow properties, denoted by ∞, to find M. In the documented research, density and velocity were unknown quantities; however, by using conservation of mass, a relationship between the mass flow rate and area of the jet to the cross-flow can be determined. This relationship is shown in Equation 2.15.

$$M = \frac{\rho_j U_j}{\rho_\infty U_\infty} \tag{2.14}$$

$$M = \frac{\dot{m}_J A_\infty}{A_j \dot{m}_\infty} \tag{2.15}$$

Many sources document the effect of M on the film cooling effectiveness. For the purposes of this work, film cooling effectiveness is synonymous with the jet plume trajectory. Baldouf et al. [19] documented the effectiveness of angled jets at varying blowing ratios as seen in Figure 2.11. For Figure 2.11, the darker areas are indicating a higher cooling effectiveness. In Figure 2.11, the lack of dark gray areas at high M is indicating a lack of film cooling effectiveness. The decreased effectiveness is indicative of the jet separating from the surface.

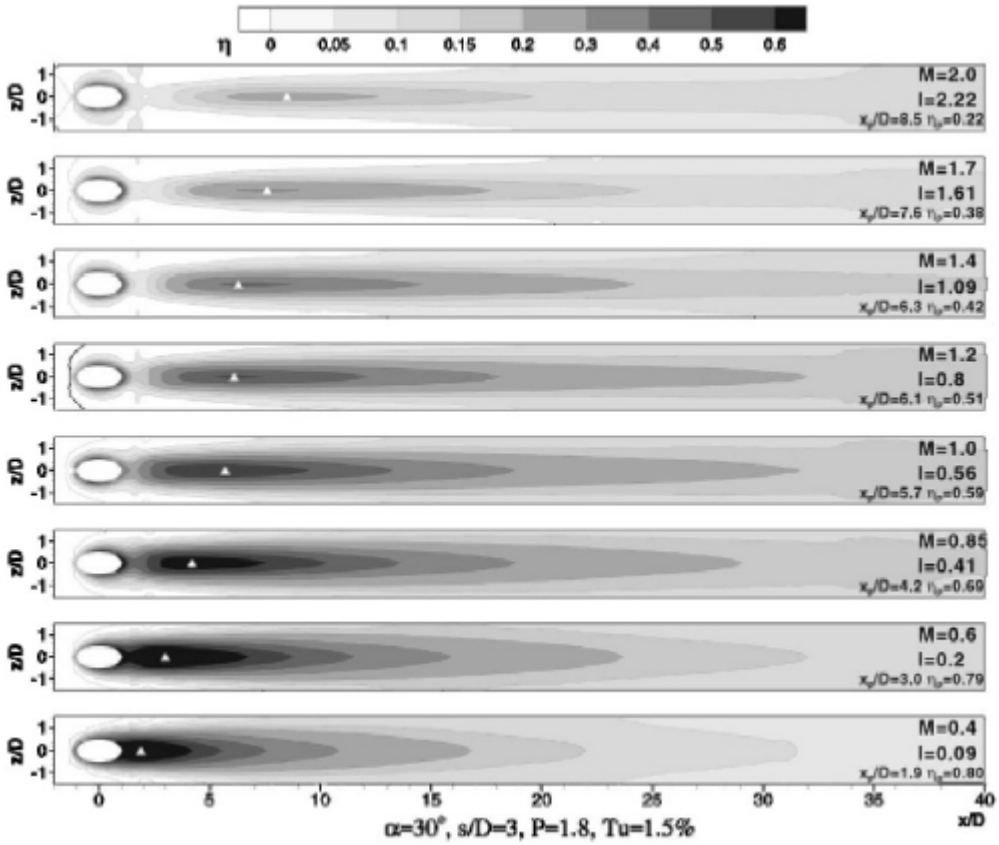

Figure 2.11: Distribution of film cooling effectiveness at varying blowing ratios for angled holes [19]

Film cooling research has also shown that the jet's angle to the cross-flow affects the plume trajectory. Additional experiments completed by Baldouf et al. [19] were

accomplished with holes normal to the cross-flow. Figure 2.12 shows the film cooling effectiveness between the angled holes (top) and the normal holes (bottom). Based on the intensity of the shaded regions, Baldouf et al. show that at high blowing ratio the normal jet plume is more effective than the angled holes with downstream distance from the jet. It is also noted, that at M = 2.0, neither plume is effective near the hole. The lack of effectiveness indicates that both angled and normal holes, at high blowing ratios, will separate from the surface. The results also imply that at high M the angled jet plume dissipates in less downstream distance than the normal jet based on the relative distance of the peak effectiveness location to the jet.

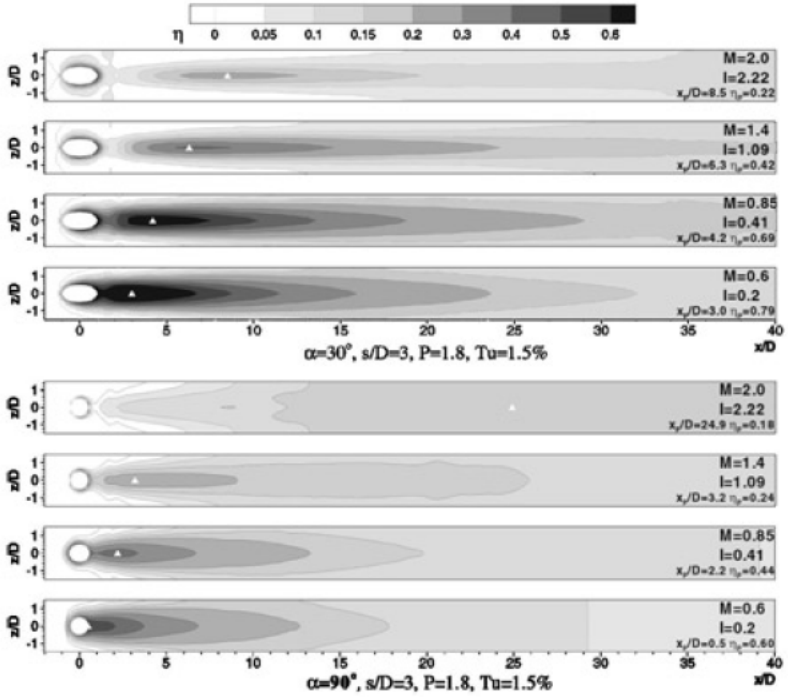

Figure 2.12: Changes in jet plume trajectories based on injection angle [19]

With the results of Baldouf et al. clearly indicating a separation occurring at high M, the experimental results of Thole et al. [20] help describe the degree of separation that occurs at high M. For the results reported by Thole et al., the temperature contours are an

indicator of where the jet plume was located. Thole et al. showed that for nonreacting film cooling flow emanating from holes angled at 35 degrees and M = 2, temperature contours were affected up to two diameters in perpendicular distance from the hole opening before the cross flow overcame the momentum of the jet. The maximum penetration distance of the jet occurred at roughly eight diameters downstream. Corroborating the results of Thole et al., Polanka et al. [21] experimentally showed that for reacting, angled jets at M = 2 in a cross-flow, the plumes traveled roughly four diameters away from the cooling hole with a downstream distance of seven diameters as seen in Figure 2.13.

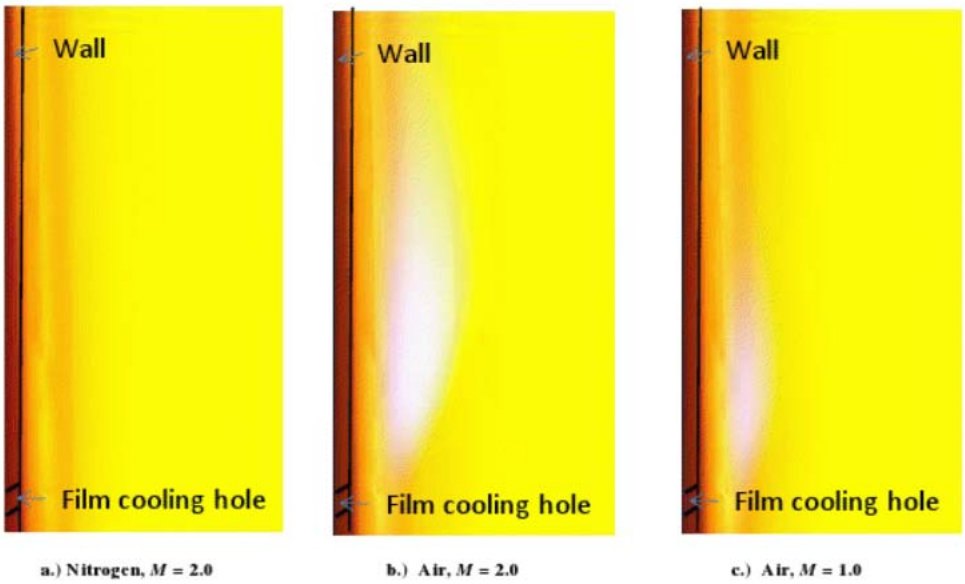

Figure 2.13: Thermal response from film cooling jets in a reacting cross-flow [21]

Polanka et al. [21] also numerically showed that for normal holes at M = 1, the jet plume travels a maximum distance of roughly three diameters away from the wall with six diameters of downstream distance as seen in Figure 2.14. Comparing the results from Figure 2.13 and 2.14, it appears that normal holes achieve their maximum perpendicular

distance away from the orifice in less downstream distance, but the angled jets achieve a greater perpendicular distance with downstream distance.

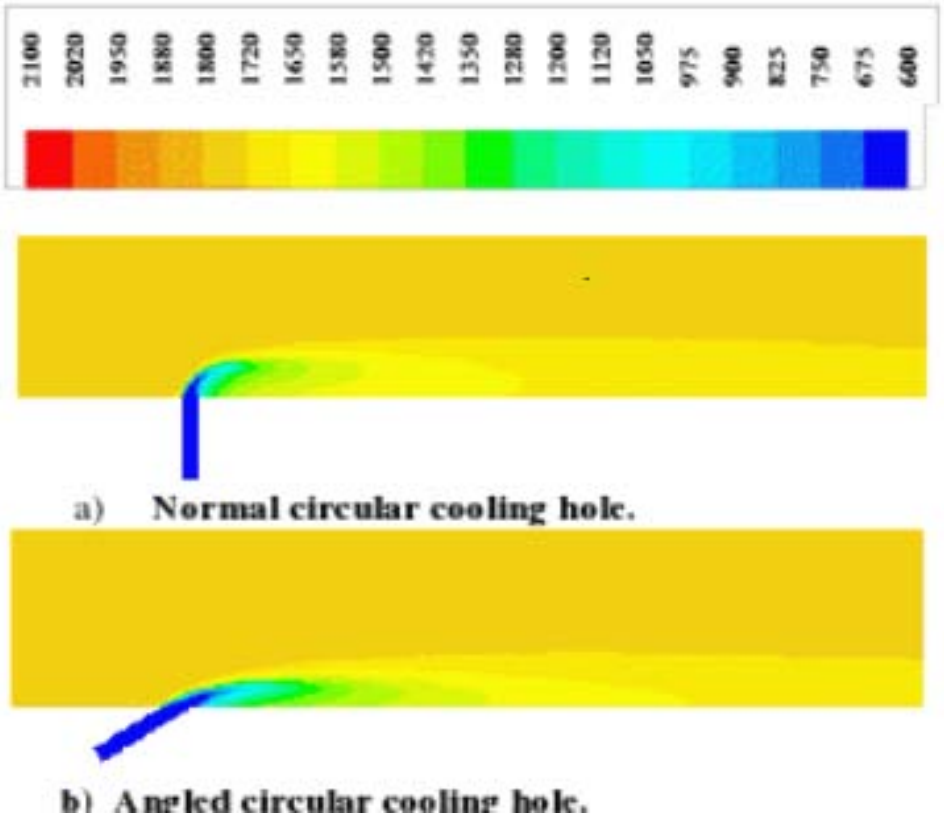

Figure 2.14: Numerical results of film cooling jets in a reacting cross-flow [21]

2.6 Chemiluminescence

During certain chemical reactions, the emission of light is observed. The emission of light with very little heat produced is called chemiluminescence. In recent years, the imaging of chemiluminescent events has become a popular method in identifying reaction zones [22, 23, 24]. Stojkovic et al. [22] took advantage of high speed imagery to locate the OH radical formation in a gasoline internal combustion engine. Stojkovic et al. could then confirm the reaction zone regions from the chemiluminescence of the OH radical. Cross et al. [23] captured chemiluminescence of CH, C_2, and CO_2 to explore oscillations due to vortex shedding in a natural gas and air flame. The radicals CH and

C_2 only emit in the blue and green spectrums; therefore, Cross et al. [24] used only the blue and green channels of a high speed camera to capture the chemiluminescence of CH and C_2 in a Jet-A and air flame.

By taking advantage of known chemiluminescent events, previous research has shown that the location of the flame in a combustion environment can be inferred. For most combustion of hydrocarbon fuels, the CH radical is created. When the CH radical is created, it illuminates at a wavelength of 430 nm [25]. The isolation of the blue channel in a digital image essentially allows only the creation of CH to be tracked. LeBay [17] used a time average of the blue channel intensity to find the approximate location of the CH radical production in the core section of the AFIT UCC section. This allowed LeBay to estimate the path the flame took as it exited the UCC section and qualitatively show the difference in angles based upon different operating conditions. LeBay also used the results to identify areas of flame unsteadiness.

2.6 Limitations of Previous Work

Previous research done using the AFIT UCC section was accomplished with the RVC facing away from the flow in the circumferential cavity. This was done to allow optical access for non-intrusive measurement techniques. Radtke [16] showed that for a full annulus, minimal effects to combustor efficiency were observed when the RVC was oriented away from the circumferential flow. Research with the AFIT UCC section has not validated that the sectional test rig acts in the same manner as the full annulus. LeBay [17] attempted to estimate the amount of mass transferred from the circumferential cavity into the axial cavity; however, this method has not been validated.

In order to validate that the sectional test rig is replicating the performance of the full annulus, a better method of quantifying mass transfer needs to be established.

Drenth [14], Thomas [15], and LeBay explored the axial cavity characteristics as a function of UCC operating parameters. Significant differences in the axial cavity characteristics were documented to be dependent on the UCC operating parameters: most notably MFR. In addition, Mawid et al. concluded that the core section exit plane exhibited unorthodox temperature profiles in the current state. The variations in the exit plane characteristics of temperature profile, flame shape, and emissions spectra make integrating the UCC into a turbine engine exceedingly difficult. As a result, there is a need to desensitize the axial cavity exit plane characteristics at off-design conditions. The exit plane characteristic should have limited variation from the on-design conditions. Currently, there is no known research that is actively pursuing a method to render the UCC exhaust characteristics independent of operating parameters.

III. Experimental Set-up

While most combustors are relatively simple, the UCC is not a trivial piece of hardware. The following chapter will guide the reader through an overview of the AFRL test rig, the derivation of the AFIT test section from the AFRL rig, and the capabilities of the facilities that house the AFIT test section. A detailed description of the experimental setup and methodologies used for the research work are also included.

3.1 AFIT UCC Test Section

While researching the potential of a UCC, AFRL constructed a full annulus UCC test rig [2, 5]. The full annulus, shown in Figure 3.1, has a mean radius of 0.055 m with six fuel injection locations equally spaced around the OD of the UCC cavity [2]. Air is injected into the cavity through pairs of holes. There are two pairs of holes between every fuel location for a total of twenty-four air injection holes. The holes are angled to 45 degrees to induce the bulk circumferential movement in the cavity. As depicted in Figure 3.1a, a centerbody was used to simulate the actual engine geometry and to house the guide vanes (shown in Figure 3.1b) which direct the upstream flow past the circumferential cavity.

AFIT developed their sectional model to replicate one vane passage (the area between two of the vanes on the centerbody) of the AFRL full annulus. This vane passage is depicted in Figure 3.2. Henceforth, the vane passage will be referred to as the 'core section' (due to the engine's core mass flow passing through this passage). The core section was fabricated from 316 stainless steel. It has a pitch (the distance between the bottom of the core section and the top) of 0.030 m and a span (the distance between the OD and ID of the core section) of 0.028 m. This gave the core section an inlet and

exit area of 0.00084 m^2. The core section housed the guide vane, shown in Figure 3.2, which could be replaced in order to evaluate a variety of airfoil shapes and designs. Air was supplied to the core section upstream of the vane.

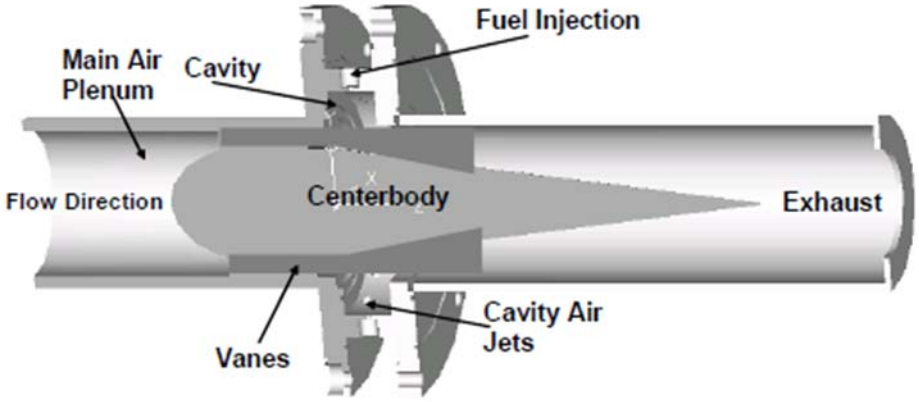

(a)

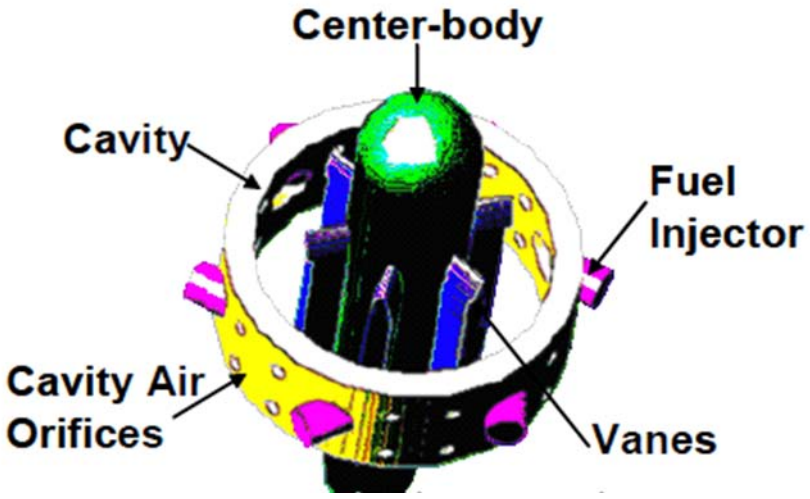

(b)

Figure 3.1: Configuration of the AFRL UCC test rig in (a) axial orientation and (b) cavity, vane, fuel, and air locations [2]

Moenter, who designed the AFIT test section, included multiple optical access points in order to capitalize on the laser based measurement techniques available at AFIT (these techniques will be discussed later) [26]. These optical access points allow the

AFIT section to investigate the flow field in the UCC and core sections above that available in the AFRL full annulus. The core section had optical access in the pitch-span plane upstream of the vane (Figure 3.2), in the pitch-chord plane at the vane (Figure 3.3), and the axial-span plane above the vane (Figure 3.2). The optical access was provided by UV-grade fused silica windows. The windows, manufactured by Behm Quartz, were surrounded by a ceramic insulator called Fiberfrax. This was used to not only seal gaps between the quartz and the stainless steel, but it also alleviated the thermal stresses due to the differing thermal expansions.

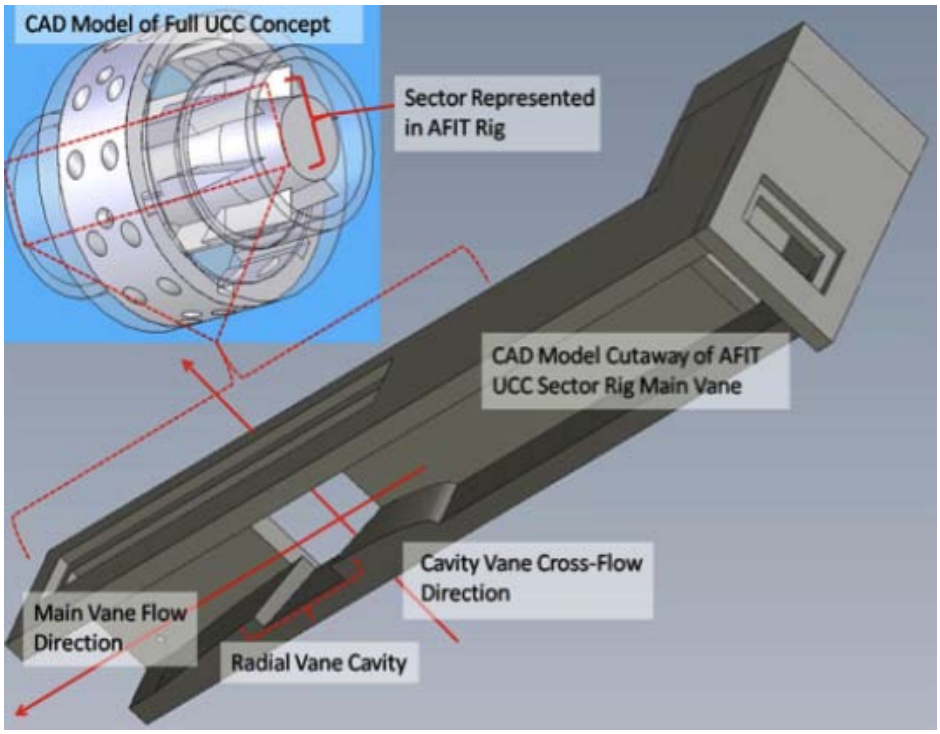

Figure 3.2: AFIT core section as compared to the AFRL full annulus

The circumferential section was developed to replicate the swirling flow that would be observed in the full annulus circumferential cavity. Henceforth, the circumferential section will be referred to as the 'UCC section' as it is the ultra-compact component of the combustor. It was designed to simulate two fuel injection locations: one at the vane

passage and one upstream of the passage. Therefore, it included everything that one-third of the AFRL full annulus housed.

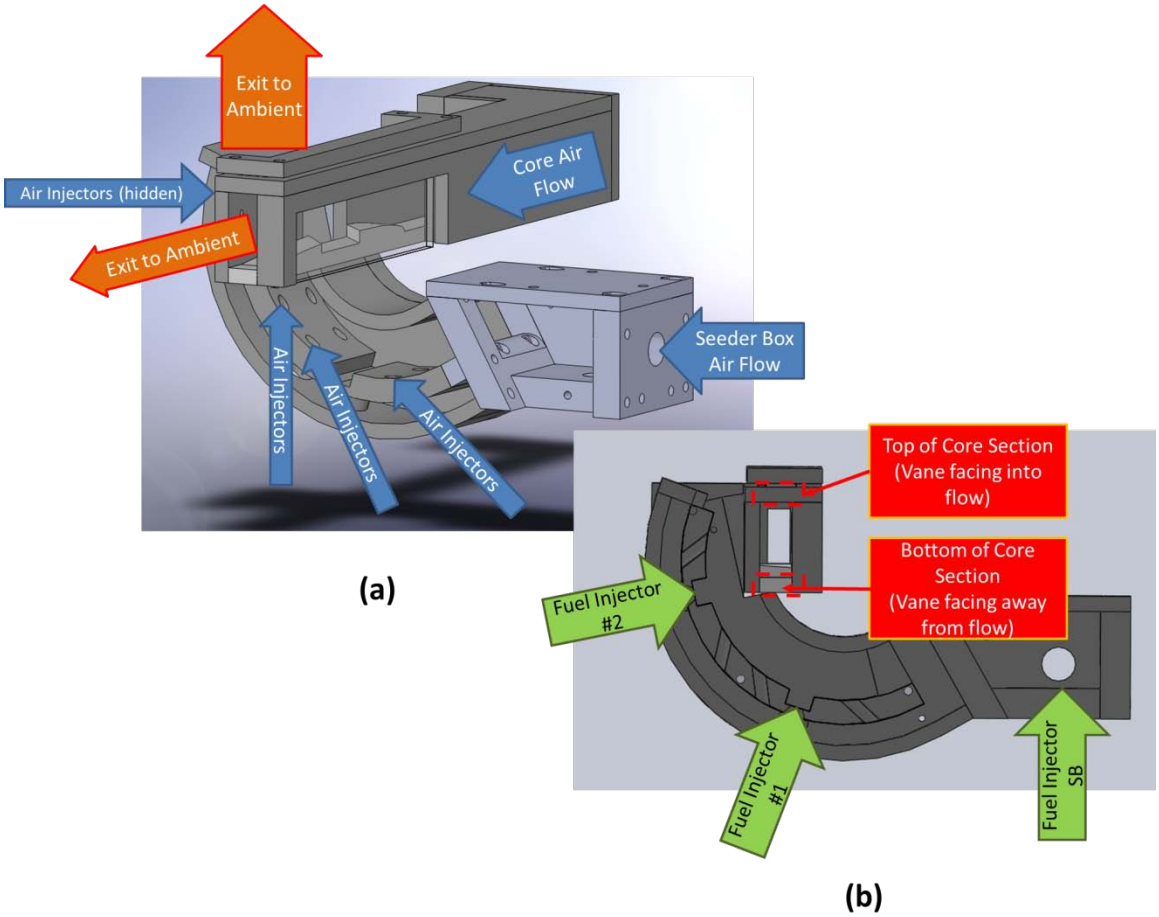

Figure 3.3: AFIT's UCC section affixed to the core flow section (a) depicting air inlet locations and (b) fuel inlet locations

The UCC section was also constructed out of 316 stainless steel and mounted to the core section at roughly mid-chord of the main vane, see Figure 3.3. The UCC section has a radius of curvature of 0.055 m, a width of 0.038 m, and a depth of 0.0135 m. This gives the UCC an exit area of 0.000513 m^2. The UCC section has a circumferential length of roughly 0.14 m. Four pairs of 0.00533 m diameter air injection holes were equally spaced around the circumference of the section. One of the several differences in the UCC section over the full annulus design was that the air injection holes were angle at

37 degrees downstream instead of 45 degrees. These holes provided the bulk air swirl to the UCC section. The second difference is the fuel injection occurred radially instead of angled as seen in the AFRL full annulus. The two fuel injectors located in the UCC section were equally spaced around the circumference of the section as indicated in Figure 3.3. The injectors were recessed in a rectangular cavity and emitted fuel from a 0.0032 m diameter hole. One mass flow controller was used to control the fuel to the two injectors in the UCC section.

The AFIT test section has three distinct traits that make it desirable for executing experimentation. First, the AFIT test section has 3 different optical access points allowing for interrogation into the flow field above the capabilities of a full annulus. Second, the AFIT test section has dedicated facilities to operate the test section which lend it to having greater availability than the full annulus. Third, the AFIT test section has modular geometry allowing for a wide range of components to be tested in the section more readily than in the full annulus [17]. With these reasons, the AFIT test section was more desirable for testing than the AFRL full annulus.

3.2 Combustion Optimization and Analysis Laser (COAL) Laboratory

The COAL Laboratory was designed and built by Anderson [26] for the purpose of testing small scale combustors such as the sectional UCC. Anderson consolidated the control and operating procedures for the experimental techniques and their data acquisition systems in the COAL Laboratory. Koether [27], using the OH-Planar Laser Induced Fluorescence (PLIF) experimental technique on a laminar premixed flame, validated the abilities of the laboratory.

Facility air is supplied to the laboratory by two, 50 hp Ingersoll Rand air compressors. For the UCC research, the air compressors are capable of providing 7 kg/min of air to the core section on the main supply line and 2 kg/min of air to the UCC section on the secondary supply line. Each supply line is controlled by a Badger Meter research control valve as seen in Figure 3.4. The control valves are needle valves that are pneumatically actuated. To act as the flow control feedback loop, each line contains a Fox Thermal Instruments FT2 flow meter. This meter quantifies the mass flow rate of the line, with an accuracy of +/-1 % of the measured value, and returns the signal to the laboratory's control software. The control software then adjusts the pneumatic signal being sent to the control valves in order to accurately supply the needed mass flow rate.

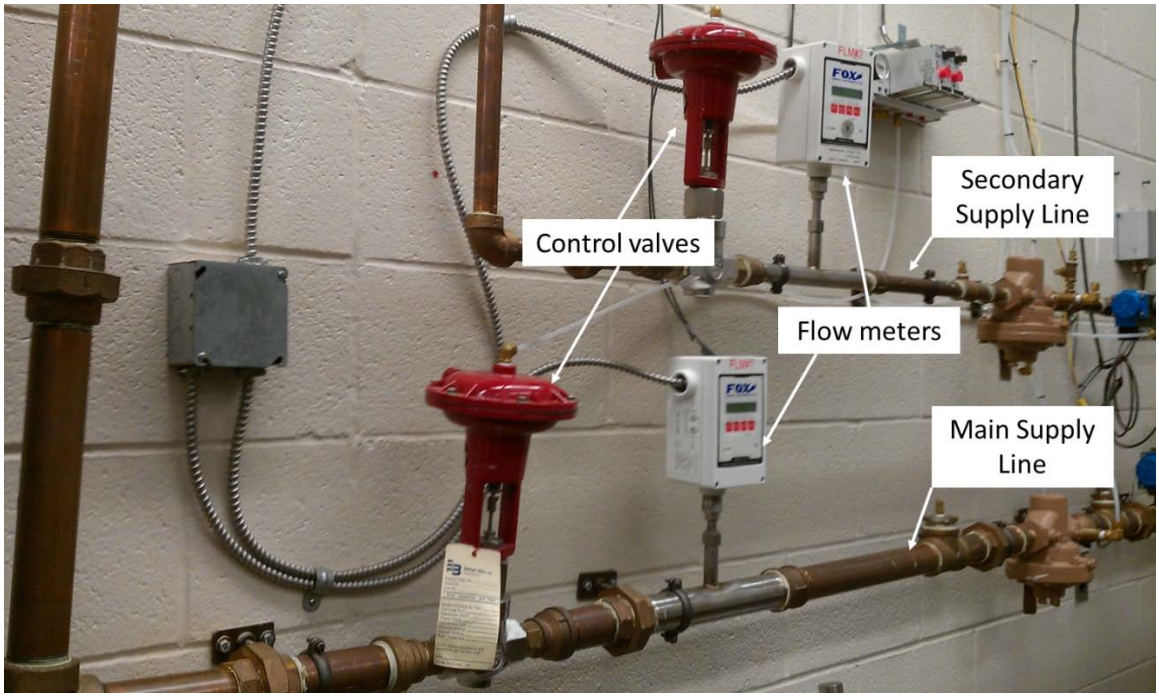

Figure 3.4: COAL Laboratory air supply lines and feedback controls

Fuel is supplied to the research section via several MKS flow controllers. Air and ethylene (C_2H_4) routed to the igniter box used MKS ALTA 1480A flow controllers with a maximum flow rate at 50 and 15 SLPM, respectively. MKS ALTA MC20 controlled the

propane (C_3H_8) travelling to the UCC section injectors. The MKS flow controllers have an accuracy of +/-1 % of the measured value and were controlled using an MKS 247D 4-channel control box. LeBay [17] described the addition of an Algas ZIMMER electric propane liquid-to-gas vaporizer. The vaporizer is capable of supplying 350 SLPM of gaseous propane from three 500-gallon liquid propane supply tanks. This allows for over 45 hours of testing before the supply tanks have to be refilled [17]. Liquid fuel is also available for use in the laboratory and is supplied using an ISCO Model 1000D syringe pump. Liquid fuel can be supplied at a rate up to 408 mL/min +/-0.5 % of the flow value. In the laboratory, liquid fuel is prone to pooling, as reported by Drenth [14].

In addition to the air and fuel facilities, thermocouples (Omega K-type, range 73-1523 K, +/-0.75 %) are in place to measure various temperatures depending on the combustor being analyzed. For UCC research, the thermocouples measure the inlet and exit temperatures of the core flow as well as the exit temperature of the seeder box. Pressure transducers are also in place in order to measure static and differential pressures. Dwyer model 682 pressure transducers measure the inlet pressure of both the core and UCC sections. Dwyer model 655-5 differential pressure transducers measure the pressure decrease across the UCC and core section. The pressure transducer and thermocouple locations can be found in Figure 3.5.

Anderson [26] developed a computer control code using National Instruments LABVIEW. The code not only collects all data inputs, but it is also used to control all air and fuel supply to the UCC. To facilitate the data acquisition for each experimental technique, LeBay [17] built a gigabit Ethernet network for all of the laboratory computers. By utilizing TightVNC v1.3.10 remote desktop software, LeBay was able to

centralize the control of the laboratory optical measurement techniques. This network, in addition to a derivative of Anderson's LABVIEW code, enables control over the air and fuel supply, an electronic translation stage, PIV, PLIF, and HSV image acquisition, and laser alignment to a wave meter from one centralized control station. Additionally, a US Robotics DroboPro FS network storage system was installed to allow up to 16 terabytes of experimental data storage. A manual on how to use the different equipment in the laboratory and control the facility can be found in Appendix A.

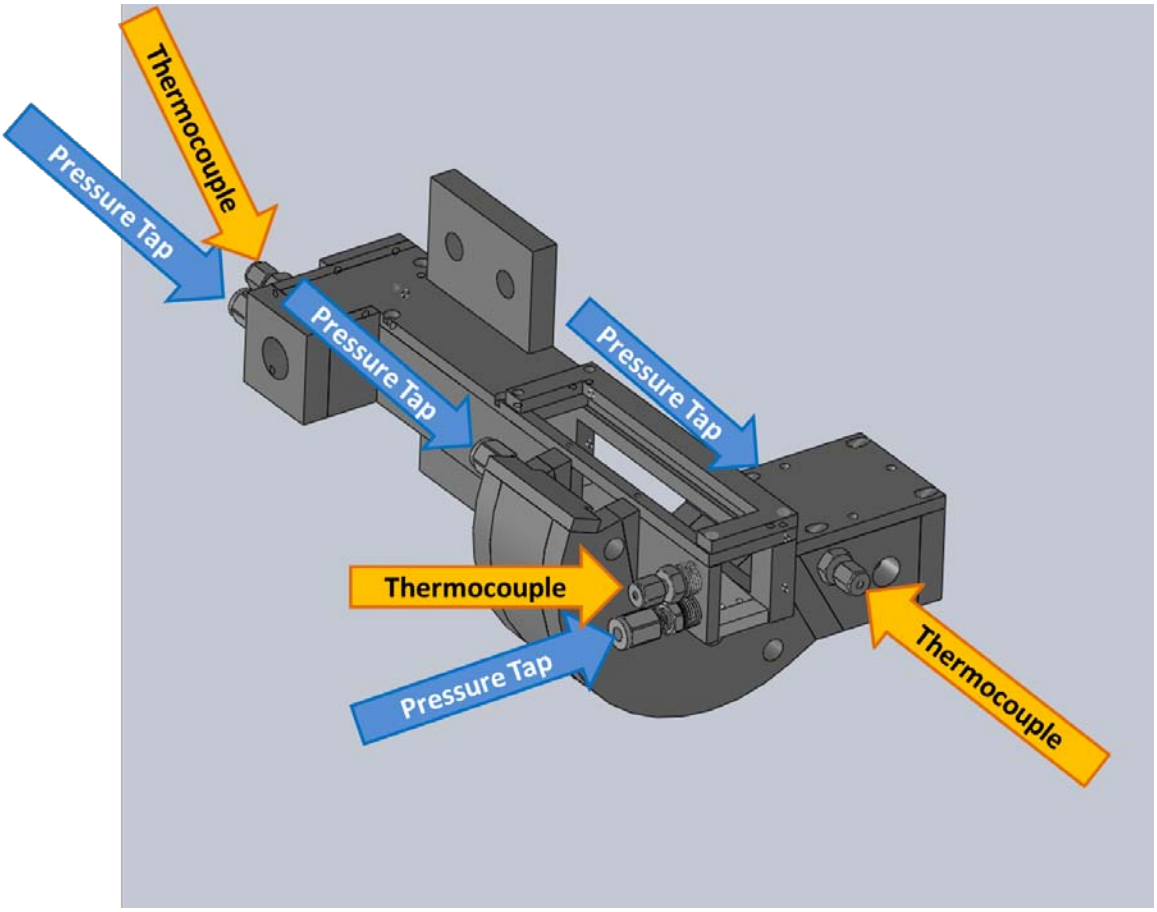

Figure 3.5: Static pressure and temperature measurement locations on the test section

Laser and camera positions were fixed within the confines of the COAL Laboratory. To have the ability to acquire data at different orientations, the test section

needed the ability to move. The AFIT sector was mounted to vertical and horizontal translation stages in order to adjust its orientation. The horizontal movement was established by an electronic translation stage, a Newport ILS50PP, as seen in Figure 3.6. A Newport ESP350 controller was used to direct the movements of the electronic translation stage. The vertical translation stage was a NRC 270 mechanical translation stage.

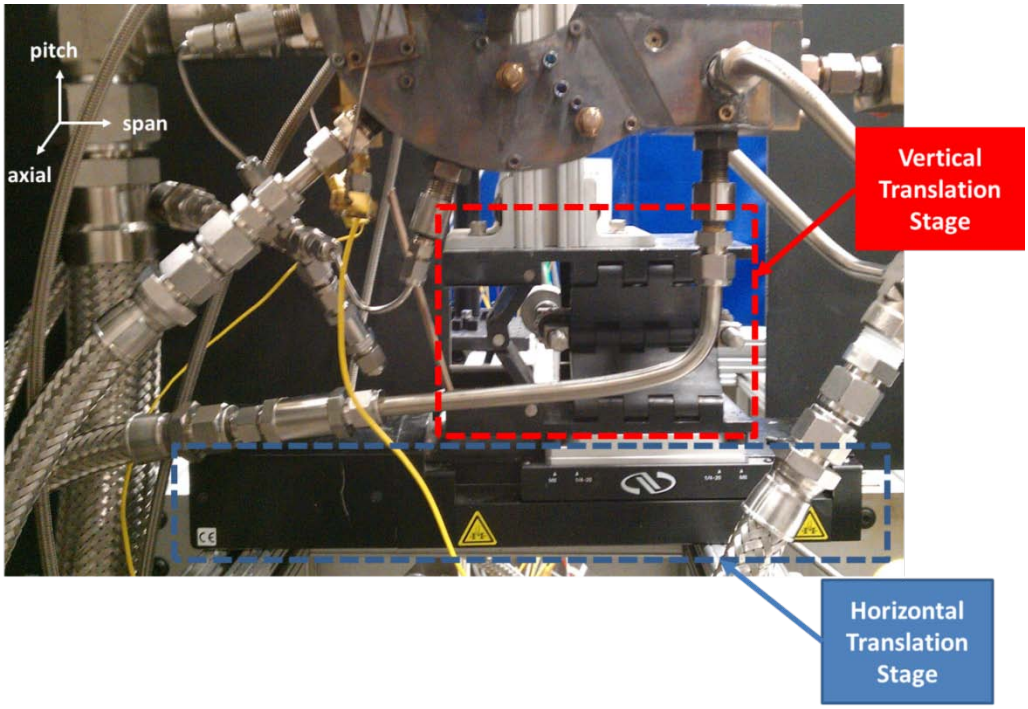

Figure 3.6: Translation stages and coordinate system for the sector

3.2.1 Improvements to COAL Laboratory

One of the future research goals is to adapt the UCC concept to a fighter-sized aircraft engine. As part of the research to accomplish this goal, a new test section is currently being designed and constructed around a realistic engine concept. The new test section, with a 0.38 m radius, is anticipated to consume nearly 2 kg/s of air. In addition to the increase in facility air demands, the new rig will also have higher fuel demands and

increased exhaust loads. Several improvements were undertaken during this work in order to provide the facility capabilities necessary to operate the future fighter-sized test section. The following sections will describe the enhancements made to the COAL Laboratory to increase the air flow capabilities as well as a combustion analysis in the chemical equilibrium code CHEMKIN™.

3.2.1.1 Enhancement to Flow Capability

The first challenge was to provide 0.6 kg/min of air to the UCC section of the larger UCC concept. The current air facilities could not sustain the necessary flow requirements due to the air supply loads by other laboratories located at AFIT. Therefore, a dedicated air compressor, an Ingersoll Rand H50A-SD, 50 hp oil free compressor, was identified and purchased to provide dry, compressed air to the larger concept. The compressor is capable of producing 186 cfm of air at 125 psig. The capability of the compressor exceeds the upgraded flow requirement and can provide up to 1 kg/s of air at atmospheric conditions.

The new compressor needed to be plumbed into the laboratory to be used for the new rig. The existing air supply lines were sized for much smaller quantities of air and included choke points at the pressure reducing valve and the flow controller. Therefore, it was necessary to add a third line to utilize the new air compressor and maximize the laboratory testing capabilities. The new high capacity line contained a Flowserve MaxFlo 3 control valve capable of 0.6 kg/s of air at maximum flow rate. A Fisher 299 pressure reducing valve was also purchased to drop the supply pressure to the desired control pressure. This air would then be metered to the test stand. The mass flow rate would be measured with a Fox Thermal Instruments FT2 flow meter. The FT2 meter

quantifies the mass flow rate of the line, with an accuracy of +/-1 % of the measured value, and returns the signal to the laboratory's control software. In order to accurately measure the flow, the line diameter was increased to 3 inches to ensure laminar flow through the FT2 meter. This line is shown in blue in Figure 3.7.

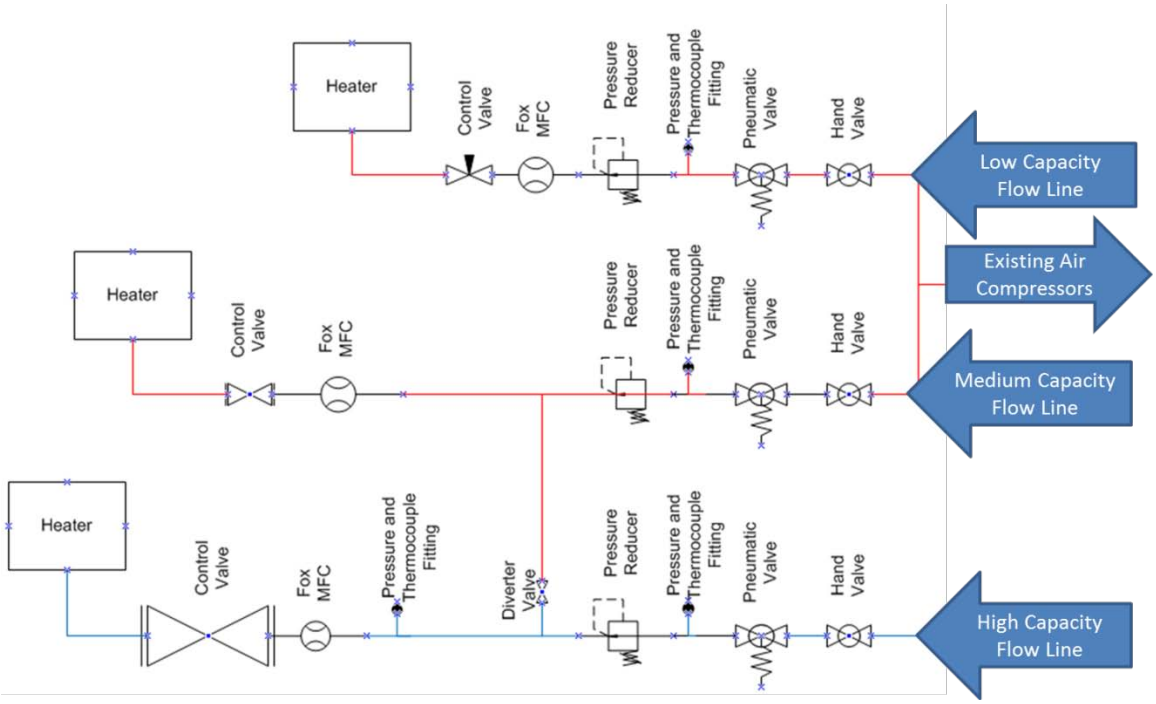

Figure 3.7: Flow path drawing depicting the high capacity flow line

As mentioned before, the existing lines had choke points at the pressure reducing valve and the control valve. These valves also limited the maximum flow capabilities of the line. In order to have a medium capacity flow line, a Flowserve MaxFlo 3 control valve was purchased with the capability to provide 0.3 kg/s of air at maximum capacity. A Fisher 299H pressure reducing valve was also purchased to replace the existing pressure reducing valve. Together, the COAL Laboratory has the capability to flow up to 1 kg/s on the high capacity line, 0.3 kg/s on the medium capacity line, and 0.03 kg/s on the low capacity line.

3.2.1.2 CHEMKIN™ Analysis

As mentioned in the prior section, a future goal is to adapt the UCC concept to a fighter-sized turbine engine. One upgrade to the current laboratory facilities needed is the ability to remove a higher quantity of UCC exhaust from the laboratory. To prepare for this increased load, a computer model was created to represent the fighter-sized UCC and its exhaust products. The model's data would be used in conjunction with numerical results from Bohan [3] (the model being a chemical equilibrium based analysis while Bohan used a fluid dynamics based analysis) to provide expected temperature and emissions results for the larger UCC emissions. The results could then be used to help size the future exhaust system, as well as give an indication of the exhaust products to be expected from the current UCC test apparatus. The UCC model was created and analyzed using the chemical equilibrium code CHEMKIN™ [28].

For the analysis, a 2-species model of air (O_2 and N_2) was used for the oxidizer, and propane (C_3H_8) was used for the fuel. The reactants were taken to complete combustion with standard products (CO_2, H_2O, and N_2). CHEMKIN™ requires three input files to create a chemical property set suitable for analysis. The requisite files were gas kinetics, thermodynamics, and gas transport. The files contain detailed information about intermediate combustion species and dictated how a reaction will occur. For this analysis, the GRI-Mech 3.0 files were used. The GRI-Mech 3.0 software was developed at University of California, Berkeley and is an "optimized mechanism designed to model natural gas combustion, including NO formation and reburn chemistry" [29].

The analysis used the Perfectly-Stirred Reactor (PSR) and the Plug Flow Reactor (PFR) models in CHEMKIN™. The UCC section was modeled as a series of

PSR reactors while the axial exit of the combined products was modeled as a PFR as shown in Figure 3.8. As conceived, there would be one fuel injection per vane cavity in the core section. Therefore, each PSR reactor represents one fuel injection location of the UCC section.

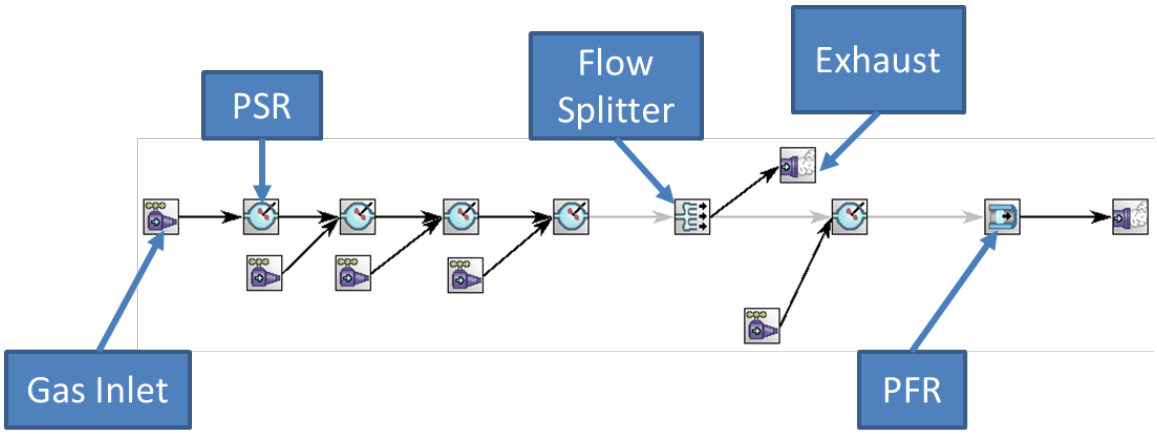

Figure 3.8: UCC flow diagram for CHEMKIN™ analysis model

Fuel was provided at a rate consistent with maintaining an equivalence ratio of 2.2 in the UCC section. The results reported by Bohan [3] were used to determine the necessary air and fuel rates. Bohan found that the reactants only reside in the UCC section for $0.0024\ s$ before exiting into the core section. The residence time corresponds to about $3/20^{th}$ of a full annulus. Consequently, at any cross-section of the UCC cavity only $3/20^{th}$ of the mass was present. Therefore, the total mass flow rate (air and fuel) was set to 0.0257 kg/s.

The decision was made to model $1/5^{th}$ of the full annulus instead of $3/20^{th}$. This would replicate three upstream fuel injectors whose products should begin to exit at the fourth injection location as predicted by Bohan. The fourth fuel injector was modeled as the fuel injector directly over the vane cavity. As a result each PSR had the volume of $1/20^{th}$ of the full annulus, or $0.000269\ m^3$. This assumed a rectangular cross section that

was 0.048 m on edge and a mean diameter of 0.35 m for the full annulus. The inlet supplied propane (C_3H_8), O_2, and N_2 to the reactor and the products from any upstream reactors. For the first PSR, the reactants were brought in at a temperature of 532 K which was the minimum temperature the fuel-oxidizer mixture could enter into the circumferential cavity and begin combustion before entering the downstream PSR. The temperature was used to simulate the preheating of the fuel that would occur during ignition. The temperature for the reactor was set to 1600 K. This was the minimum reactor temperature that could sustain combustion through the entire PSR. The pressure in the reactor was set to 1atm.

A PSR was used to model a mixing zone where the UCC flow converges with the core flow at a vane location. The volume for this zone was calculated to be 0.0004513 m^3 based on $1/20^{th}$ of the area of a disk with an inner radius of 0.3175 m and an outer radius of 0.3475 m multiplied by a depth of 0.048 m. Even though the model is depicting $1/5^{th}$ of the mass flow in the circumferential cavity, only $1/20^{th}$ of the flow exits into the mixing zone; therefore, the mixing zone (and the core flow section) needs to be only $1/20^{th}$ of the sector. As a result, ¼ of the products from the upstream PSRs was directed into the mixing zone while ¾ of the products were exhausted. Core air was brought into the mixing zone at 366 K. This temperature was the estimated temperature of air coming off a compressor as used by Bohan [3]. The core air was contained only O_2 and N_2. It entered into the reactor at a mass flow rate of 0.097 kg/s. This reactor was also set to a temperature of 1600 K and a pressure of 1atm.

The core section was modeled as a PFR with a cross sectional area of 0.003134 m^2. The PFR varied in length allowing the author to track parameters with downstream

distance. A maximum length of 0.112 m was used. The inlet to the PFR brought in the products of the mixing zone. This reactor was also set to a temperature of 1600 K and a pressure of 1atm.

Once the model was constructed, a parametric study of the system was performed. The first study was maintaining the equivalence ratio in the UCC section at 2.2 while the mass flow of the core flow was varied. The study effectively changes the overall equivalence ratio between the fuel and the total mass flow of air. Figure 3.9 shows that as the overall equivalence ratio drops, the temperature of the products in the PFR also drops. The trend is reasonable because as the local equivalence ratio drops below the LBO point, the reactions are quenched. This will cause the reactions to cease, and due to the lack of heat release, the temperature will approach the temperature of the core air (366 K). A temperature such as this would be unacceptable for the turbine inlet for it could not extract the requisite amount of work. An additional concern for this scenario is the concentration of UHC left behind by the quenched flame. The UHC will proceed downstream into the turbine leading to a potential secondary heat release that would be detrimental to the turbines structural integrity.

Figure 3.9 (the legend depicting overall equivalence ration) also shows that as the overall equivalence ratio approaches one, the temperature approaches the adiabatic flame temperature of propane. The study indicates that the turbine will see higher temperature if the engine is unable to keep the expected core mass flow without changing the equivalence ratio in the UCC. Alternatively, if the engine entrains more core air mass, then the turbine temperature will drop and less work will be able to be extracted. The

latter causing additional UHCs to be present in the turbine section with potential for secondary heat release when interacting with a blade cooling scheme.

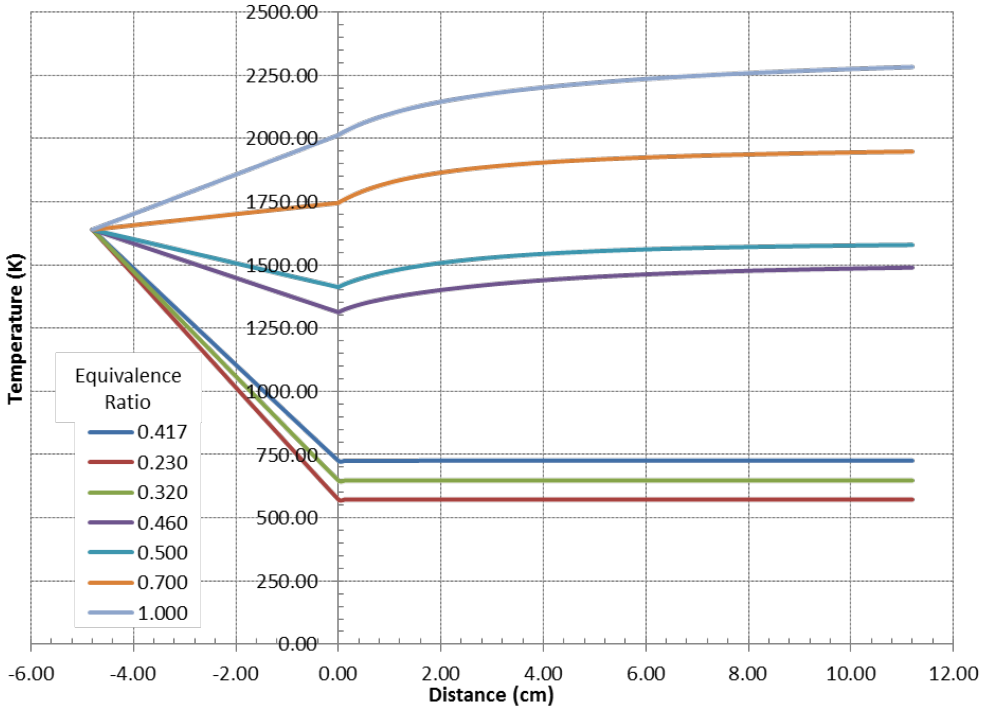

Figure 3.9: Temperature results as a function of PFR distance by varying the core mass flow

A second study done was to hold the core mass flow constant and vary the equivalence ratio of the UCC cavity. Because of the fighter-size UCC design basis, the amount of energy release needed in the UCC section was a specified amount. Therefore, the mass flow rate of the fuel is a fixed quantity at the design point. In order to change the equivalence ratio in the UCC section, it is necessary to change the mass flow rate of the air in the UCC cavity. For this study, equivalence ratio was varied from 0.5 to 2.5 by maintaining a fuel mass flow rate of 0.064 kg/s and varying the needed mass flow rate of air. In order to keep the total mass flow constant, the core mass flow rate was adjusted accordingly to the change in the UCC air mass flow rate.

Figure 3.10 summarizes the effects on temperature of variations in the UCC section equivalence ratio with downstream distance. The legend shows the percent of total mass going into the UCC and the corresponding UCC section equivalence ratio. It can be seen that at high equivalence ratios (fuel rich situations), the temperature is significantly lower in the core section. Any reactions occurring in the UCC section are quickly quenched and the temperature drops closer to that of the incoming core air. Alternatively, as equivalence ratio decreases the temperature rises. It is noted that the peak mixing zone temperature occurs at an equivalence ratio of 1.25 while the peak temperature in the PFR occurs at an equivalence ratio of 0.5. The difference occurs because 83.4% of the air is entering into the UCC section in the 0.5 case so the energy release is only able to raise the air temperature to 1500 K, and the marginal amount of core air coming into the mixing chamber that the heated products is quickly brought up to temperature. Whereas for an equivalence ratio of 1.25, only 33.3% of the total air is entering the UCC section and the heat release can more easily raise the bulk temperature. It is also noted that the temperature rises in the PFR for all cases at an equivalence ratio of less than 2.1. This is a result of the flame not being quenched and reactions continuing to take place in the PFR as shown in Figure 3.10 and Figure 3.11.

In addition to looking at the exit temperature, the amount of unburned hydrocarbons and OH present at the exit plane was investigated. The concentration of OH was used as an indicator of the completeness of combustion. Figure 3.11 shows three equivalence ratio cases and their UHC concentration on the left axis while their OH concentration is on the right. It can be seen at equivalence ratios of 2.1, 2.0, and 1.5, the concentration of UHCs dropped with downstream distance while OH concentration remained relatively

constant. This is consistent with the OH radical produced by the decomposition of UHCs replacing the OH radicals consumed as combustion continued. At an equivalence ratio of 2.2, the UHC concentration is constant and the OH concentration drops quickly indicating that the reaction has ceased to occur within the PFR.

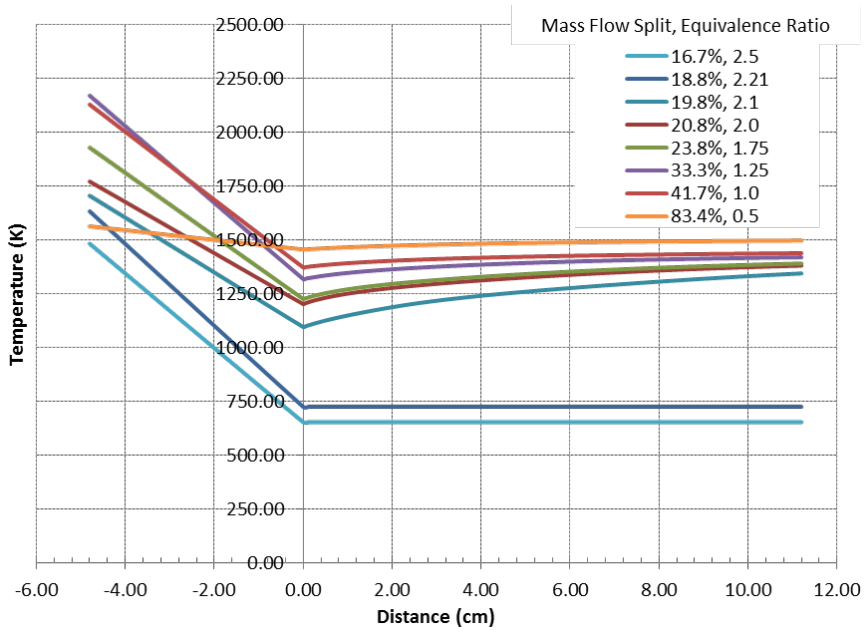

Figure 3.10: Results from varying the equivalence ratio in the UCC section

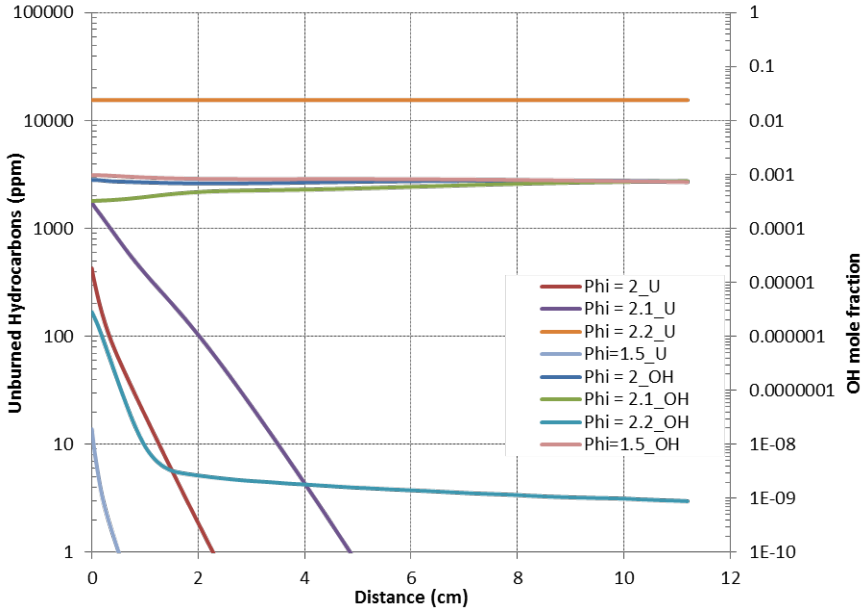

Figure 3.11: UHC and OH concentrations with downstream distance in the PFR

Some important conclusions can be drawn from Figure 3.10 regarding the specifications of the exhaust system. First, it can be seen that the exhaust from the circumferential cavity will have its highest temperature at nearly 2200 K with a mass flow rate of roughly 0.13 kg/s ($\Phi = 1.25$). Additionally, the highest mass flow rate will be at roughly 0.31 kg/s and a temperature of 1950 K ($\Phi = 0.5$). The latter also produces the highest turbine inlet temperature of about 1461 K with a core mass flow rate of 0.02 kg/s. These cases help define the maximum thermal mass the exhaust system would have to endure. However, there may be a case where a large mass passing through the system does not have the highest overall temperature but combined with its mass flow it has the largest thermal mass load.

In addition to sizing the exhaust system, this data was used to define the experimental space for the new sector. A typical goal for high performance engines is to have a very high turbine inlet temperature. This is the temperature seen at 11.2cm downstream in Figure 3.10. Figure 3.10 also depicts the diminishing return of decreasing equivalence ratio with respect to turbine inlet temperature. In order to determine the ideal operating equivalence ratio, several options were considered: a very low UHC concentration by 11.2cm, a low thermal gradient between the mixing chamber and the core flow temperatures, and a high turbine inlet temperature. It appeared that the equivalence ratio of 2.0 met all three of these conditions. Therefore, the fighter-size UCC combustor will likely focus on optimization around $\Phi = 2.0$ with only slight variations above and below this equivalence ratio. This concludes the numerical analysis in CHEMKIN™.

3.2.2 Flow Meter Calibration

In addition to adding new capabilities to the COAL Laboratory, each of the flow controllers (three air, one ethylene, and two propane) was calibrated using a BIOS Definer 1020 flow calibrator. The flow rate of each gas was varied within its typical operating range and recorded. Figure 3.12 shows a representative calibration curve. The input parameters were plotted versus the output reading from the calibrator. A trend line was developed for each of the flow controllers based on a linear relationship with the data and a zero offset. The trend line provided the new calibration constant for each flow controller. The LABVIEW program was modified to reflect the new constant. The remaining calibration curves can be found in Appendix B. Hysteresis in the flow controllers was also investigated. No controller showed a significant amount of hysteresis. Once the calibration had occurred, several points for each flow controller were selected at random to validate the calibration process. All points were less than one percent different from the desired input value. A detailed account of the calibration process can be found in Appendix A. Table 3.1 highlights the old calibration constants and the new calibration constants for each of the flow controllers. Due to the zero offset mentioned earlier, the calibration constants reflect the slope of the calibration curve.

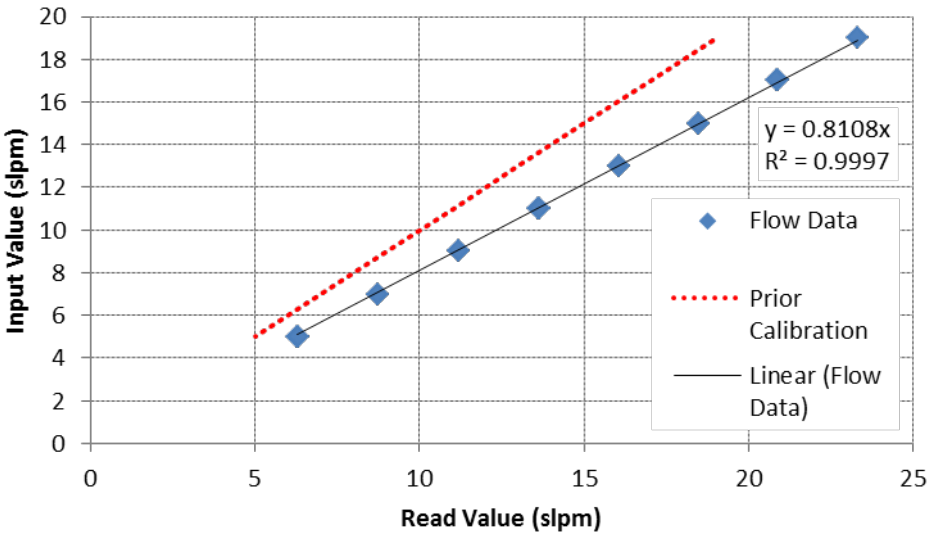

Figure 3.12: Calibration curve for the igniter air showing old calibration curve, the corrected calibration curve, and the correlation coefficient

Table 3.1: Calibration constants for the COAL Laboratory flow controllers

Gas	Old Constant	New Constant
Air (core section)	0.71428	0.8625
Air (UCC section)	2.5	2.875
Propane (Injectors 1 &2)	1	1.0007
Propane (seeder box)	1	1.0007
Propane (igniter)	1	0.8108
Ethylene (igniter)	1	1.2883

3.3 Additions to the AFIT UCC Test Section

A short-coming of the AFIT test section was that while the circumferential cavity replicated two injectors, it did not offer the ability to change the upstream characteristics

of the flow. As reported by Bohan [3], a steady-state collection of mass occurs in the UCC section based on the processes specific residence time. This collection can cause the combustion products to exist in the circumferential cavity for multiple vane passages before exiting into the core flow. Therefore, a level of uncertainty existed as to what the appropriate residence length was needed for each fuel injector before the reactants were properly combusted. The test section configuration to this point may not have been accurately representing the full annulus flow characteristics. To remedy this issue, LeBay [17] developed a box (see Figure 3.13) that housed an additional fuel injector and air inlet with the ability to vary the upstream conditions. Assuming the flame started in the box, the resident length was nearly doubled for the UCC section. The box had a secondary purpose to allow the addition of PIV seed. For this purpose, it was termed the 'seeder box'.

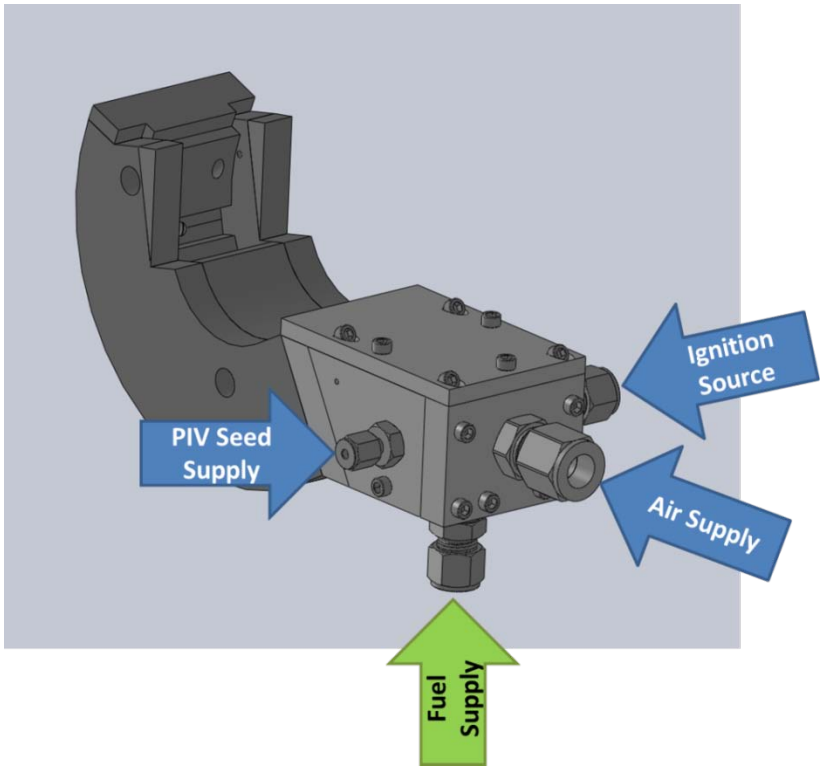

Figure 3.13: The seeder box attached to the UCC section

The seeder box was attached to the upstream opening of the UCC section. Because of its proximity to the optical access in the core section, the box was affixed so it turned away from the UCC section's radius of curvature. In order to make this connection, a curved piece was installed within the seeder box to ensure the flow had a smooth transition from the seeder box to the UCC section. Highlighted in Figure 3.13, the box was 0.064 m long, 0.038 m wide, and 0.032 m deep. The box had an opening for air to be provided from the most upstream position creating a significant cross flow in the circumferential cavity. It also included an opening for silicon carbide seed particles to be introduced, an opening for a fuel injector, and an opening for an ignition source. For this work, the ignition source was an ethylene-air mixture ignited by a standard automotive sparkplug. In addition, pressure transducers and thermocouples could be attached to the box in order to estimate the density of the mixture, based on the ideal gas law, as it entered the UCC section.

The decision was made to have the seeder box replicate the four upstream injectors not included in the UCC section. The fuel injector in the seeder box was controlled by its own mass flow controller. This allowed the operator to vary the fuel between the seeder box and the two fuel injectors. LeBay [17] developed standardized flow rate values for a variety of flow conditions. During the development of these flow rates, LeBay found that the flame would not stay lit in the UCC section when four injectors worth of fuel was delivered to the seeder box. LeBay found that at this configuration the flame would either sputter or blow downstream of the UCC section. Neither case was acceptable for trying to replicate the full annulus. LeBay decided to split the fuel so that 44 % (or roughly 2.7 fuel injectors) of the necessary fuel was delivered to the seeder box and each

fuel injector flowed 28 % (or 1.66 fuel injectors) of the fuel. The decision on dividing the fuel flow in this manner had unintended consequences that will be addressed later in the work. Once the issue of maintaining a lit flame was resolved, LeBay finished the development of the standard operating parameters. Fuel flow rates were based upon the bulk equivalence ratio desired in the UCC section. These parameters can be found in Table 3.2. It is important to observe that the mass flow rate in the core section is one-sixth of the mass flow rate of the full annulus at that specific MFR due to the AFIT test section having one-sixth the volume of the full annulus.

Table 3.2: Typical operating parameters for the AFIT UCC test section

Centrifugal Loading (g's)	UCC Section Air (kg/min)	Core Section Air (kg/min)			Propane $\Phi = 2$ (slpm)		
		MFR = 0.1	MFR = 0.2	MFR = 0.3	Seeder Box (44 %)	Injector 1 (28 %)	Injector 2 (28 %)
500	0.3714	0.6189	0.3094	0.2063	11.257	7.044	7.044
1000	0.5252	0.8753	0.4376	0.2917	15.922	9.961	9.961
2000	0.7428	1.2379	0.6189	0.4126	22.517	14.087	14.087

Another short-coming of the AFIT test section was briefly mentioned in Chapter 2. The guide vane was placed in the bottom of the core section in order to have optical access from above. This means that only one side of the core section has a guide vane, and the optical window provides only a flat surface instead of the traditional airfoil shape. Bohan [3] studied the UCC section flow paths and concluded that the UCC products tend to exit at the top of the core section. These results concurred with Anderson's [13] results on the AFRL full annulus test rig. These results indicated that variations in the

geometry of the vane have an increased effect on the circumferential flow when the vane is facing the circumferential flow. This built the belief that the flow interactions between the UCC and core sections would only be accurately reflected by the AFIT sectional test rig if the vane was located on the top of the core section. Therefore, the core section was modified from LeBay's work in order to place the vane on the top of the core section. The modification was made modular so that multiple vane geometries could be explored. Three vane geometries were developed and are shown in Figure 3.14: a solid vane, a RVC, and a tiger claw vane.

The RVC and the tiger claw were developed to encourage the hot combustion products from the UCC section to migrate into the core section. The RVC, Figure 3.14b, was first proposed by AFRL [2,5] to help the UCC section flame migrate from the OD to the ID of the core section. LeBay [6] noted that the flow eagerly travelled across varying span distances causing the flow to impinge upon the ID wall creating a large temperature gradient. The location of the impingement varied based on MFR, as seen in Figure 2.10. Bohan [3] numerically confirmed this effect. The changing of impingement location is due to the changing of the injection angle. The variation in location makes it increasingly difficult to cool the vane and the HPT components.

While the objective of the RVC was to encourage products from the UCC section, it is not ideal to have all the hot products on the ID of the core section. The tiger claw was created to try and mitigate the changes in injection angle with changes in MFR. Three channels were created, as seen in Figure 3.14c, to change the impinging flow from a radial to an axial trajectory in the core section. The channels are designed to create three separate low pressure regions at the intersection of the UCC and core section. The

circumferential flow will then be coerced into one of the three channels. Each channel was designed to have an upward slope with axial downstream distance at the interface of the UCC and core section. This upward slope encourages the flow to stay within each channel instead of allowing the flow to bleed into the downstream channel. The channels then direct the flow from the radial to axial directions without allowing the flow to impact the ID of the core section. The channels are intended to create a more uniform distribution of flame across the span of the vane. AFRL explored the use of multiple channels for migrating flow from a trapped vortex combustor, but there is no known design that attempts to turn the flow parallel to the axial direction [30]. The reader may notice holes in the tiger claw vane (see Figure 3.14c). These holes were placed in the vane for static pressure measurements that are not in this research and can be ignored. With a predictable, uniform temperature distribution across the vane, an effective film cooling scheme can be developed to cool both the vane and the HPT components.

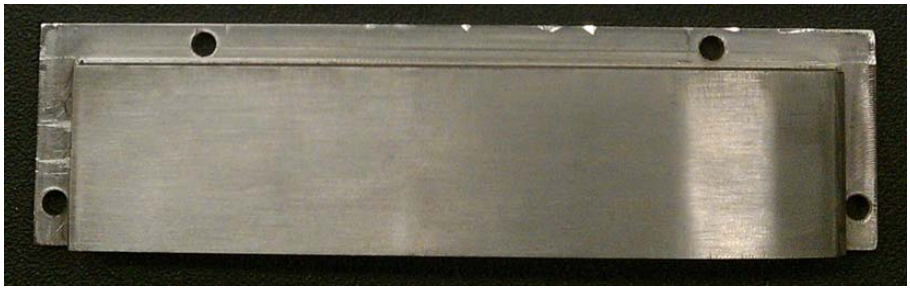

(a)

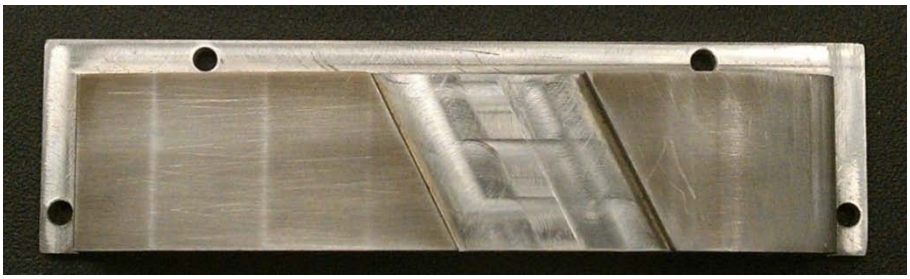

(b)

(c)

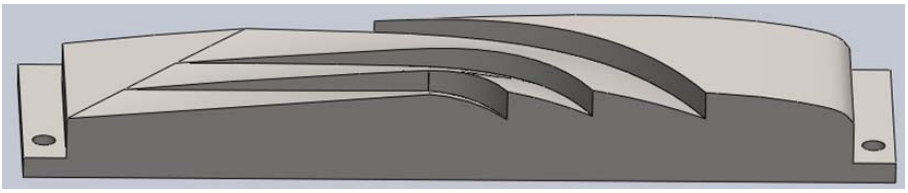

(d)

Figure 3.14: Core section vane configurations studied in this work were (a) solid airfoil, (b) radial vane cavity, (c) tiger claw, and (d) tiger claw profile

3.4 HSV Experimental Test Methodology

Fundamental to this research was the ability to show changes in the flame's characteristics as operating parameters and the core section vane geometry were varied. In order to accomplish this, an experimental method had to be employed that was able to show the flame's position, intensity, steadiness as well as its efficiency and exhaust products. High-speed video was chosen to meet the need to document flame position, intensity, and steadiness. The HSV allowed for immense amounts of flame data to be collected in a small amount of time. The following sections will discuss the HSV experimental setup and tests conducted and how these are used to characterize the dependence of the flame's properties on operating parameters and vane geometry.

3.4.1 HSV Test Setup

High speed video data was collected with a Vision Research Phantom V12.1 Color camera. The camera was capable of capturing images at frequency of 1 MHz with a resolution of 128 x 8 pixels. In full resolution, 1280 x 800, the camera was capable of capturing images at 6.2 kHz. The majority of HSV collected was done at a resolution of 800 x 200 and at 5 kHz. At frequencies higher than 5 kHz, exposure time was short enough that additional light was needed in order to detect a flame. Artificially illuminating the flame could be avoided if an exposure time of 190 μs was used at a frequency of 5 kHz. The camera gain was set to 10 to produce a clear but unsaturated video. In conjunction with the camera, a Nikon AF Micro-NIKKOR 60 mm lens was used.

The Phantom V12.1 camera was controlled using the Phantom Control Center (PCC) software. The software not only enabled the capture of HSV, but also

balanced the lighting and removed noise from the image signal. In addition to setting the camera gain to 10, the camera gamma and saturation settings were fixed at one. A white balance was accomplished using the PCC software to improve color capture by the camera. Included in the software was the ability to remove noise from the signal via a current session reference (CSR). The lens cover was placed on the camera to create a pure unsaturated image. An image was captured and pixels detecting a signal were identified. The software considers this as a pixel by pixel bias and removes the bias from every image after a CSR was accomplished. A CSR was accomplished once at the beginning of testing. The CSR adjusted the image acquisition for thermal changes as the camera reached its operating temperature. Figure 3.15 is a typical example of before and after a CSR. It is easy to tell that before one accomplishes a CSR (Figure 3.15a), there is a red channel bias on the left side of the image. After the CSR is accomplished (Figure 3.15b), the image looks uniformly colorless. In addition, an average of pixel intensity post-CSR was calculated to determine the level of noise in the signal. From Figure 3.15c, it was determined the level of noise in the signal is below an intensity level of 10. The noise floor set the minimum signal strength level used throughout the analysis in which any signal below an intensity of 10 was discarded. After an hour, a set of images was recorded and it was observed that the noise floor remained below an intensity level of 10.

The Phantom camera was placed in three different locations depending on the purpose of the data being collected. Figure 3.16 shows the camera placed above, below, and to the side of the core section. Placing the camera above and below allowed the chord-span plane to be captured. The chord-span plane was the plane of interest for

studying flame migration from the UCC to the core section. From the side, the chord-pitch plane could be studied for frequency analysis and depth of flame in the core section.

(a)

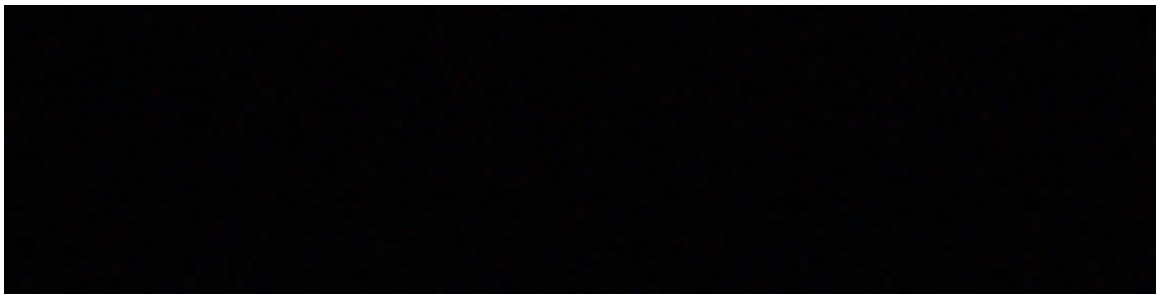

(b)

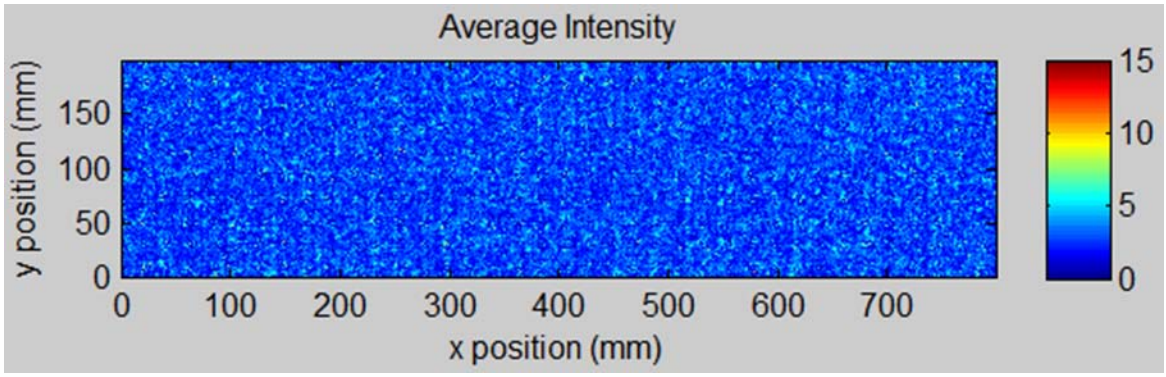

(c)

Figure 3.15: A HSV image (a) before and (b) after a CSR as well as (c) noise in an image

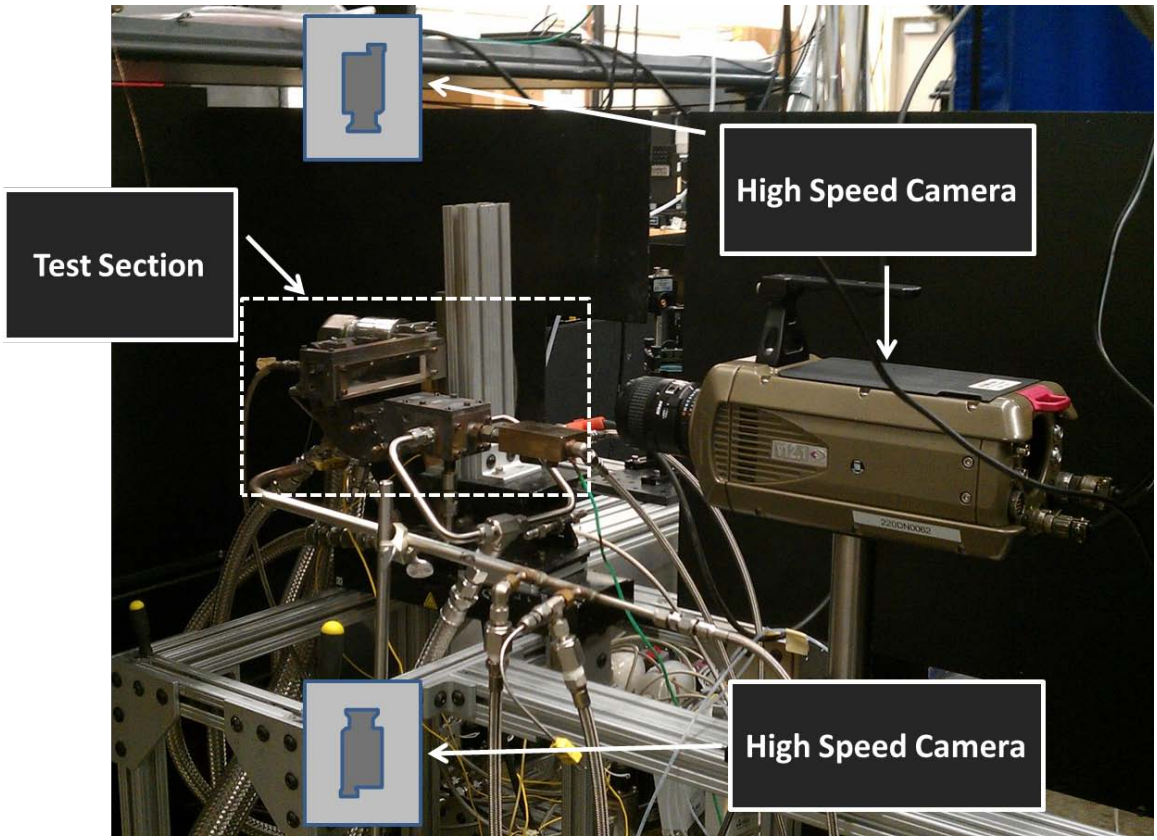

Figure 3.16: Position of the HSV camera for flame migration studies (above and below) and frequency analysis (side – as shown)

3.4.2 HSV Test Plan

The collection of HSV data allowed the qualitative comparison of the location and shape of the flame in the core section. The first objective of the HSV experiments was to document how the flame in the core section reacted to changes in operating conditions. As mentioned previously, LeBay [17] showed that MFR greatly affects the way the flame enters into the core section as seen in Figure 2.10. Therefore, a series of experiments were conducted to document the effect of changes in MFR. Secondly, LeBay showed that centrifugal loading only changed the intensity of the flame in the core section, but not the shape. Therefore, centrifugal loading was studied sparingly.

After the dependence on operating parameters of the AFIT UCC section was documented, the airfoil geometries and location were varied. As discussed previously, the AFRL full annulus had the vane facing the circumferential flow and CFD results confirmed that the products have a tendency to exit on the vane facing the circumferential flow. For this reason, the vane was placed on top of the core section with the ability to view the flame from the bottom. In addition, the shape of the vane was also modified. A standard solid airfoil shape was used. The RVC was also used as AFRL has extensively documented its ability to coerce hot products to exit into the core section. Flows with both of these vanes, however, are known to have a dependence on operating parameters, and the RVC produced unorthodox temperature profiles.

For these reasons, the tiger claw vane was also tested. The tiger claw features a novel three channel design that should decrease the flow's dependence on operating parameters as well as providing a low pressure zone to encourage hot products to exit the UCC section. By optically capturing the flame's position within the core section, the desensitization of the flow by the tiger claw was shown. Table 3.3 encapsulates all of the HSV experiments that were conducted. The last column is Table 3.3 describes the percent of the total fuel flow delivered to each location. The baseline case was considered to be Case 21 due to the recommendations from previous research that this was a representative operating condition for a UCC.

Table 3.3: HSV Test Matrix

Test Case	Core Section Vane	Position in Core Section	G-load (g's)	MFR	Fuel Split (%) (Seeder Box/ Injector 1/ Injector 2)
1	Solid	Top	1000	0.2	66/16.5/16.5
2	Solid	Top	1000	0.2	66/0/16.5
3	Solid	Top	1000	0.2	66/16.5/0
4	RVC	Top	1000	0.2	66/16.5/16.5
5	RVC	Top	1000	0.2	66/0/16.5
6	RVC	Top	1000	0.2	66/16.5/0
7	RVC	Top	1000	0.3	66/16.5/16.5
8	RVC	Top	1000	0.1	66/16.5/16.5
9	Tiger Claw	Top	1000	0.2	66/16.5/16.5
10	Tiger Claw	Top	1000	0.2	66/0/16.5
11	Tiger Claw	Top	1000	0.2	66/16.5/0
12	Tiger Claw	Top	1000	0.3	66/16.5/16.5
13	Tiger Claw	Top	1000	0.1	66/16.5/16.5
14	Tiger Claw	Top	500	0.2	66/16.5/16.5
15	Tiger Claw	Top	2000	0.2	66/16.5/16.5
16	Solid	Bottom	1000	0.2	66/16.5/16.5
17	Solid	Bottom	1000	0.2	66/0/16.5
18	Solid	Bottom	1000	0.2	66/16.5/0
19	Solid	Bottom	1000	0.2	66/8/8
20	RVC	Bottom	1000	0.2	44/28/28

21	**RVC**	**Bottom**	**1000**	**0.2**	**66/16.5/16.5**
22	RVC	Bottom	1000	0.2	66/0/16.5
23	RVC	Bottom	1000	0.2	66/16.5/0
24	RVC	Bottom	1000	0.2	66/8/8
25	RVC	Bottom	1000	0.3	66/16.5/16.5
26	RVC	Bottom	1000	0.1	66/16.5/16.5
27	RVC	Bottom	1000	0.2	55/16.5/16.5
28	RVC	Bottom	1000	0.2	47/16.5/16.5
29	RVC	Bottom	1000	0.2	39/16.5/16.5

3.4.3 HSV Data Processing

The Phantom camera recorded each image as a combination of three colors (red, green, and blue) and stored the data set as a cinematic file. The cinematic files were then converted to multipage tagged image file format (TIFF). While the cinematic files contained 5000 images, a multipage TIFF is limited to 4470 images. For simplicity, the first 4000 images were analyzed or roughly 0.8 sec worth of data. The images were analyzed using a derivative of a computer code developed in MATLAB by LeBay [17]. The code can be found in Appendix C.

To begin the analysis, the computer code loads each TIFF image into a three-dimensional matrix (one dimension for each color). A relationship for the number of pixels per unit length was then calculated based upon a calibration image, as shown in Figure 3.17. Using a known horizontal surface in the image (i.e. the window edge), the image can be rotated to adjust for any tilt in the camera. The inclusion of the ruler aids in finding the conversion factor for number of pixels in a given length.

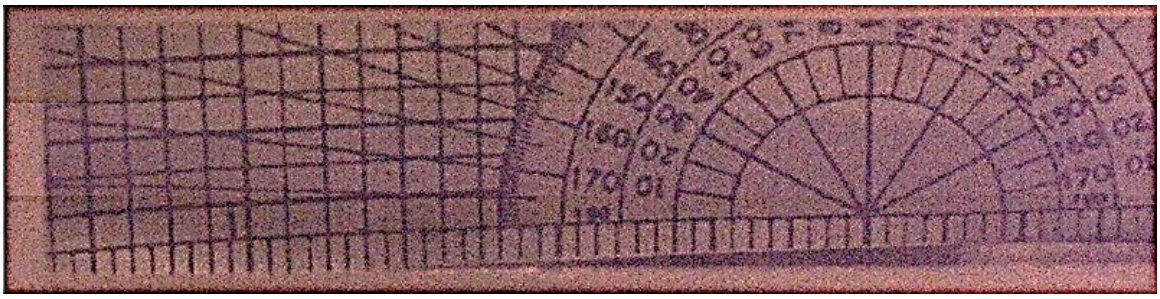

Figure 3.17: Typical calibration image for HSV data set

To explore the location of the flame in the core section, only the blue channel data was used. The blue channel data was used due to the chemiluminescence of the CH molecule being emitted as hydrocarbon bonds are broken (see section 2.6) [22]. The intensity of each pixel was time averaged to determine the average location of the flame using Equation (3.1).

$$\overline{I_{xy}} = \frac{\sum_{t=1}^{4000} I_{xy}(t)}{4000} \tag{3.1}$$

Additionally, the sample standard deviation in time at each pixel location was also calculated using Equation (3.2) to determine the fluctuations in the flame intensity.

$$s_{xy} = \sqrt{\frac{1}{3999}\sum_{t=1}^{4000}\left(I_{xy}(t) - \overline{I_{xy}}\right)^2} \tag{3.2}$$

If desired, a minimum signal strength threshold can be established and used as a filter. After the images have been averaged, any average intensity below the minimum threshold could be zeroed. This helped eliminate noise in the images. From here the results can be plotted to determine the average location of the flame and the area(s) of maximum fluctuation in the location of the flame. Figure 3.18a details the camera's perspective from the side, Figure 5.18b from the top perspective (used when the vane is located at the bottom of the core section), and Figure 5.18c from the bottom perspective (used when the vane is located on the top of the core section).

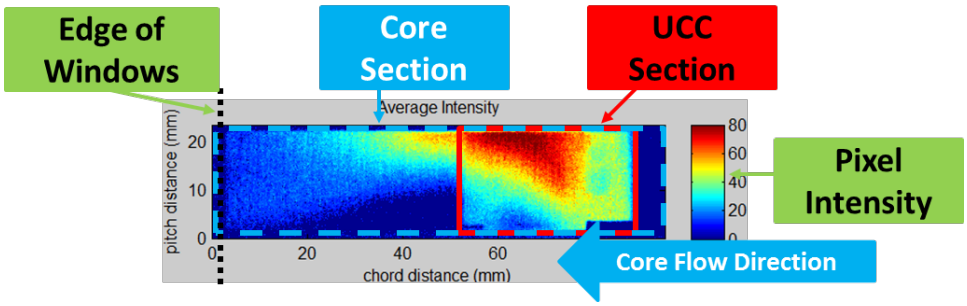

(a)

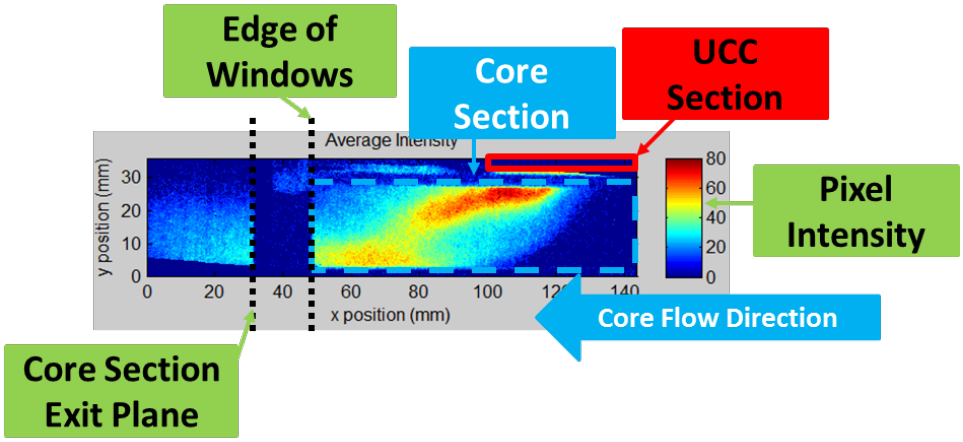

(b)

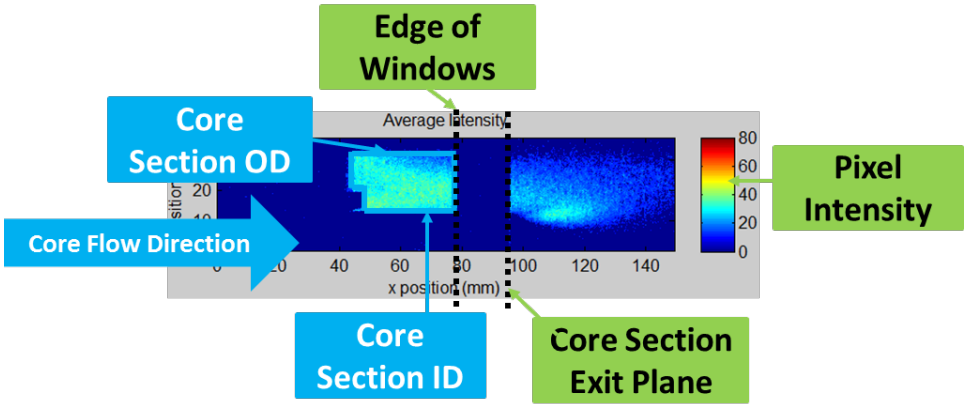

(c)

Figure 3.18: Details of the HSV results from (a) side, (b) top, and (c) bottom views

3.4.4 HSV Unsteadiness

Flame unsteadiness was quantified by taking a standard deviation of the processed data for each case. A typical standard deviation result is shown in Figure 3.19. From Figure 3.19, it can be seen that the pixel intensity within the UCC section varies significantly over the time span, while the pixel intensity is less unstable in the core section. These fluctuations give an indication to the unsteadiness in the flame. When used in conjunction with an averaged pixel intensity image, the standard deviation can identify where flame is present most often as well as the boundaries of the flame shape. The boundary of the flame may produce an average pixel intensity of less than ten and subsequently be filtered out; however, the standard deviation will show the fluctuations in pixel intensity of the flame boundary and help identify where the true boundary of the flame lies.

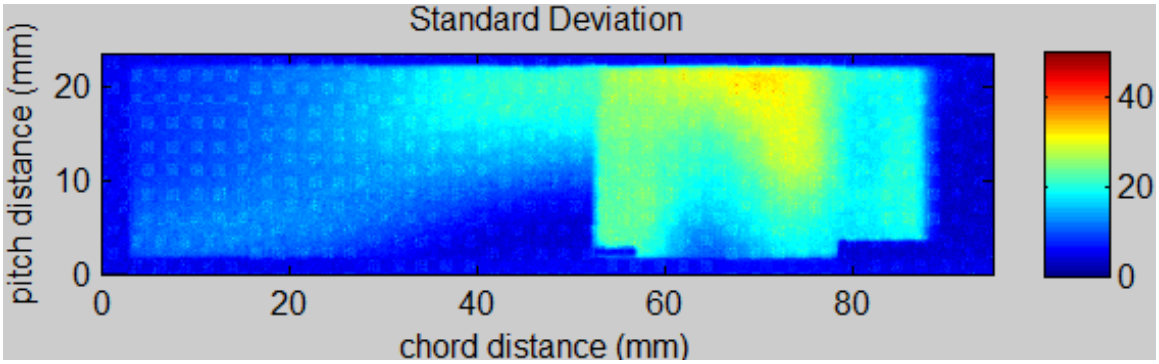

Figure 3.19: Representative image showing changes in flame location with time (side view)

3.5 Emissions Test Methodology

Considering the future integration of the UCC into a turbine engine, one must recognize that the UCC is designed to operate at high equivalence ratio. As such, incomplete combustion products are expected to exit the circumferential cavity and

interact with the core flow. Ideally the core flow will enable the species to quickly reach equilibrium and no combustible species would exit into the downstream turbine. Combustion completion within the turbine rotating section would result in a significant reduction in life and needs to be avoided. It is desirable to complete these reactions as early as possible while also minimizing the heat transfer to the airfoil surface. One specific problem is how to effectively cool the airfoil surface to avoid secondary heat releases in the turbine. Simplistically when UHC enter into the turbine and encounter film cooling air, the UHC react causing a heat release on the surface of the turbine component. This can be extremely detrimental to the equipment. Thus, minimizing UHC emissions from the combustor will minimize the risk of secondary heat releases in the turbine.

The objective of this investigation was to understand the conditions under which reactions might be expected to occur in the downstream turbine. One means to determine if this objective was being met was to consider the emissions of the UCC. Emissions data of key emissions constituents were collected in order to quantify the concentration and location on the core section exit plane. The following sections will describe the experimental setup and tests conducted.

3.5.1 Emissions Test Setup

Emissions data was collected using a suite of California Analytical Instruments, Inc. rack-mounted analyzers, as seen in Figure 3.20. Unburnt hydrocarbons were detected using a model 300-HFID analyzer with a detection range of 0 - 10,000 ppm carbon at a resolution of 0.01 ppm carbon. Nitrous oxides were detected using a model 400-HCLD analyzer with a detection range of 0 - 3,000 ppm at a resolution of 0.1 ppm. A model 300

analyzer was used to detect CO_2, CO, and O_2. The analyzer could detect 0 - 20 % CO_2 at a resolution of 0.02 %, 0 - 10,000 ppm of CO at a resolution of 0.01 ppm, and 0 - 25 % O2 at a resolution of 0.01 %.

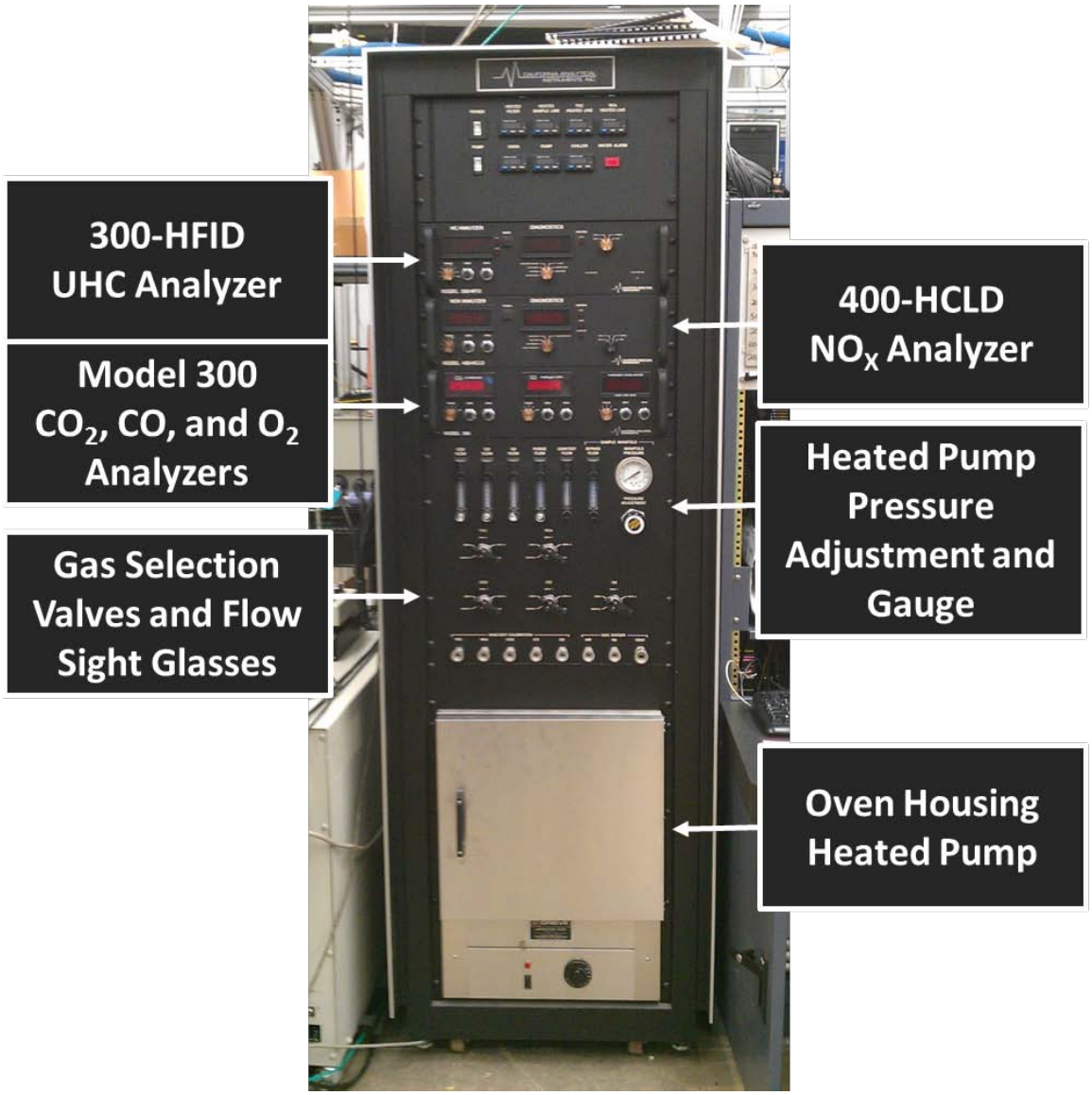

Figure 3.20: Rack-mounted emissions equipment including (from top to bottom) UHC, NO_x, CO_2, CO, and O_2 analyzers

The three analyzers were given at least one hour of warm-up time at start-up. This allowed each analyzer an opportunity to reach its operating temperature to minimize error

in results. After the one-hour warm-up, the three analyzers were calibrated using certified mixture grade calibration gases. Each analyzer had a specified gas to use for calibration and a set concentration of the gas. Table 3.4 concatenates the calibration gases, concentrations, and analyzer for the calibration process. Each of the analyzers contained a zero and span potentiometer for the calibration process. Two potentiometers, a zero and a span, were employed to adjust the linear relationship between the analyzers sensor and its output. The rack flowed pure nitrogen through each analyzer to set the zero point and then flowed the calibration gas to set the span. It is noted that for some of the analyzers, multiple concentration ranges could be chosen. Multiple calibration gases could be used to accurately calibrate the analyzer for the range of interest. For this work, the calibration gas closest in concentration to that anticipated from the experiments was used. Each analyzer had the ability to be calibrated at will. A full description of calibrating the gas analyzers can be found in Appendix A.

In order to protect the analyzers, emissions samples had to be kept above 450 K in order to keep all water content in a suspended state. The temperature requirement was met by having a heated pump draw the sample through a heated line at a flow rate of roughly 1 L/min. The sample passed through the heated sample probe, then a heated particulate filter, and into the heated line. Once the sample reached the analyzer rack, water vapor was removed and the sample divided and sent to the three analyzers. Data from the analyzers was recorded manually; however, the rack could be connected to a computer and LABVIEW could be used to automatically collect data.

Table 3.4: Gas analyzers and corresponding calibration gases

Constituent	Model	Calibration Gas	Concentration
UHC	300-HFID	C_3H_8	C_3H_8 - 900 ppm C N_2 - Balance
NO_x	400-HCLD	NO_x	NO_x - 98.2 ppm N_2 - Balance
CO_2	300	CO_2 (low range)	CO_2 - 4.75 % N_2 - Balance
		CO_2 (high range)	CO_2 – 9.75 % N_2 - Balance
CO	300	CO (low range)	CO - 1600 ppm N_2 - Balance
		CO (high range)	CO - 4800 ppm N_2 - Balance
O_2	300	O_2	O_2 - 5.00 % N_2 - Balance

The sample probe was located at a distance of one quarter of the airfoil chord downstream of the core section exit plane as seen in Figure 3.21a. The probe was heated and cooled by a Mokon H22103AJ Compact Heated Thermal Fluid System. The thermal fluid, a water-glycol mixture, was circulated between the sample probe and the Mokon unit at approximately 2.75 bar and a temperature of 450 K. This allowed the probe to be heated to 450 K prior to any measurements being made. When the UCC section was ignited, the Mokon unit acted as a cooler to ensure the probe did not reach its melting temperature when exposed to flame.

Emission measurements were made at 16 varying pitch and span locations at the exit plane of the core section as seen in Figure 3.21b. The sampling locations allowed for the development of a point-wise emissions profile or a spatially averaged collection of the results. Sampling occurred across the span of the airfoil at 21, 43, 64, and 86 %. The percent span was chosen to correlate with the interrogation planes LeBay [17] used for OH-PLIF experiments. The sampling positions corresponded to 10, 33, 57, and 80 % pitch. The percent span and pitch values are shown in yellow in Figure 3.21b.

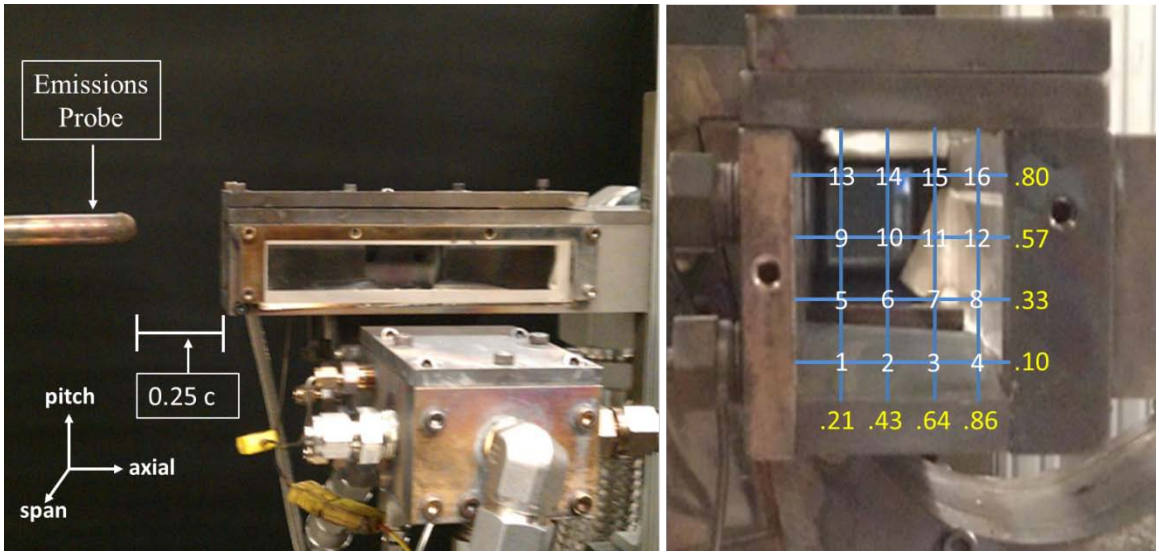

(a) **(b)**

Figure 3.21: Experimental setup showing (a) the location of the sample probe relative to the core section and (b) the sample locations

3.5.2 Emissions Test Plan

The emission data was used to directly satisfy the main objective of this work: to show the desensitization of the core section properties to changes in operating parameters. A group of experiments were conducted to characterize the exit plane constituents with the vane both on the bottom and top of the core section. These

experiments matched several cases recorded by the HSV experiments in order to use both the HSV results and emissions results to better understand the physics occurring in the core section. The characteristics gathered would be used to help design future UCC projects and modify the current AFIT UCC section.

Table 3.5 outlines the nine emissions data test scenarios. The cases were chosen to be able to directly show the effects on emissions by using the tiger claw airfoil as well as any changes in exit plane characteristics by having the vane on the top of the core section instead of bottom. Due to the emissions test cases directly matching several of the HSV test cases, the HSV test case numbers were used to track the emissions results.

Table 3.5: Emissions test cases

Test Case	Core Section Vane	Position in Core Section	G-load (g's)	MFR	Fuel Split (%) (Seeder Box/ Injector 1/ Injector 2)
1	Solid	Top	1000	0.2	66/16.5/16.5
4	RVC	Top	1000	0.2	66/16.5/16.5
8	RVC	Top	1000	0.1	66/16.5/16.5
9	Tiger Claw	Top	1000	0.2	66/16.5/16.5
12	Tiger Claw	Top	1000	0.3	66/16.5/16.5
13	Tiger Claw	Top	1000	0.1	66/16.5/16.5
14	Tiger Claw	Top	500	0.2	66/16.5/16.5
16	Solid	Bottom	1000	0.2	66/16.5/16.5
21	RVC	Bottom	1000	0.2	66/16.5/16.5

3.5.3 Emissions Data Analysis

The data collected from the three gas analyzers were evaluated in accordance with the SAE ARP 1533A [9]. The concentration results collected were transformed into EI values based on Equation 3.3. In Equation 3.3, Z was the constituent of interest (CO_2, CO, or UHC). The values gathered from the EI could be used to calculate combustor efficiency per Equation 3.4. The efficiency model used was enthalpy based accounting for reaction inefficiencies from CO production and the lack of hydrocarbon reaction (UHC). It is important to note that the 300-HFID analyzer was specifically calibrated for C_3H_8; therefore, concentration results from the UHC analyzer were multiplied by 3 (the number of carbon atoms in the propane molecule).

$$EI_Z = \left(\frac{[Z]}{[CO]+[CO_2]+[UHC]}\right)\left(\frac{10^3 MW_Z}{MW_c+\frac{y}{x}MW_H}\right)\left(1+\frac{0.00034X}{m}\right) \tag{3.3}$$

$$\eta_b = \left[1.00 - 4.346\frac{EI_{CO}}{H_c} - \frac{EI_{UHC}}{1000}\right] * 100 \tag{3.4}$$

3.5.4 Emissions Error Analysis

The known error for the emissions analysis was quantified using the stochastic approach outline by the SAE ARP [9]. To accomplish this analysis, the known error in full scale measurements must be known (see Section 3.5.1). The process adds "noise" to the measured values based upon a Gaussian distribution about a mean value. For this analysis, the noise was added to the measured value and the error was propagated through the EI calculations and burner efficiency calculations. Table 3.6 summarizes the percent error for each of the EI calculations based upon the stochastic approach. The uncertainty in the EI UHC comes from the limitations of the analyzer used. The range on the 300-HFID was set to 1000 ppmC for each of the tests. At this setting, the user is limited to reading only to the tens location. To reduce this error, the user would need to see about

how much concentration was going to be measured, then choose a range on the 300-HFID better suited for the expected concentration level. Due to time constraints, the source of this error was unable to be reduced.

Table 3.6: Uncertainty in the EI of varying constituents and the combustor efficiency

Parameter	Uncertainty (% of measured value)
EI CO	+/- 0.24
EI CO_2	+/- 0.22
EI UHC	+/- 28.8
η_b	+/- 0.28

IV. Modifications to Current Configuration

The AFIT UCC test apparatus underwent several modifications to either correct issues or respond to observations made by LeBay [17]. The main purpose of the modifications was to improve upstream conditions replication in the UCC section. This increases the accuracy of the sectional model in representing the behavior of a full annulus. The following sections will address the issues with the UCC configuration, what modifications were made and why, and will provide some preliminary results and consequences of the modifications.

4.1 Confirmation of Operating Conditions

Preliminary experiments conducted explored the emission products for operating conditions established by LeBay [17]. LeBay suggested that the ideal operating condition for the UCC was at an MFR = 0.2 and a g-loading = 1000 g. The results from the emissions testing were used to confirm LeBay's conclusions and to compare to the bulk emissions of a full annulus published by Zelina et al. [2].

4.1.1 Confirmation of Operating Conditions Test Plan

As outlined in Table 4.1, mass flow ratio, equivalence ratio, and the division of fuel delivery were varied individually to understand their effects. Mass flow ratio, as defined in Equation 2.4 was varied between 0.1 and 0.2. Due to a required heat release in the UCC section, a fuel rich environment was necessitated. As a result, the equivalence ratio, defined in Equation 2.11, was varied between 1.6 and 2.6 at 0.2 intervals. The g-loading was set at 1000 g's due to both LeBay's [17] recommendation and Zelina et al.'s [2] conclusion that this was the loading for peak efficiency. To set the centrifugal loading, Equation 2.2 and 2.3 were utilized. On previous UCC operations, the temperature and

pressure in the UCC section had been measured (see Figure 3.5). From these values and use of the ideal gas law, an estimation of the UCC section flow density was determined. The estimated density was used in Equations 2.2 and 2.3 to solve for the UCC section air mass flow rate needed to achieve a g-loading = 1000 g's. For consistency purposes, the mass flow rate developed by LeBay was maintained in this research.

Further investigations were to vary the distribution of fuel between Injectors 1 and 2 as well as the seeder box fuel injector (see Figure 3.3). As described in Section 3.2.1, LeBay had difficulties in keeping a flame lit when the fuel was distributed 66 % to the seeder box and 33 % to Injectors 1 and 2. LeBay found that the circumferential flame stayed lit in the cavity when only 44 % of the fuel was sent to the seeder box and the remaining fuel was divided evenly between Injector 1 and 2. The test matrix explores the consequences of using LeBay's fuel splits. By turning on and off injectors in the UCC section, any effects the injectors played in the way the UCC and core sections interacted could be observed. When an injector was turned off, it is denoted by a zero as the percent fuel split in Table 4.1.

Table 4.1: Emissions Test Matrix

Test Case	φ	MFR	Fuel Split (%) (Seeder Box / Injector 1 / Injector 2)
E1	1.6	0.2	44 / 28 / 28
E2	1.8	0.2	44 / 28 / 28
E3	2.0	0.2	44 / 28 / 28
E4	2.0	0.1	44 / 28 / 28
E5	2.2	0.2	44 / 28 / 28
E6	2.2	0.1	44 / 28 / 28
E7	2.4	0.2	44 / 28 / 28
E8	2.4	0.1	44 / 28 / 28
E9	2.6	0.2	44 / 28 / 28
E10	2.0	0.2	44 / 28 / 0
E11	2.0	0.2	44 / 0 / 28
E12	2.0	0.2	44 / 56 / 0
E13	2.0	0.2	44 / 0 / 56
E14	2.0	0.2	66 / 16.5 / 0
E15	2.0	0.2	66 / 0 / 16.5

4.1.2 Results of Operating Conditions Testing

The emissions testing facilitated an understanding of the completeness of combustion as well as insights into the structure of the flame at the core section exit plane (see Figure 3.21 for exit plane description). Figure 4.1 collects the results from Case E5, with each line representing a particular pitchwise path in the core section exit plane. Figure 4.1a shows the highest UHC concentration at Point 1 in the exit plane. General trends saw that the UHC concentration decreased with both positive pitchwise and spanwise displacements. Point 9, however, was counter to that trend. Point 9 contained a higher concentration of UHC than Point 5, indicating an absence of combustion at this

location. To further understand where the combustion reactions took place, the O_2 concentrations were interrogated. Figure 4.1b revealed a general decrease in the O_2 concentration with positive spanwise displacement with increasing pitchwise displacement. This indicated a higher concentration of combustion occurred closer to the ID than the OD of the core section. Additionally, more reactions occurred near the vane than in the center of the core section.

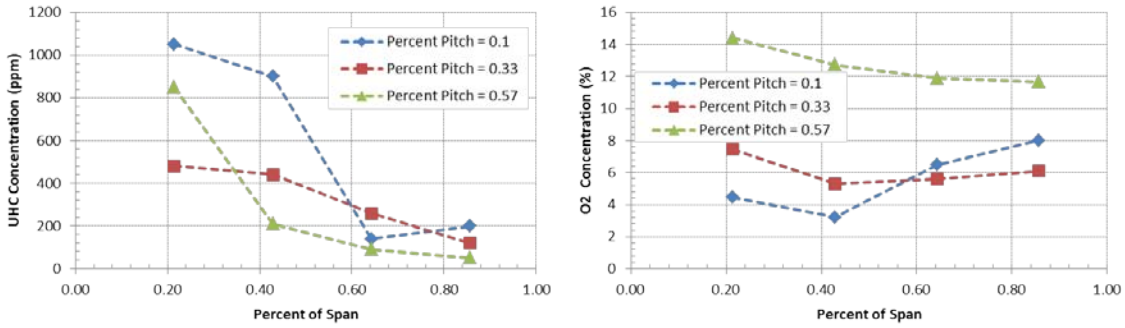

(a) **(b)**

Figure 4.1: Spatial concentration trends for MFR = 0.2, Φ = 2.2, at various spanwise and pitchwise locations for (a) UHCs and (b) O_2

In an effort to better understand the structure of the flame in the core section, HSV from above the core section was collected. Figure 4.2 is a set of four images for Case E3 encompassing 0.0016 s. A distinct helical motion developed in the core section as the flame was ejected from the UCC section. The flame exited the UCC section and progressed diagonally across the channel to the ID wall. Once reaching the wall, the flow turned downward and began the formation of a helical structure. The flame then traversed diagonally back across the channel. This general flow path is indicated on Figure 4.2 by the forward and backward running diagonals.

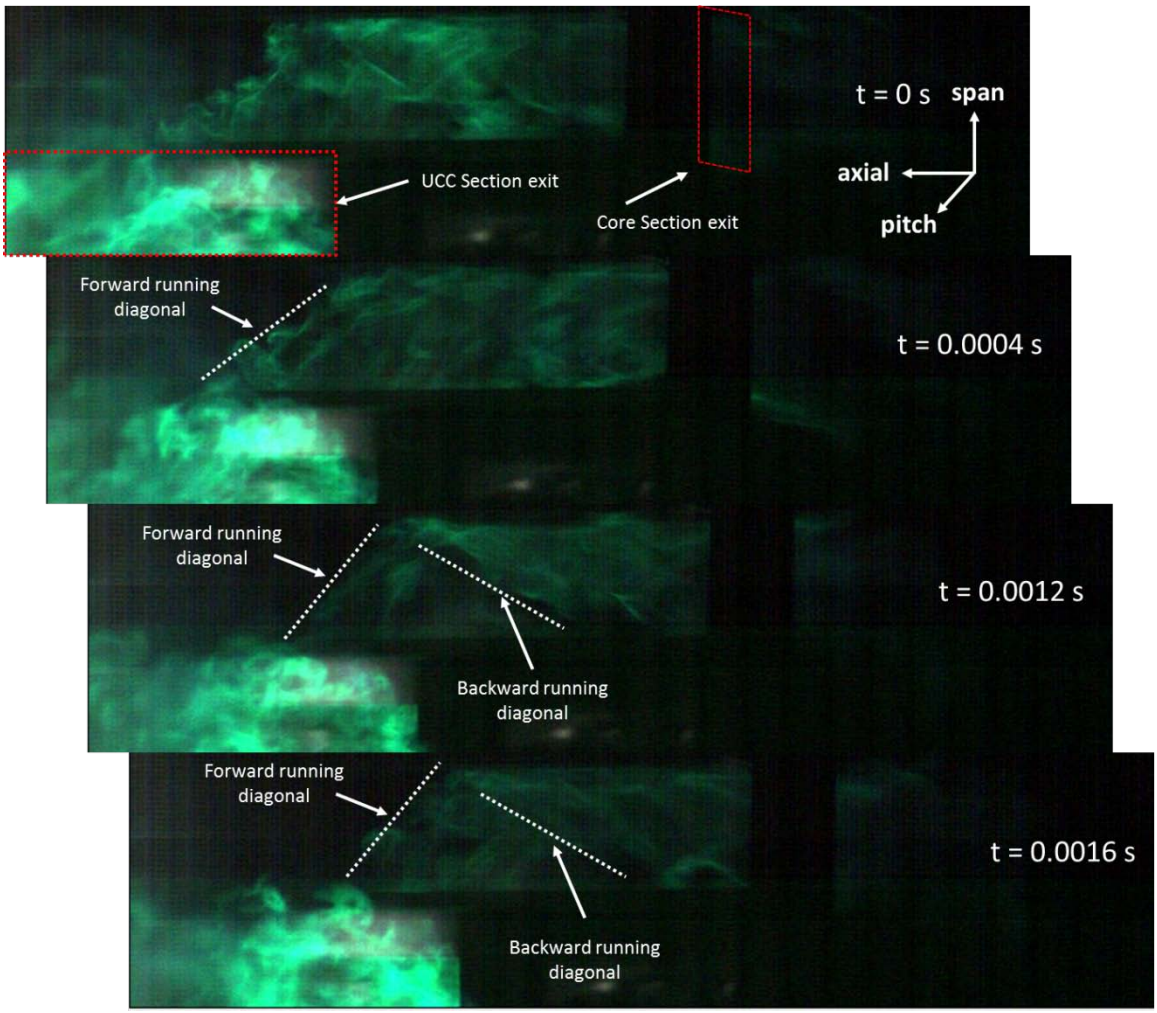

Figure 4.2: HSV frames depicting the helical motion of the flame entering the core section at MFR = 0.2, Φ = 2.0, and Δt = 0.0016 s (top view)

Using the HSV results in Figure 4.2 with the emissions results helped explain the trends being observed in Figure 4.1. At sample Point 1, there was little O_2 due to the fact that the flame is arriving at Point 1 after it had been burning for some time in the helical pattern; therefore, most of the O_2 had been consumed by the exit plane. At Point 9, a high concentration of O_2 was observed. Point 9 is near the point where the center of helix was located. The absence of the flame in the center allowed air to pass through the flame and transport UHCs downstream without being consumed. The vortex demonstrated in

the HSV Figure 4.2 correlated well with the data collected from the emissions measurement and furthered the understanding of the process in the core section.

A key trend to understand was the effect variations in the equivalence ratio had on the emissions concentrations. Figure 4.3 highlights those trends as equivalence ratio was increased. Point 1 consistently yielded the highest concentration of UHC with Point 9 following closely. Point 5 consistently contained the lowest concentration of UHCs, indicating that the flame structure remained fixed. The trend shown in Figure 4.3 indicates that not only does the location of the high UHC concentrations remain unchanged, but that the helical structure in the core section is also independent of equivalence ratio. The only effect equivalence ratio had on the emissions results was to increase the quantity of UHCs present in the core flow.

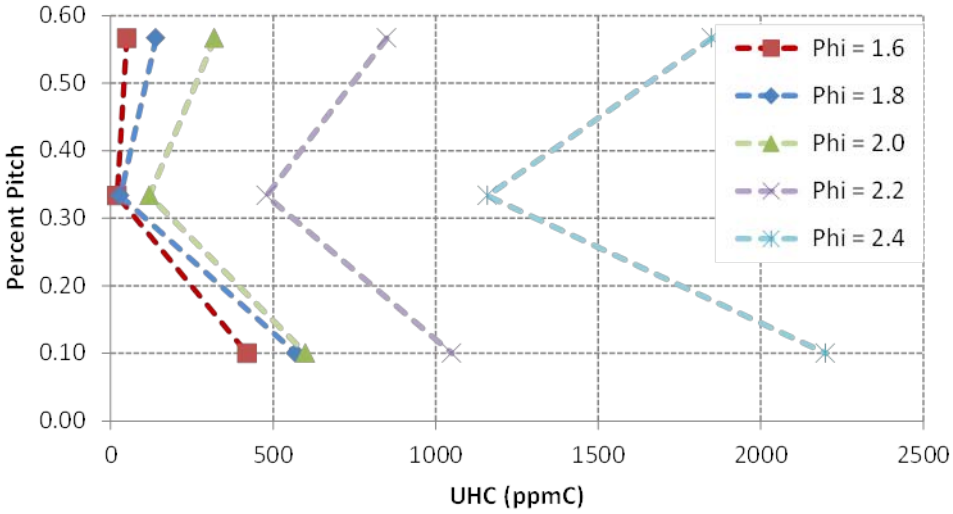

Figure 4.3: UHC concentration as a function of equivalence ratio at 21 % span

With the emissions results correlating well with the HSV results for flame location in the core section, the overall combustor efficiency was evaluated over the range of equivalence ratios outlined in Table 4.1. Figure 4.4 reveals that for low equivalence

ratio, efficiencies near 97 % were measured. Zelina et al. [2] suggested that the UCC bulk emissions should yield a combustor efficiency around 99 % at similar operating conditions. The emissions results show that as equivalence ratio increased, the combustor efficiency decreased significantly faster than the trends reported by Zelina et al. [2]. A drop of roughly 0.5 % in efficiency from $\varphi = 1.5$ to 2.0 was anticipated instead of the 2 % drop observed in the current emissions results.

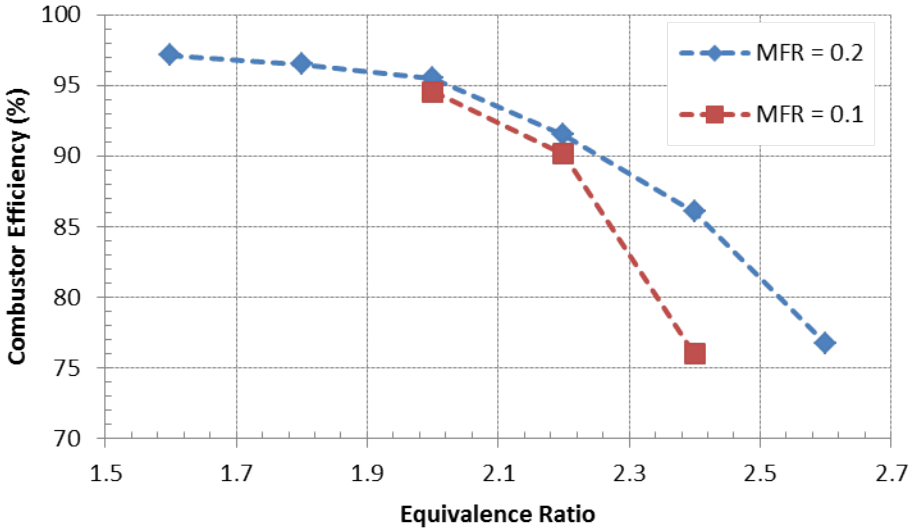

Figure 4.4: Spatially averaged combustor efficiency at various equivalence and mass flow ratios

To investigate the significant drop in combustor efficiency, the source of the high UHC concentration was explored. One area of investigation was how the fuel injectors interacted with the cavity flow and the core flow. Injector 2, at the interface of the UCC and core section is highlighted in Figure 4.5a. The injector port was recessed into a rectangular cavity on the OD of the UCC section (see Figure 3.3)

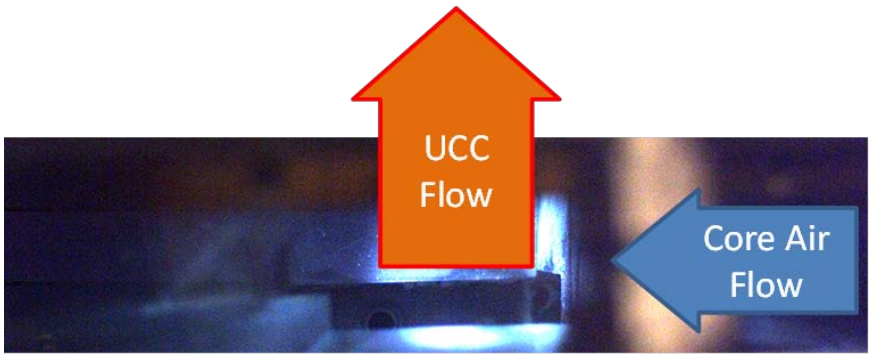

(a)

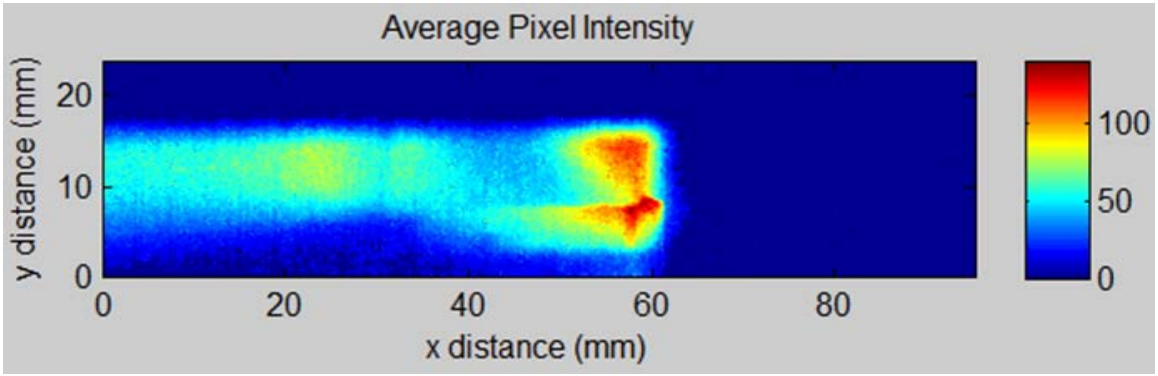

(b)

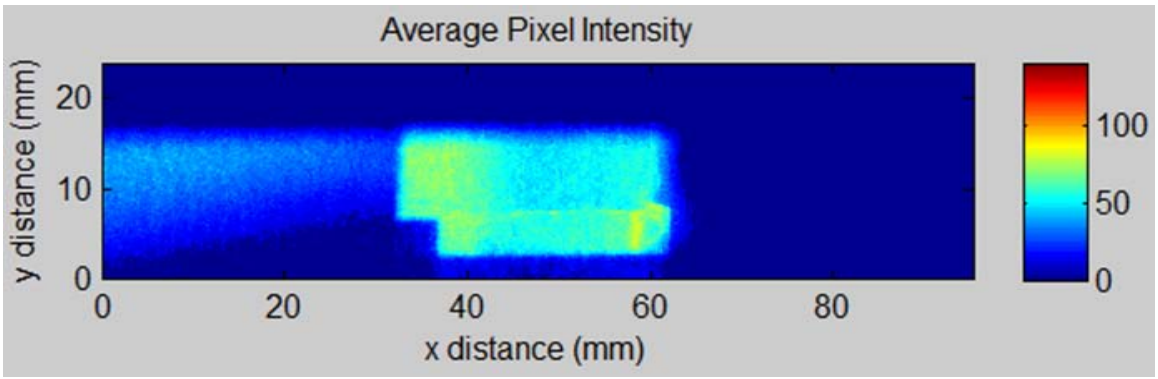

(c)

Figure 4.5: HSV (a) field of view and a visualization of the effects of operating with Injector 2 (b) on and (c) off at MFR = 0.2 and φ = 2.0

As the UCC was originally conceived, each fuel injector should act as a normal jet in a cross flow, being sheared off by the circumferential flow. By calculating the blowing ratio (see Equation 2.15) of the jets, an indication of the penetration of the jet

into the cross flow can be ascertained. From the dimensions of the injector and cross flow as well as the mass flow rate, it was determined that Injector 2 operated at a blowing ratio of 2.53 when the combustor was operating at $\Phi = 2.0$. Using the results from Thole et al. [20] and Polanka et al. [21], the Injector 2 fuel plume was expected to travel about 0.01 m away from the jet in a downstream distance of 0.019 m. Figure 4.6 shows the anticipated path of Injector 2. The trajectory of fuel Injector 2 should not result in fuel directly exiting the circumferential cavity for this case. However, its path will force the upstream constituents into the core section due to its high blowing ratio.

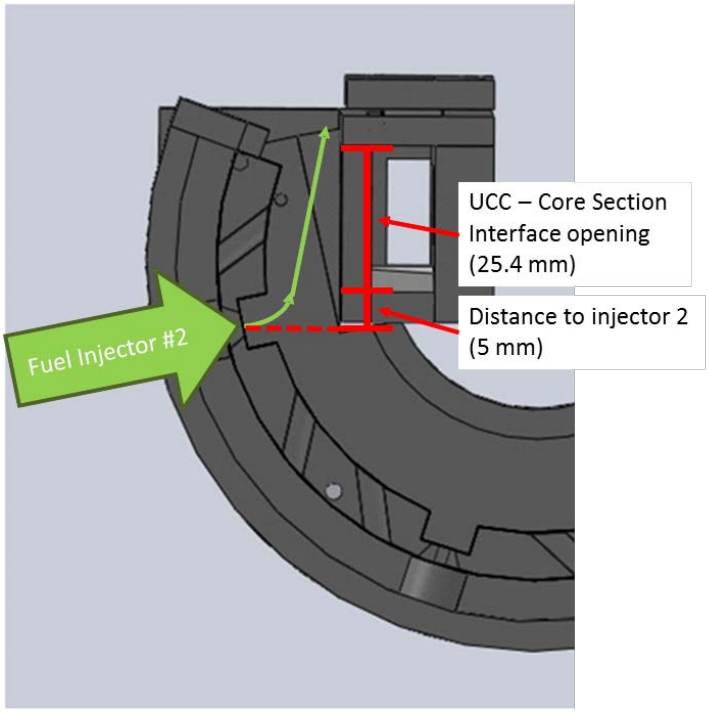

Figure 4.6: Anticipated path of jet core for MFR = 0.2, Φ = 2.0, and M = 2.53

The species observed in the core section was believed to be sourced from the upstream injector since Injector 2's plume did not have the trajectory to enter the core section itself. An estimation of the path of the upstream air supply jets was made using the results from Thole et al.[20], and an estimation of the fuel jet paths was made based

on the results of Polanka et al [21]. Figure 4.7 is a graphical representation of what was believed to occur as air and fuel were added throughout the UCC section. Because of the magnitude of each of the blowing ratios, the fuel was driven to the ID of the UCC section. The air holes provided enough disruption in the cross flow to keep the fuel pinned to the ID of the UCC section. When the upstream constituents, particularly the unburnt fuel from Injector 1 reached the location of Injector 2, the Injector 2 jet pushed the unburnt fuel into the core section. The process described shows the propensity that the beneficial effect of buoyancy was being counteracted by the high blowing ratios utilized to generate the desired equivalence ratio.

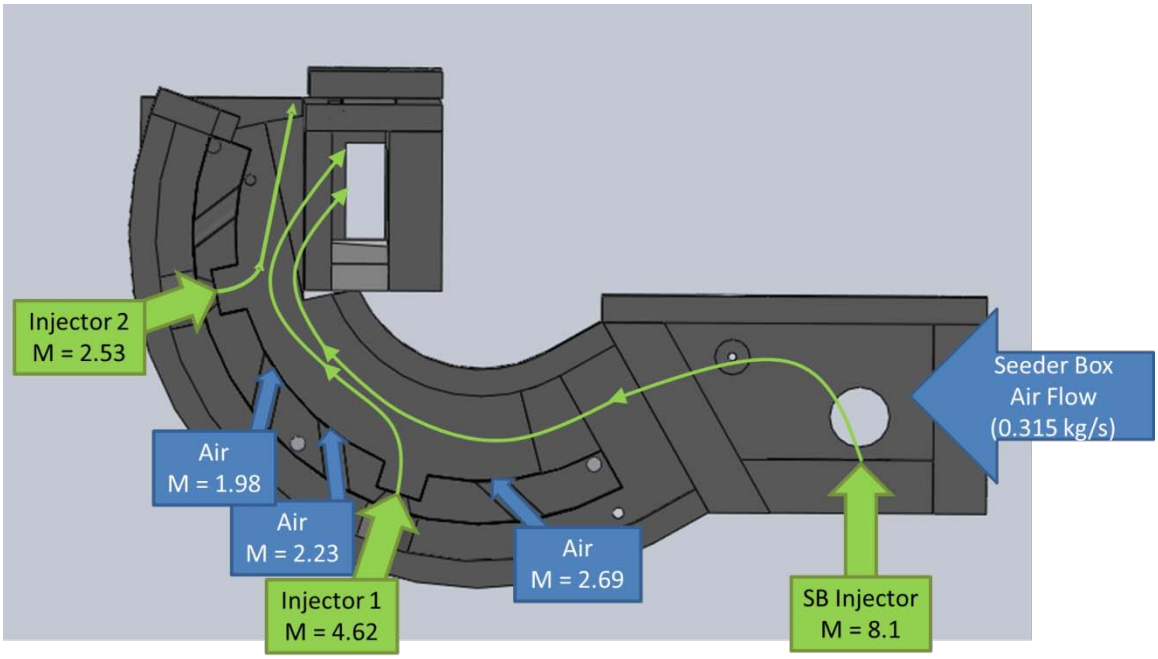

Figure 4.7: Graphical depiction of the fuel flow path in the UCC section

To confirm these calculations, emissions data was recorded for Injectors 1 and 2 turned on and off. This data is compiled in Figure 4.8. With the Injector 2 turned off, fewer UHCs entered into the core section at 21 % span. The concentration of UHC dropped off significantly with positive spanwise movement indicating that the fuel is not

significantly transported across the span. It also indicates that fuel that enters the helix in the core channel was being successfully burned by the time it reached the exit plane. It is noted that a higher concentration of UHC was observed when Injector 2 is off at 43% span that when both injectors are on. This is most likely due to the plume from Injector 1 entering the core section at a higher pitchwise location than when both injectors are on. With Injector 2 on, but Injector 1 off, the amount of UHC's entering into the core section drops by over a factor of 10 across almost the entire airfoil span. The extremely low content of UHCs indicates that the blowing ratio of the second injector, while not large enough to be spraying directly into the core cavity, is large enough to push the constituents of Injector 1 into the core section. The emission results reinforce the conclusions that the blowing ratio of the jets was large enough to overcome the cross flow allowing Injector 2 to pushed UHCs from the upstream injector(s) into the core flow.

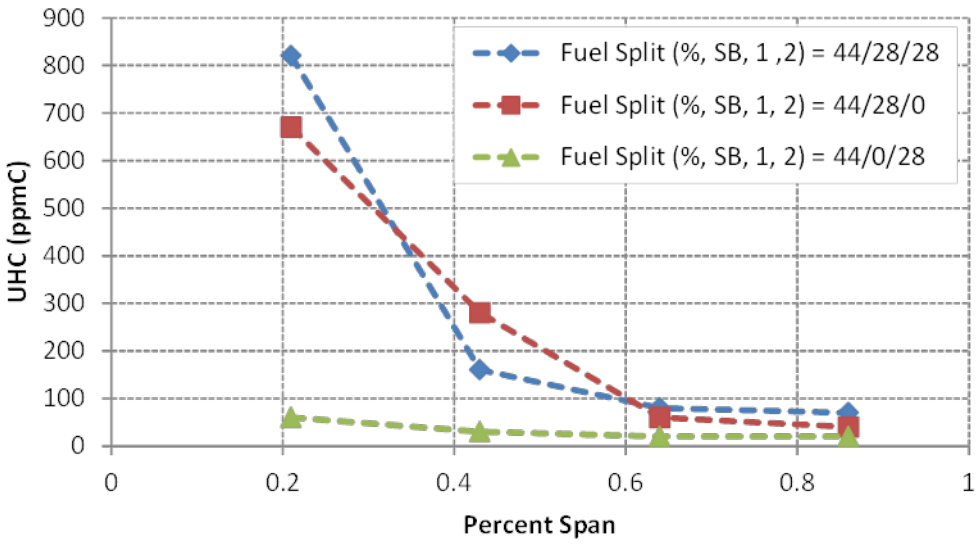

Figure 4.8: UHC concentration along airfoil span at 10 % pitch with variations in fuel delivery locations

4.1.3 Conclusions about the Operating Conditions

Pockets of UHCs were identified as locations where possible secondary reactions could occur; however, the efficiency of the UCC was significantly different from published values. An investigation into the causes of the inefficiencies highlighted the fuel injectors as possible causes. By comparing the blowing ratio of the fuel injectors to film cooling jets, it was observed that fuel rich material could exit the UCC cavity due to the high blowing ratio of the fuel injector jets and the short channel height found within the UCC.

Several design considerations that can mitigate this effect include:

1. Additional fuel jets could be used to reduce the blowing ratio of the individual jets which will reduce the penetration of the plumes enabling them to stay on the OD of the UCC section.
2. The air and fuel could be injected from the side of the UCC rather than radially. This will make the jets travel axially and allow the buoyant forces more opportunity to striate the constituents in the UCC section.
3. A larger channel height could be used to allow the blowing ratio and orientation of fuel and air injection to stay the same, but the plumes would travel a smaller percent of the channel height reducing the opportunity of the jets to push upstream constituents into the core section.

A combination of these ideas may yield the best results; however, care needs to be taken when injecting radially in a UCC structure. Radial injection can have unintended consequences of disrupting the buoyant phenomenon and causing poor combustion

performance. In order for the AFIT UCC section to accurately represent a full annulus, either changes to the test apparatus or operating conditions need to occur.

4.2 Anchoring the Flame

As stated before, the seeder box (see Figure 3.3) was intended to replicate upstream flow conditions by providing a location for four injectors worth of fuel to begin combusting. LeBay [17] observed that the flame in the UCC section would not stay lit if four injectors worth of fuel was brought into the seeder box. He determined the flame would stay ignited when only 44 % of the total fuel flow was sent to the seeder box. Due to this issue, the AFIT UCC section had been operated using LeBay's fuel distribution (as described in Section 3.3).

Following the experiments in the previous section, the seeder box was disassembled for maintenance. Upon reassembly, it was observed that the flame in the UCC and core section had increased in length significantly when run at typical operating conditions. The increase in flame length was evidence that the flame was no longer anchoring in the seeder box but residing somewhere downstream of the seeder box. When this occurred, the residence time of the upstream constituents was significantly reduced and inaccurately represented the upstream conditions. It was observed that slight deviations in the vertical location of the seeder box injector caused the flame to anchor in different parts of the UCC section. This sparked the need to anchor the flame in the seeder box in order to ensure that experiments created the same flame characteristics.

4.2.1 Anchoring the Flame in the Seeder Box

To create a series of experiments that were repeatable, the first step was to find a way to anchor the flame into the seeder box. The initial attempt was to modify the air

inlet so air would be brought into the seeder box from opposing sides (see Figure 4.9). Ideally, the opposing jets would create a stagnation point in the center of the seeder box that would allow the fuel jet to mix with the air and have a stable flame location. The seeder box fuel injection remained on the bottom, while the ignition source moved upstream of the air and fuel inlets. The PIV source was removed completely in order to allow the air to be brought in from opposing sides. The thermocouple was removed in order to use the port as a sight glass to ensure flame was in the seeder box.

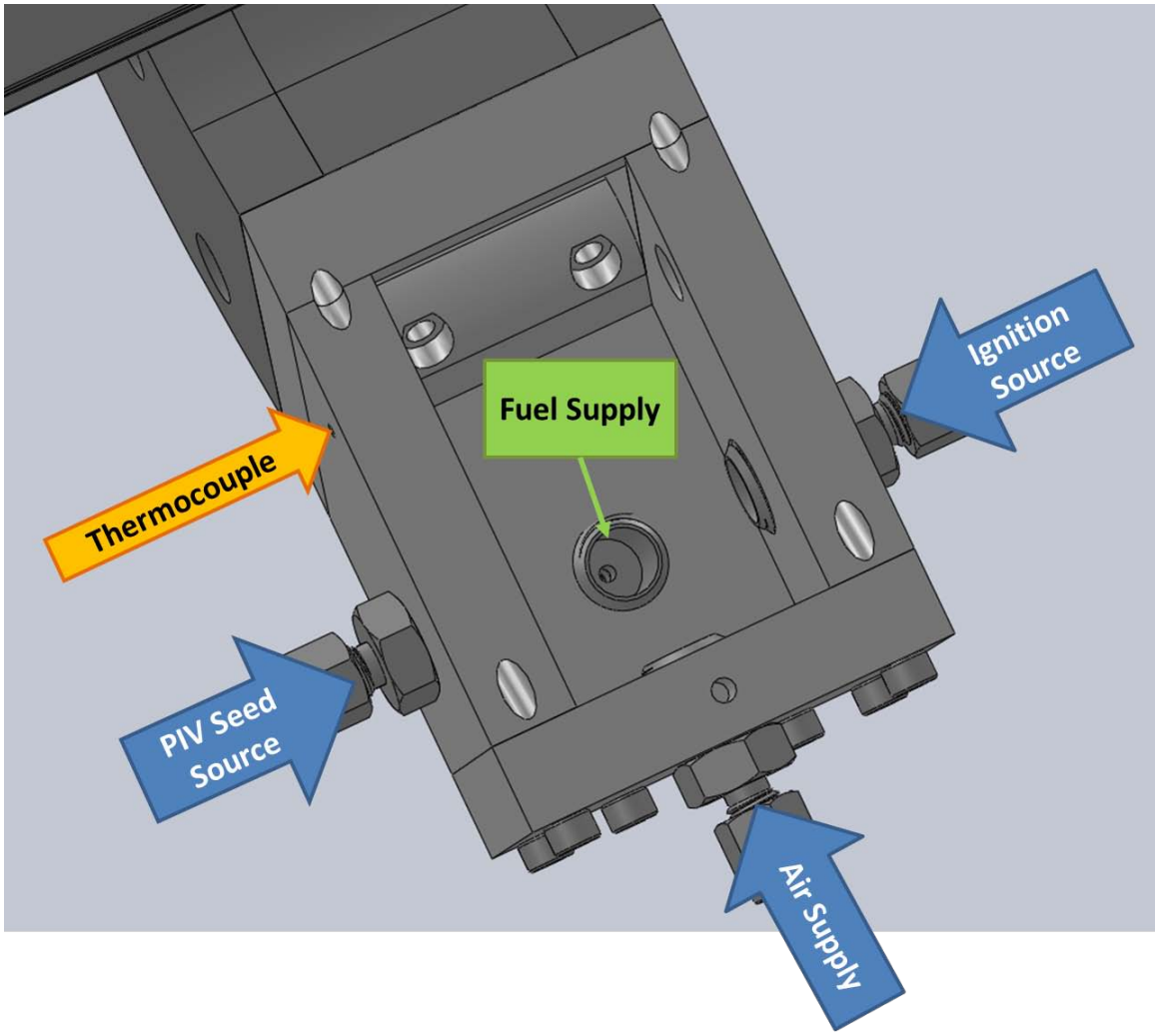

Figure 4.9: Original seeder box setup

The seeder box fuel injector was dropped farther away from the air jets to try and reduce its blowing ratio. Also, the diameter of the injector jet was enlarged from 0.0032 m to 0.0053 m by removing the nozzle on the fuel injector. Together, these things only reduced the blowing ratio to roughly five and still allowed the plume to travel straight through the stagnation point of the air jets. In an effort to further reduce the blowing ratio of the seeder box, a stainless steel u-channel was created. The u-channel was designed to block the core of the fuel plume. This not only split up the fuel injection plume, but it also established a recirculation zone in the seeder box. From previous experience, establishing a recirculation region was crucial to having a consistently anchored flame in the seeder box. The bracket is shown in Figure 4.10 before it was welded into place.

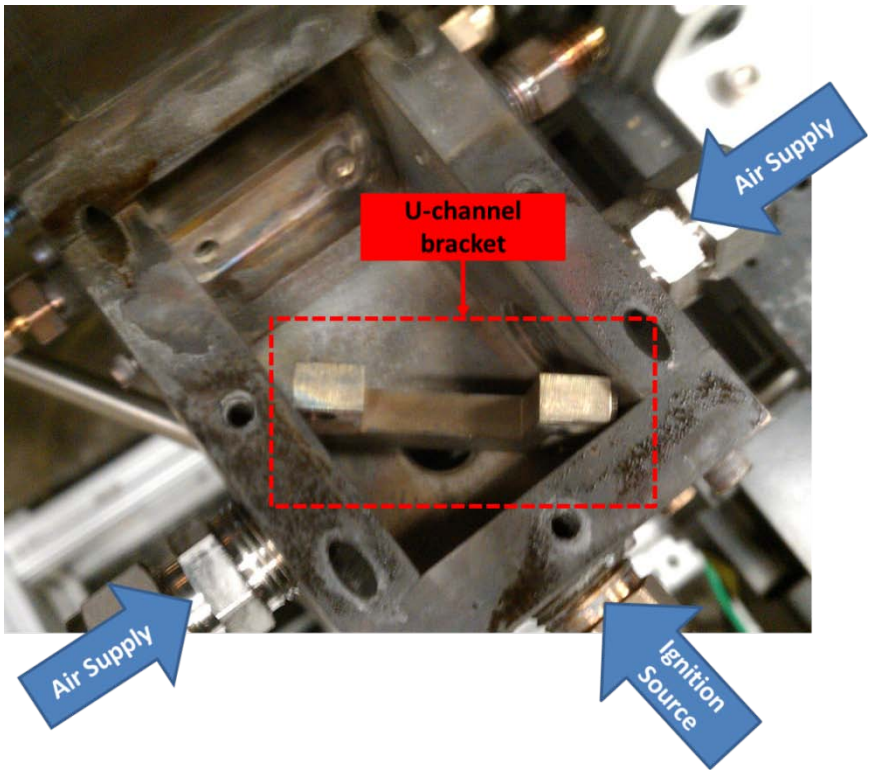

Figure 4.10: U-channel bracket used to develop a recirculation zone to anchor the flame in the seeder box

4.2.2 Results of Anchoring the Flame

After the u-channel was secured in the seeder box, the first objective was to determine if the flame was staying in the seeder box. The thermocouple that had previously been located in the seeder box (see Figure 4.9) was removed. This exposed an optical port with a diameter of 0.0016 m to confirm the presence of a flame in the seeder box. A blue flame could be observed in the seeder box with the u-channel present, and no blue flame in the seeder box when the UCC was operated without the u-channel. This confirmed that the u-channel was holding the flame in the seeder box.

Understanding that the sectional UCC needs to replicate the physics of a full annulus, an investigation occurred to determine where the flame anchored in the test apparatus. LeBay [17] split the fuel flow so that each injector had 28 % of the fuel flow instead of 16.5 % like the split would be for a full annulus. The seeder box only had 44% of the fuel, so instead of the seeder box replicating 4 upstream fuel injectors, it was only replicating 2.5. Therefore, the first test of the new u-channel flame anchor was to determine if a flame would remain in the seeder box if the appropriate 66% of fuel was delivered to the box. In preliminary tests, the UCC successfully started ten out of ten times at the 66% fuel split. For each start, the flame was visible in the thermocouple port, and for varying lengths of time the flame remained in the seeder box. A time dependence on whether the flame was anchored or not was never observed. The success of these ten starts provided the confidence that the UCC could now be successfully operated with the seeder box replicating four upstream fuel injectors.

A qualitative comparison was made between the fuel split LeBay used without an anchored flame, the fuel split LeBay used with an anchored flame, and the preferred fuel

split of 66 % in the seeder box and 16.5 % to each downstream injector as shown in Figure 4.11. The geometric scaling is slightly different between the images, but the set of images serve as a good qualitative basis to observe the major changes in the flame intensity and shape the core section flow. Immediately, one notices the change in average flame shape in the core section amongst all three of the cases. In Figure 4.11a, the flame is located at the top and at the bottom of the core section, with very little flame in the middle of the section. When the flame is anchored in the seeder box, however, Figure 4.11b and 4.11c show the flame envelops almost the entire pitch of the core section. Figure 4.11b also highlights that the flame is nearly extinguished by the exit of the core section unlike in either Figure 4.11a or 4.11c. For Figure 4.11b, with only 44 % of the fuel in the seeder box, the residence time is sufficient for all of the constituents to react before the exit plane.

LeBay [17] also observed a distinct 130 Hz frequency present in the core section flame. The frequency intensity is normalized, as seen in Figure 4.12a, and clearly shows that a single frequency of 130 Hz was significantly more prominent than any other frequency. After the flame was anchored into the seeder box and the appropriate fuel split was applied, the most prominent frequencies were distributed amongst the lower frequency spectrum, as seen in Figure 4.12b. Figure 4.12b is normalized by the intensity of the 130 Hz frequency from LeBay's results. Because of the magnitude of the frequency observed by LeBay versus the other frequencies, it had been speculated that the frequency was being forced within the UCC section. It is possible that there was an interaction occurring between the cross flow and the fuel injector jet that caused vortex shedding to occur at the particular frequency. It may also have resulted from a vortex

shedding occurring due to the geometry of the seeder box. With the flame anchored in the seeder box through the use of the u-channel, the resonance was no longer observed.

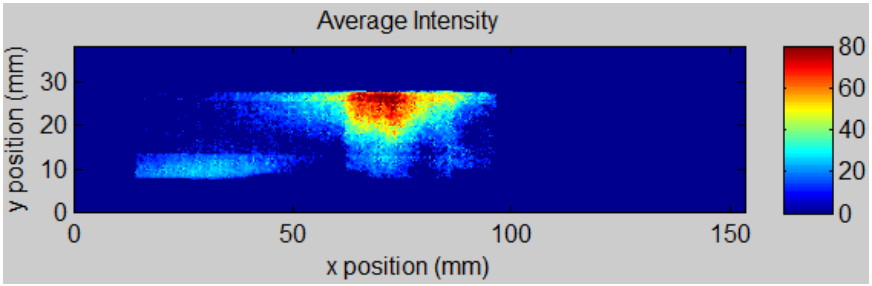

(a)

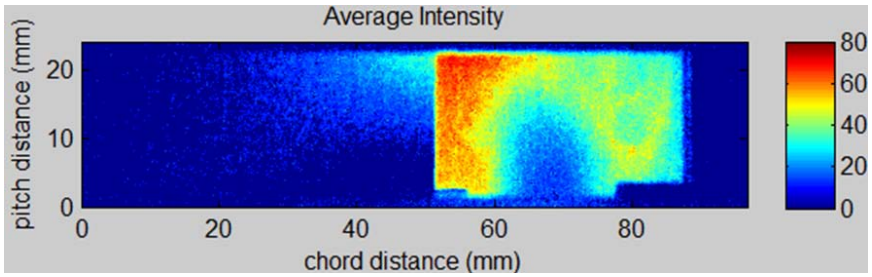

(b)

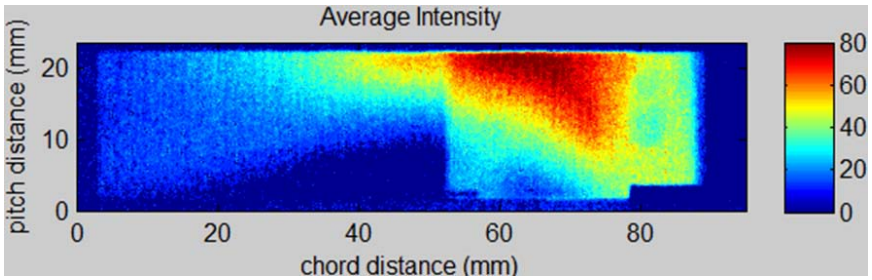

(c)

Figure 4.11: Changes in core section intensity and flame shape at (a) 44 % fuel split without an anchored flame (b) 44 % fuel split with an anchored flame and (c) 66 % fuel split with an anchored flame at 1000 g's, MFR = 0.2, Φ = 2.2 (side view)

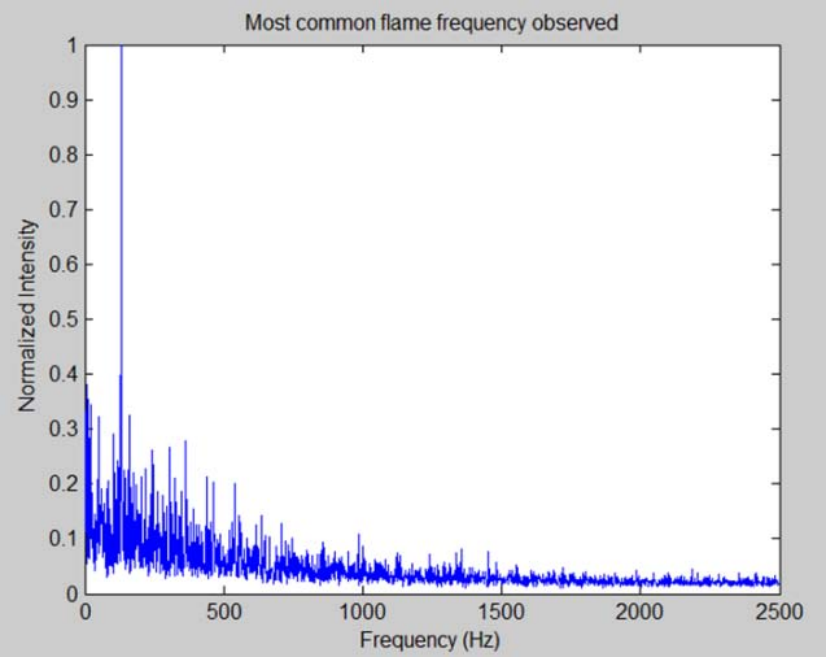

(a)

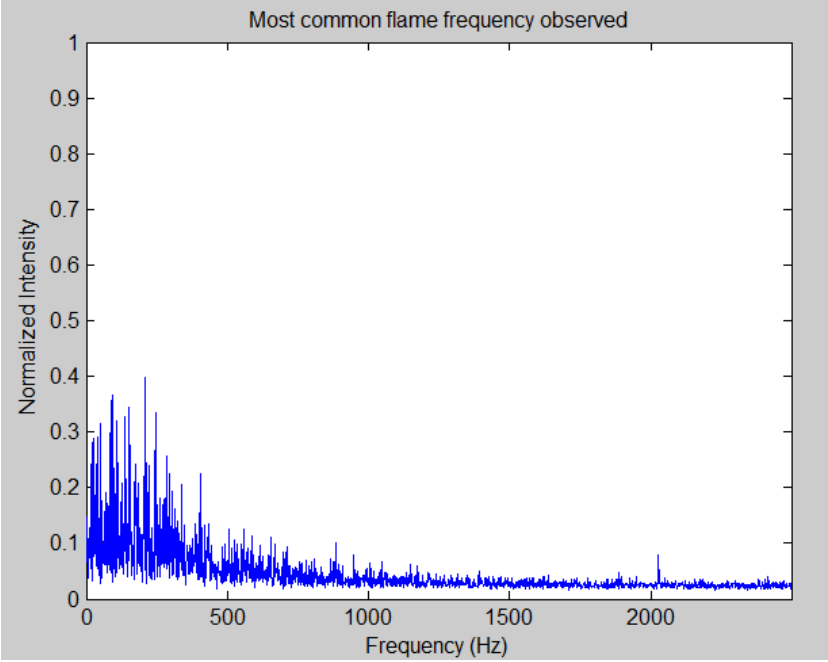

(b)

Figure 4.12: Differences in frequency spectrum from (a) 44 % fuel split without an anchored flame and (b) 66 % fuel split with an anchored flame at 1000 g's, MFR = 0.2, Φ = 2.2

From the HSV and frequency results, it was easy to observe major differences in the flame structure. It was anticipated that similar differences would be observed in the emissions spectrum as well after both anchoring the flame into the seeder box and applying the preferred fuel split of 66 % to the seeder box. As an additional benefit, using the preferred fuel split significantly reduced the blowing ratio of the fuel injectors in the UCC section. Each injector's blowing ratio was reduced by nearly a factor of two, which is enough to alleviate the excess UHC emissions observed in Section 4.1. Anchoring the flame proved to be a significant accomplishment that solved several issues associated with the UCC section not being operated as intended.

4.2.3 Repeatability of Experiments

Repeatability is a fundamental requirement to ensure the integrity of data. To show repeatability of the current study, the baseline case was repeated five times. Two data sets were recorded consecutively, two were taken at random intervals, and one was taken after the test section was disassembled and reassembled. The results of this repeatability analysis can be found in Figure 4.13. Little distinguishable differences appear between the five data sets shown in Figure 4.13a. An average of the data was taken to give an approximate shape of the flame as seen in Figure 4.13b. It is difficult to identify any differences between the individual sets of the data and the average. This indicates that a time record of 0.8 s accurately captures the shape and pixel intensity of the flame.

A standard deviation of the five sets of averaged data was taken. As shown in Figure 4.13c, standard deviation in the core section was roughly an intensity of four along the outer edges of the flame, and an intensity of two to three within the flame. Even within the confines of the UCC section, the standard deviation is only a pixel intensity of

four. This indicates that for everywhere away from the edge of the flame, the difference in pixel intensity is less than +/- 10 % of the mean value (using 2 standard deviations). This is a strong indication that the experiments are now very consistent and repeatable.

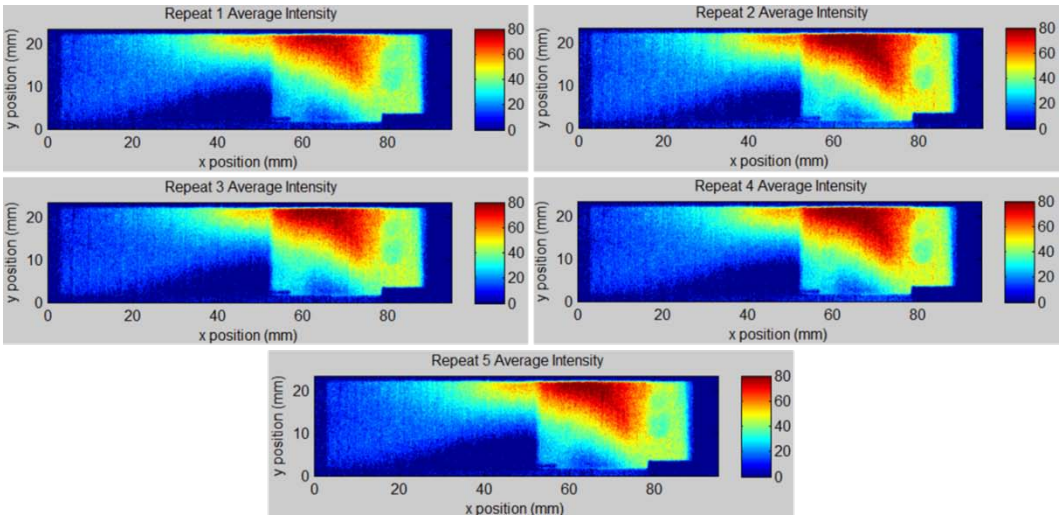

(a)

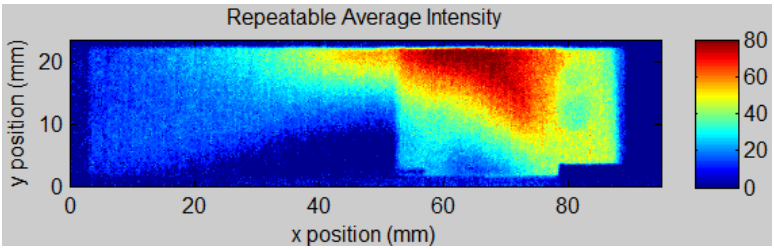

(b)

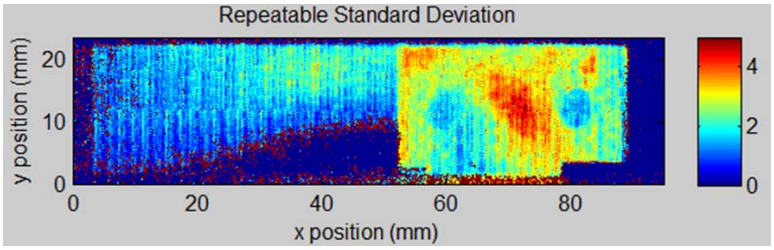

(c)

Figure 4.13: Repeatability analysis showing (a) the five independent sets of data (b) the average and (c) the standard deviation for the sets of data with core air flowing from right to left (side view)

V. Results and Discussion

The results of the HSV and emissions experiments outlined in Chapter 3 are presented in this chapter. It is important to understand that the following results are products of the flame being anchored in the seeder box. These results will accomplish the objectives of first, establishing the flame and emissions characteristics with the vane on the bottom of the core section. The results will then meet the objective of describing the differences in flame and emissions characteristics when the vane is located on the top of the core section. Finally, the results will meet the objective of showing a desensitization of the flame and emissions characteristics when the tiger claw vane was used. A discussion on the main observations will follow the presentation of results.

5.1 HSV Results

The following sections present the HSV results. The first section will explore the physical flame characteristics (i.e. shape, intensity, and location) for the solid vane and RVC. This will occur for the vane located on the bottom and the top of the core section. The following section will show the shape of the flame due to the tiger claw as well as trends in the shape due to placing the vane on the upper side of the core section. These results will show the desensitization in the physical flame characteristics that has occurred as a result of implementing the tiger claw.

5.1.1 Verification of Previous Trends and Initial Results

The first HSV experiments conducted used the solid vane and RVC when the vane was located on the bottom of the core section. These experiments were designed to show the effects of either reducing the blowing ratio of the fuel injectors in the UCC section or turning an injector off completely. As discussed at the end of Section 4.2.2, anchoring

the flame in the seeder box had the unforeseen benefit of reducing the blowing ratio naturally in the UCC section. Therefore, very little distinguishable differences were observed from either the pitchwise plane or the spanwise plane. Figure 5.1 is a compilation of Cases 16, 17, 18, and 19 from Table 3.3 which yielded representative results for each of the other cases with similar fuel distributions. These cases are of similar nature to those conducted in Section 4.1. However, these results (and the remainder of the results in Chapter 5) occurred with the flame anchored in the seeder box where the results in Chapter 4 did not have the flame anchored in the seeder box.

There is a consistent decrease of the flame intensity in the core section, both from the side and above, in Figure 5.1b, 5.1c, and Figure 5.1d over that in Figure 5.1a. This is consistent with the lower amount of fuel being delivered to the UCC section due to one of the injectors being turned off or the blowing ratio being decreased. The shape of the flame, however, remains consistent regardless of the fuel split or blowing ratio in the UCC section. These results, consistent across each airfoil, confirmed that sending 66 % of the fuel to the seeder box dropped the blowing ratio of the injectors in the UCC section sufficiently to prevent an effect on the core section constituents.

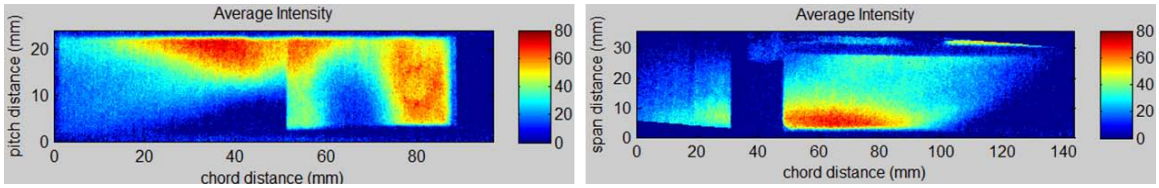

(a)

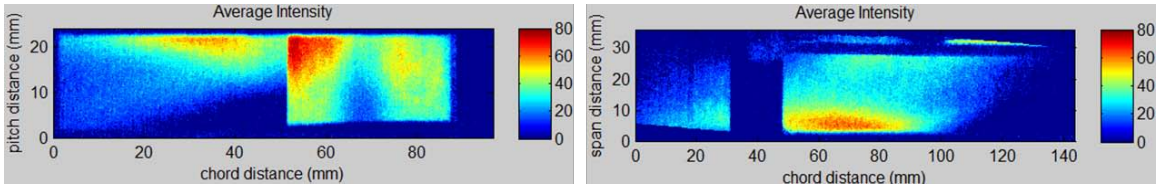

(b)

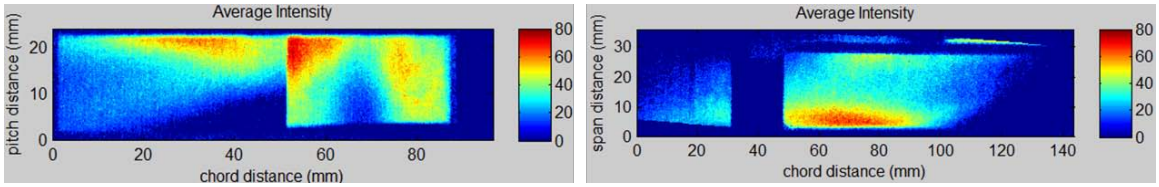

(c)

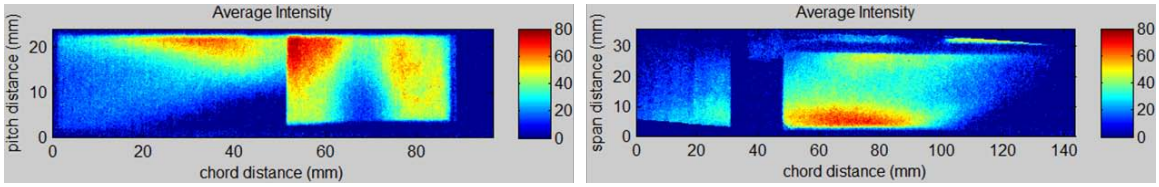

(d)

Figure 5.1: Side view (left) and top view (right) HSV results for (a) 66 % of fuel in the seeder box and both injectors on (b) Injector 1 off, (c) Injector 2 off, and (d) UCC section injectors at half their blowing ratios, MFR = 0.2, Φ = 2.2

Three other experiments were carried out to ensure the seeder box constituents (the hot products) were exiting into the core section. Cases 27, 28, and 29 reduced the amount of fuel into the seeder box. If the flame structure significantly changed or the pixel intensity did not decrease, concern would arise that colder constituents (not seeder box flow) were entering the core section. A decrease in pixel intensity would solidify the

observations that only the hot products were entering the core section. Figure 5.2 compares the three cases. It is easily seen that the intensity gradually decreases with the decrease in fuel flow to the seeder box confirming that the colder, unburnt reactants were not entering the core section.

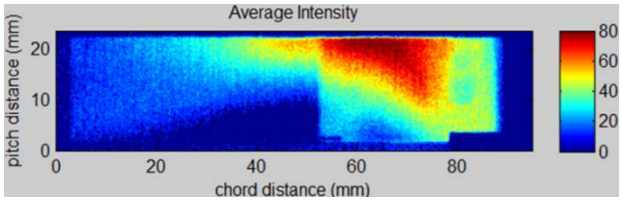

(a)

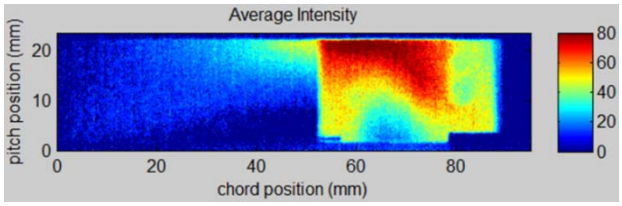

(b)

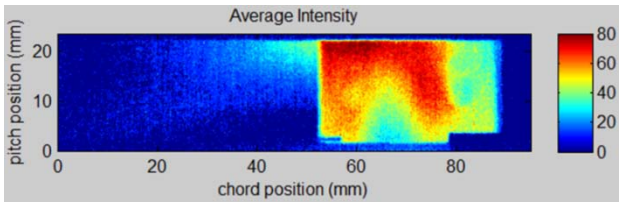

(c)

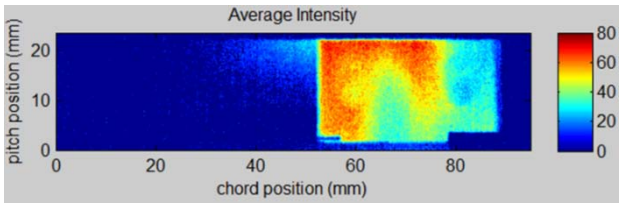

(d)

Figure 5.2: Intensity reduction in the core section for (a) baseline (Case 21) to (b) 11 % (Case 27), (c) 19 % (Case 28), and (d) 26 % (Case 29) decrease in fuel flow to the seeder box (side view)

In order to be able to determine the changes in flame structure due to placing the vane on the top of the core section, it is important to first understand how the flame behaves with the vane on the bottom of the section. Figure 5.3 compares the solid vane to the RVC from both a side and top perspective. Looking at Figure 5.3a from the side perspective, the flame exits the UCC section with the lower edge of the flame making a gradual transition from about mid-pitch to the surface of the airfoil by the exit of the core section. The RVC exhibits the same trend as observed in Figure 5.3b.

From the top perspective in Figure 5.3a, a large concentration of high intensity pixels is located on the core section ID for the solid airfoil. This aligns with the large concentration of high intensity pixels at the top of the pitch from the side perspective. This concentration is indicative of the flame coming out of the UCC section and slamming into the core section ID. The RVC does not exhibit the same behavior at the same operating conditions. From the top view, the RVC increases mixing at the UCC and core section interface, indicated by the high intensity concentration extending from the UCC section above the RVC. The largest average high pixel intensity occurs above the RVC instead of on the core section ID. However, there is still a collection of significant pixel intensity on the core section ID.

For the solid airfoil, little mixing between the core flow and UCC exit flow occurs until the UCC exit flow impinges upon the core section ID. This mixing was indicated by the helical structure presented in Chapter 4. It appears that for the RVC, the intensity extension into the core section is likely due to the mixing occurring at the UCC and core section interface instead of when the flow impinges on the ID. The increase in mixing

and gradual progression from the core section OD to ID is a benefit that the tiger claw aims to maintain.

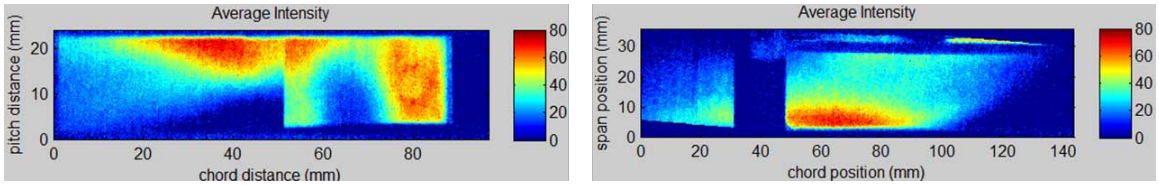

(a)

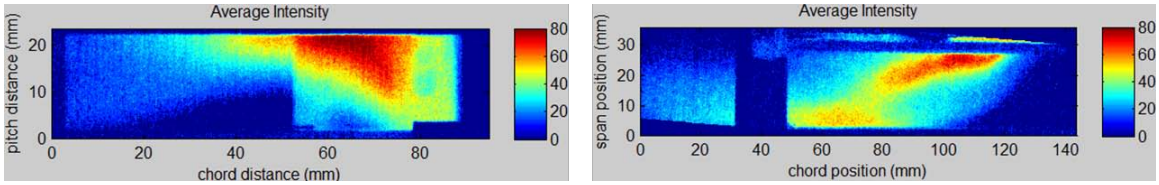

(b)

Figure 5.3: Side view (left) and top view (right) changes in flame shape and intensity for vanes facing away from the circumferential flow for (a) Case 16 and (b) Case 21

LeBay [17] observed that changes to the MFR significantly changed the way the flame exited into the core section. Figure 5.4 highlights the effect of changing MFR for the RVC airfoil. For an MFR = 0.3, a drop in intensity of the flame structure above the RVC can be seen in the top view of Figure 5.4c. However, an increase in intensity occurs along the core section ID similar to that of the solid airfoil. The increase in intensity is indicative of the flame impinging on the ID wall of the core section. It is also noted that from the side view, the average flame shape covers nearly the entire pitch of the core section at the trailing edge of the UCC-core section interface. This is indicating that at the higher MFR, with less upstream air mass in the core section, the flame is able to enter the core section at an earlier pitch.

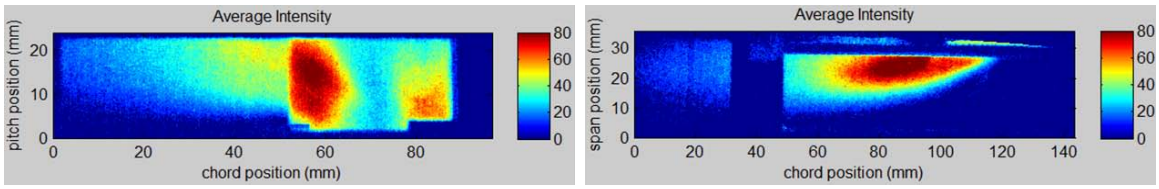

(a)

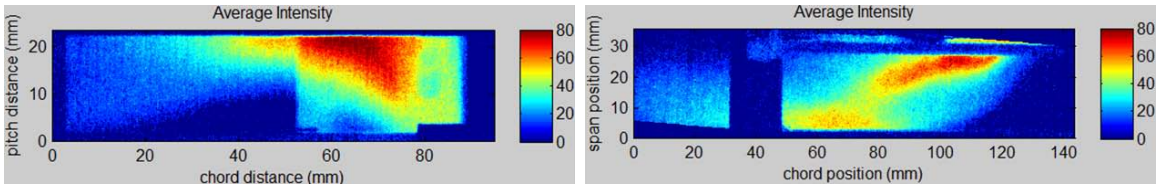

(b)

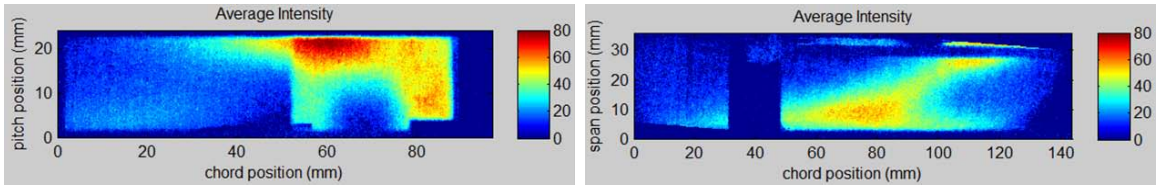

(c)

Figure 5.4: Side view (left) and top view (right) showing the effect on the flame shape and intensity due to changing MFR for (a) MFR = 0.1 , (b) MFR = 0.2, and (c) MFR = 0.3

When the MFR = 0.1, it is noticed that both shape and intensity of the flame in the core section are drastically different. From the side perspective, the average flame shape covers almost the entire pitch of the core section, but from the top view it is seen that the flame only enters traverses about half of the span of the airfoil. This keeps all the hot products on the OD of the core section. The changing of flame shape, and consequently the temperature profile, makes it difficult to develop a turbine blade cooling scheme. In order to account for changing temperature profiles either the cooling scheme itself would have to vary or the scheme would have to cover all possible temperature profiles which would negatively affect the structural integrity of the turbine component. Figure 5.4

shows the same trends observed by LeBay and highlights the magnitude of the problem the tiger claw vane attempts to address.

A secondary goal of the work was to address the changes in flame shape and intensity due to placing the vane on the top of the core section. Figure 5.5 highlights the differences between the different locations for the vane (refer to Figure 3.18 for camera orientation). It is seen from the side view that the average flame shape starts lower in the core section for both the solid vane and the RVC than when the vane was located on the bottom.

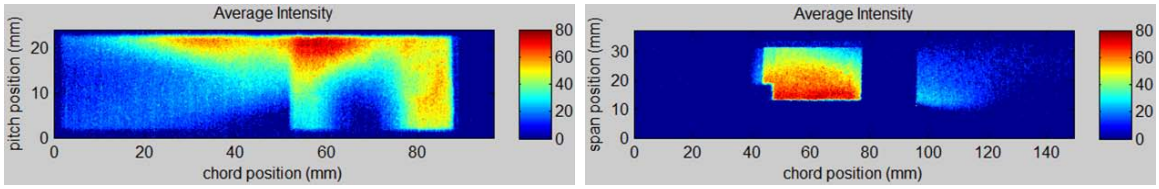

(a)

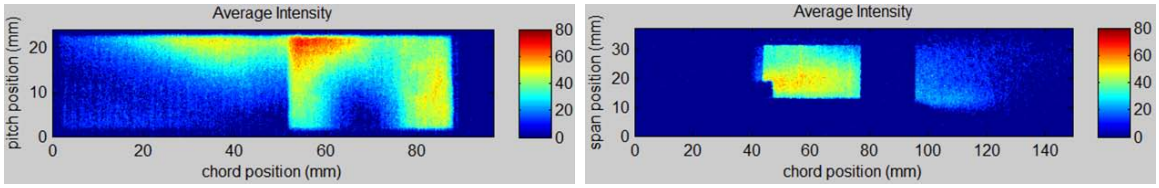

(b)

Figure 5.5: Side view (left) and bottom view (right) changes in flame shape and intensity for the vane on the top of the core section with (a) solid vane and (b) RVC

A significant change in the intensity of flame in the core section is also observed. The solid vane again has the more intense profile, and looking from the bottom view, it can be seen that the solid airfoil again produces higher intensity on the core section ID than the RVC does. Both vanes on the top of the core section exhibit a more uniform pixel intensity distribution across the span of the vane than when the vanes were located on the bottom of the core section.

Continuing to look at the effects of placing the vane on the top of the core section, Figure 5.6 explores the changes in flame shape and intensity of variations in MFR. Looking at the core section from the side, Figure 5.6a shows that the average flame encompasses the entire core section with concentrations at the top and bottom of the core section. From below, it is apparent that the majority of the intensity is on the core section ID, consistent with the results when the RVC was on the bottom of the core section

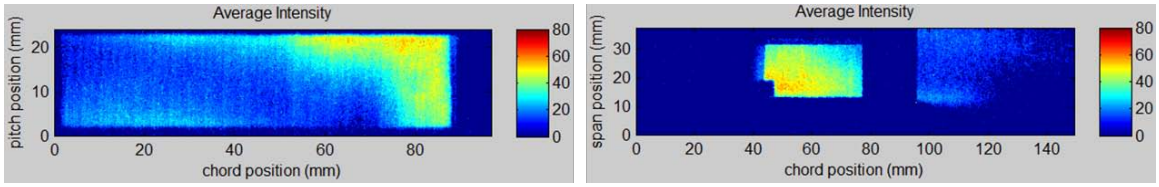

(a)

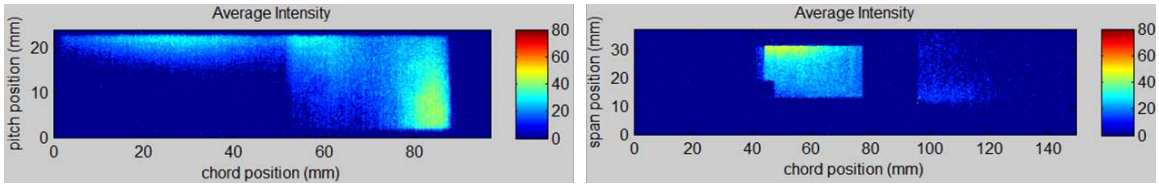

(b)

Figure 5.6: Side view (left) and bottom view (right) showing the effect of changes in MFR to the RVC on the top of the core section for (a) MFR = 0.3 and (b) MFR = 0.1

Examining Figure 5.6b, the side view shows almost no visible flame in the core section. Not only is this very different from a MFR = 0.2, but it is also different from when the RVC was located on the bottom of the core section. Looking at Figure 5.6b with the vane viewed from below, we notice a relatively uniform distribution with a slight concentration in intensity near the OD as expected from the previous results. Using the information present in both views from Figure 5.6b, since there is no flame in the core section below the 15 mm point, the flame is spread somewhat evenly across the upper surface. This indicates that the flame is being channeled and entering into the core

section via the RVC. However, there is still enough momentum in the core section air to ensure that the flame does not completely distribute itself across the span of the vane.

5.1.2 Tiger Claw Effect on Flame Shape and Intensity

The previously section clearly depicted the variations that occur when MFR is changed. The tiger claw was implemented as an attempt to desensitize the shape and intensity of the flame to changes in operating parameters. Figure 5.7 highlights the results of implementing the tiger claw. In Figure 5.7b, the flame shape from the side perspective is very similar to that of the solid and RVC vanes (see Figure 5.5). The highest level of intensity is seen at the top of the core section as well. Looking at the tiger claw from below, the intensity is very evenly distributed across the span of the vane, with a slight drop in intensity near the OD of the core section. This is an obvious change from the RVC and solid vane's results. In each of the previous vane cases, there was a significant gradient in intensity between the ID and the OD of the core section. The tiger claw does an obvious job of distributing the burning in the core section to cover the entire span of the vane.

Figures 5.7a and 5.7c show the effects the tiger claw has when MFR is altered. When MFR is increased, we see a definitive change in shape from the side perspective similar to that of the RVC. However, the tiger claw retains more intensity concentration at the top of the core section without shifting a significant amount to the bottom. When the MFR is dropped to 0.1, again a significant change in shape occurs. While it appears the flame enters the core section near mid-pitch, the intensity hangs to the upper surface. While the flame is not completely desensitized to changes in MFR, it does appear to have

less of an effect on the flame shape when viewed from the side than when the solid or RVC vanes were in place.

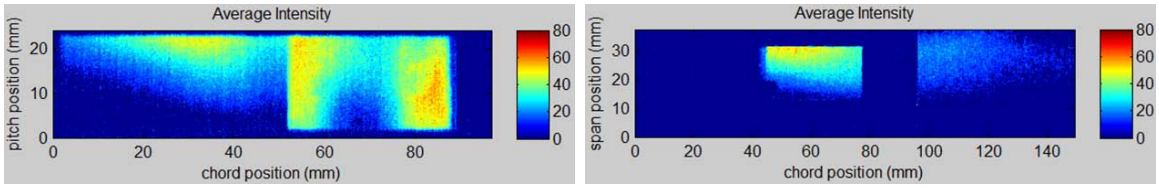

(a)

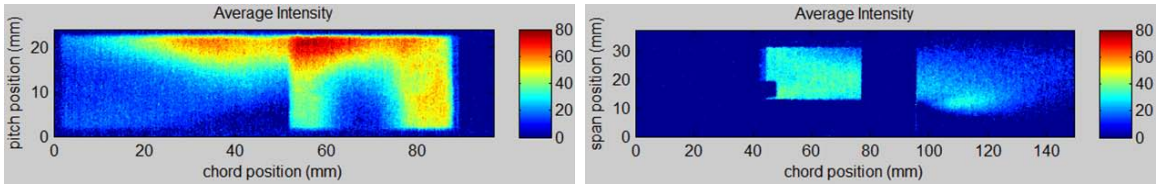

(b)

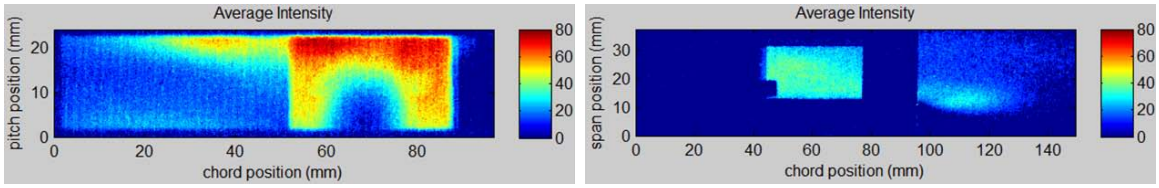

(c)

Figure 5.7: Side view (left) and bottom view (right) showing flame location and intensity for tiger claw vane for (a) MFR = 0.1, (b) MFR = 0.2, and (c) MFR = 0.3

When observing the flame from below, the tiger claw retains nearly the same distribution of flame across the span of the vane in Figure 5.7b to that in Figure 5.7c. It appears that the increase in MFR did very little to change the distribution of flame, where with the other vanes, the flame would immediately become concentrated on the ID. It is noted, though, in Figure 5.7a the flame is still concentrated on the OD of the core section. The tiger claw does spread the flame to cover almost the enter span of the vane, which has not occurred with any of the other vanes at an MFR = 0.1. There is still a significant intensity gradient across the span, but much less than what was observed in Figure 5.4a.

The change in centrifugal loading was also explored to see if the tiger claw was capable of desensitizing the flame in the core section. The intention was to explore both a 500 g and a 2000 g scenario (Cases 14 and 15 in Table 3.3); however, it was observed that the flame would not stay anchored in the seeder box for the 2000 g case. The results from the 2000 g case were deemed unreliable and are not presented. The 500 g scenario is shown in Figure 5.8. It appears very similar to the MFR = 0.1 (g-loading = 1000 g) case shown in Figure 5.7c. It is noted that when viewed from below, the distribution across the vane span is fairly even, unlike the MFR = 0.1 case.

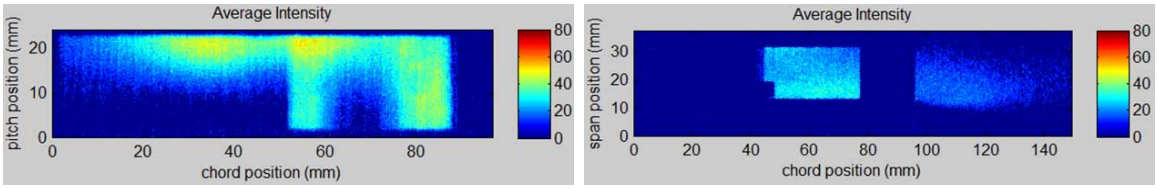

Figure 5.8: Side view (left) and bottom view (right) showing the tiger claw's effect of the core section flame at MFR = 0.2, g-loading = 500 g

5.2 Emissions Results

As reported earlier, the first set of emissions data showed that the UCC section was operating inefficiently at an MFR = 0.2, g-loading = 1000 g, and $\Phi = 2.2$. When the flame was anchored in the seeder box, only HSV of the results was taken; therefore, the first few emissions tests were taken with the vane on the bottom of the core section to document the results of anchoring the flame and to highlight differences between the vane on the bottom and top. The following sections will address the emission results of anchoring the flame and the differences between the vane on top versus bottom as well as the effect the tiger claw has on emissions.

5.2.1 Emissions Results Based on Placement of Vane

Anchoring the flame in the seeder box had significant impact on the emissions results improving those reported in Section 4.1.2. Figure 5.9 highlights the significant reduction in UHC (ppmC) over that shown in Figure 4.1a. The most obvious difference is over an order of magnitude reduction in peak UHC emissions. Similar trends did occur, however, as UHC concentration decreased with movement from the OD to the ID of the core section. The peak concentration point moved from being at the 10 % pitch location to the 80 % pitch location. The concentration then decreased with a decrease in pitch location. An interesting observation for both the RVC and solid vanes was that there were no UHC emissions for the 10 % and 33 % pitch locations at all. If the reader recalls from Figure 4.1, the 10 % pitch yielded the highest concentration of UHC when the flame was not anchored in the seeder box. Therefore, anchoring the flame in the seeder box had a significant effect on both the magnitude and location of the maximum UHC emissions.

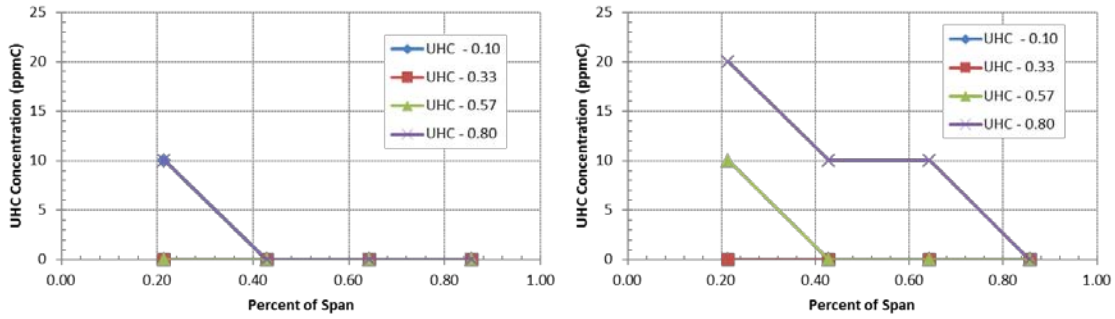

(a) **(b)**

Figure 5.9: Reduction in UHC concentration for (a) RVC and (b) solid vane on the bottom of core section, MFR = 0.2, g-loading = 1000 g, and Φ = 2.2

Investigating the RVC results further, it was observed that the EI CO decreased from the OD to the ID as seen in Figure 5.10. This correlates with an increase in production of CO_2, as seen in Figure 5.10b with a general increase in EI CO_2 with spanwise movement from the OD to the ID of the core section. This is a good indication that CO burnout is occurring due to the corresponding trends in CO and CO_2 and that the RVC is transporting hot products from the UCC section into the core section. When the emission values were averaged across the exit plane, a bulk combustor efficiency of 97.1 % was determined. This is a significant increase in efficiency over the 91.5 % bulk combustor efficiency that was observed prior to the flame being anchored in the seeder box.

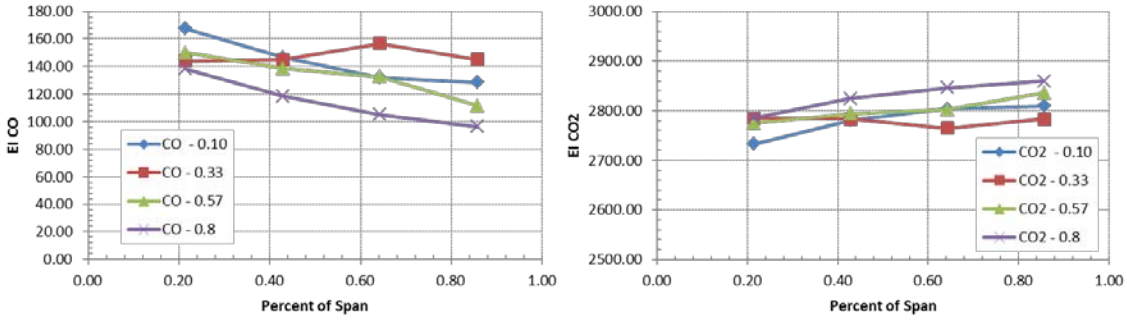

(a) **(b)**

Figure 5.10: Emissions Index for (a) CO and (b) CO2 for the RVC vane at MFR = 0.2, g-loading = 1000 g, and Φ = 2.2

When the vane was located on the top of the core section, a significant change in emissions occurred as seen in Figure 5.11. Looking at CO, CO_2, and UHC, it was observed that the highest EI of UHC and CO occurred at 80 % pitch and 21 % span with a correspondingly low EI CO_2 at the same location. However, the trend of decreasing CO and UHC with movement from the OD to the ID of the core section appears. This is

consistent with the increase in CO_2 with the same movement. Away from the OD, each of the pitchwise planes is relatively consistent except for the 80 % pitch plane. This plane consistently has the highest levels of CO and UHC. The bulk combustor efficiency for the RVC on the top of the core section is 96 % which is slightly less than the efficiency when the RVC was on the bottom of the core section.

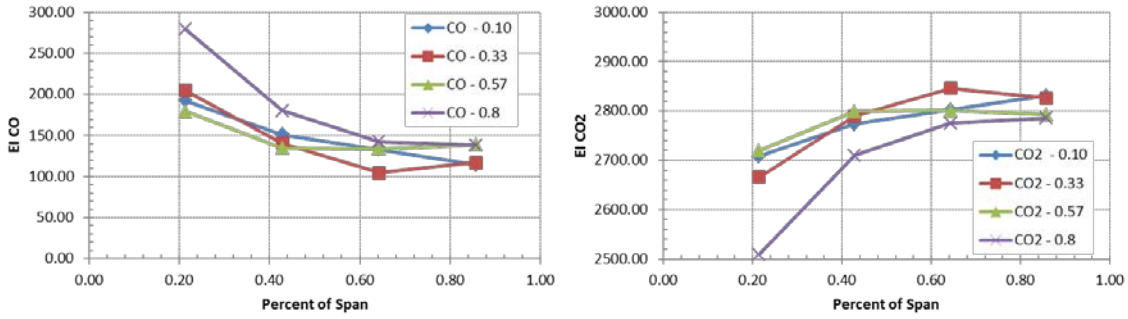

(a) **(b)**

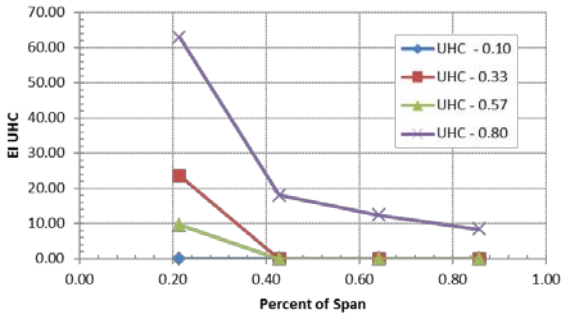

(c)

Figure 5.11: Emission Index for (a) CO, (b) CO_2, and (c) UHC for the RVC vane located on the top of the core section for MFR = 0.2, g-loading = 1000 g, and Φ = 2.2

With the vane on top of the core section, MFR = 0.1 was used to quantify the changes in emissions characteristics with changes in MFR. Figure 5.12 shows slightly elevated EI CO at Point 13 on the exit plane with a correspondingly low EI CO_2. It is seen that the trends are rather similar for EI between the two MFR cases, but Points 5 & 9

show an increase in EI UHC over the same property at MFR = 0.2. With the sharp decrease in UHC, it is quite apparent that any UHCs are remaining on the OD of the core section and not propagating across the span of the vane. The bulk combustor efficiency for the MFR = 0.1 case is slightly higher than at an MFR = 0.2 at 96.1 %.

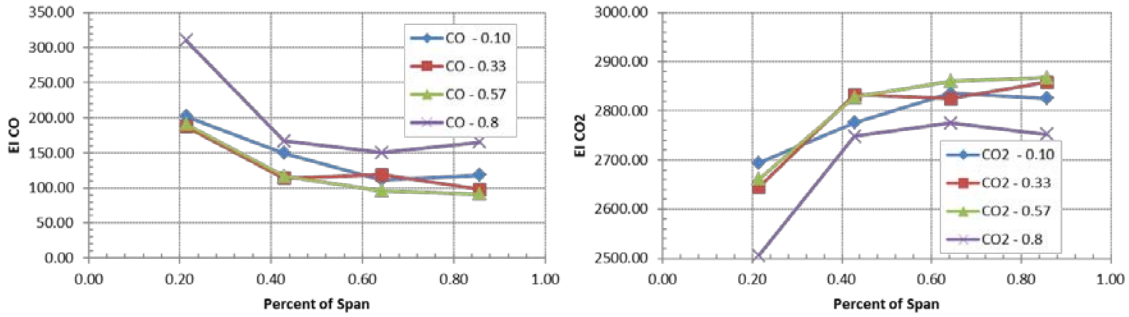

(a) **(b)**

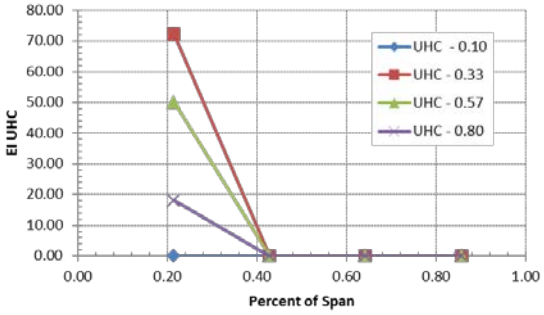

(c)

Figure 5.12: Emission Index for (a) CO, (b) CO_2, and (c) UHC for RVC vane on the top of the core section for MFR = 0.1, g-loading = 1000 g and Φ = 2.2

5.2.2 Tiger Claw Effect on Emissions at Core Section Exit Plane

The emissions results for the tiger claw are the necessary components to satisfy the main objective of this research: desensitize the flow to changes in operating conditions. In order to be able to determine if the tiger claw has successfully accomplished this objective, it is important to see how the tiger claw acts at a normal operating point.

Figure 5.13 highlights the EI CO, EI CO_2, and EI UHC results. Several similar trends were observed such as the general trend of decreasing EI CO and EI UHC with spanwise movement from OD to ID. There is the corresponding increase in CO_2 with the same movement. The decreasing CO is most likely due to the encounter with the fresh air in the core section. This is causing the CO to burnout and produce CO_2. There is the interesting trend of increasing CO along the 10 % pitch plane that has not been observed in any of the previous experiments. The bulk combustor efficiency for this scenario was 93 %. The appreciable drop in efficiency over the previous vanes is the significant increase in CO and subsequent decrease in CO_2.

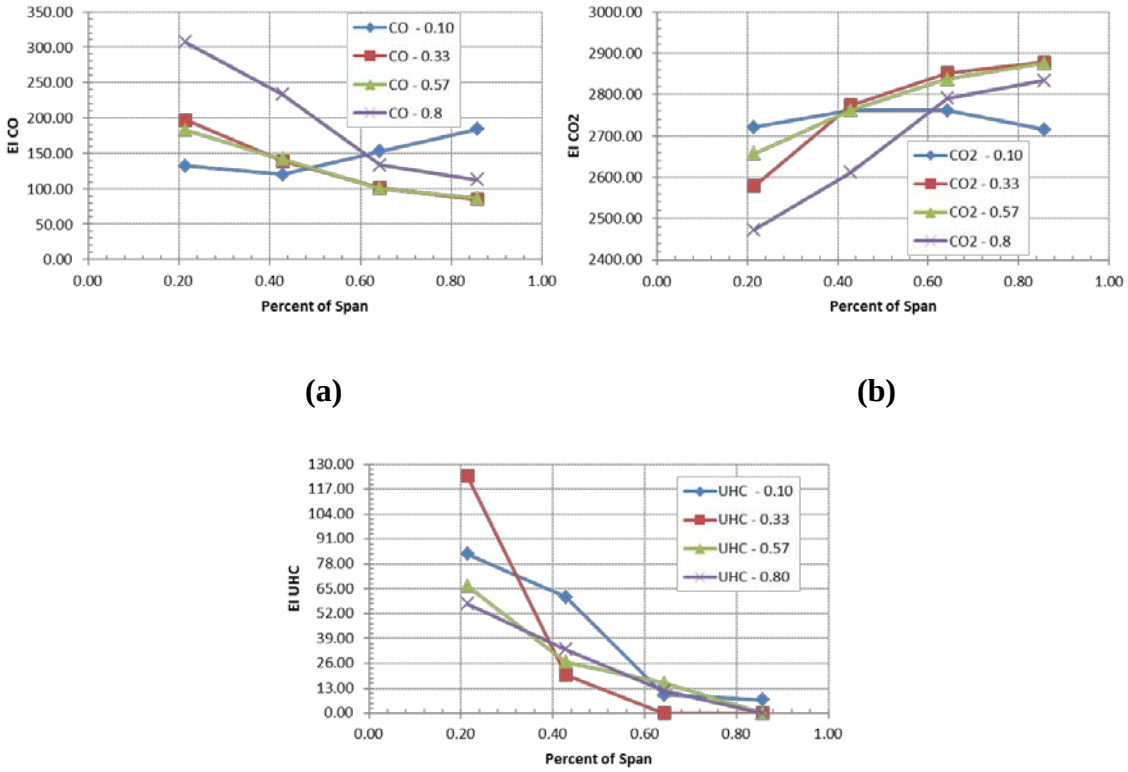

Figure 5.13: Emission Index for Tiger claw at MFR = 0.2, g-loading = 1000 g's, and Φ = 2.2 for (a) CO, (b), CO_2, and (c) UHC

Exploring the effects of changes in MFR, Figure 5.14 shows a drop in EI CO and EI UHC. The 80 % pitch plane continued to be significantly high in EI CO and low in EI CO_2. The largest difference in trends is that the 10 % pitch plane behaved like the other planes as opposed to what was observed at an MFR = 0.2. This case had an increase in bulk combustor efficiency to 96.4 %.

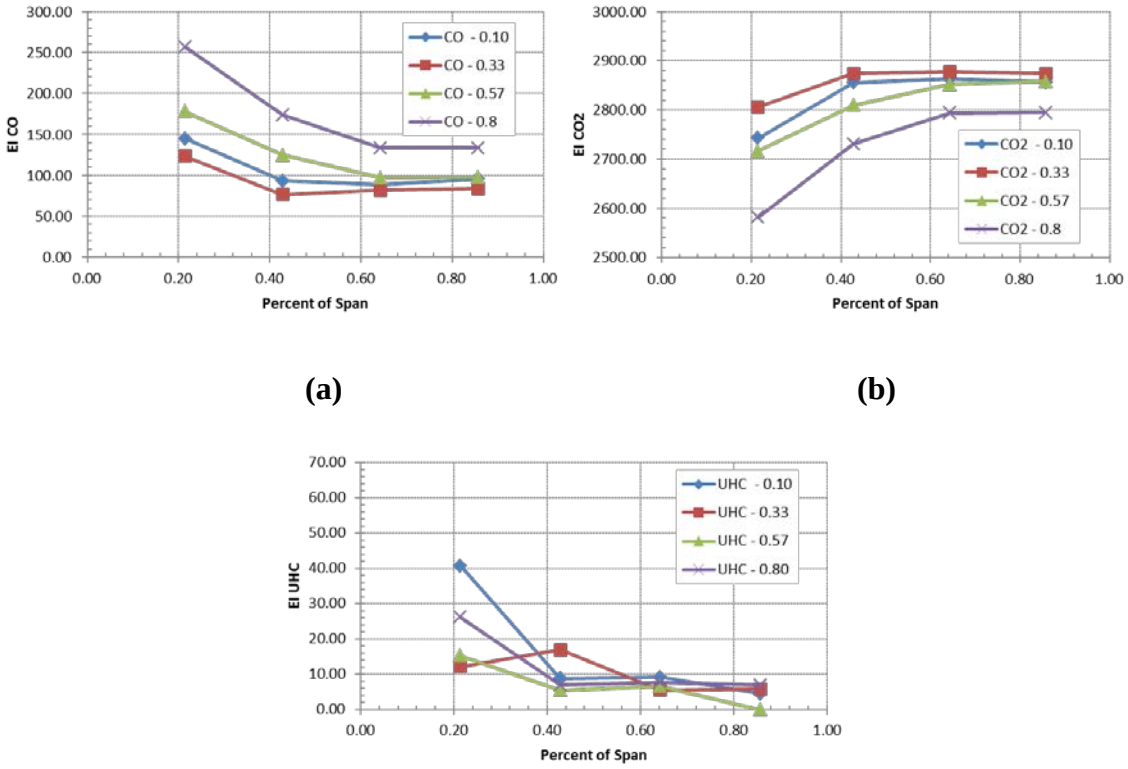

Figure 5.14: Emission Index for tiger claw at MFR = 0.3, g-loading = 1000 g's, and Φ = 2.2 for (a) CO, (b) CO2, and (c) UHC

The characteristics of the tiger claw emissions spectrum were continued to be explored with an MFR = 0.1. Figure 5.15 highlights the trends experienced at the new MFR. The magnitude of the EI CO was at the same levels observed for an MFR = 0.2.

For EI CO_2, there is less than a 10 % change for all pitch levels except the 80 % pitch plane. Combined, this provided a bulk combustor efficiency of 92.9 %.

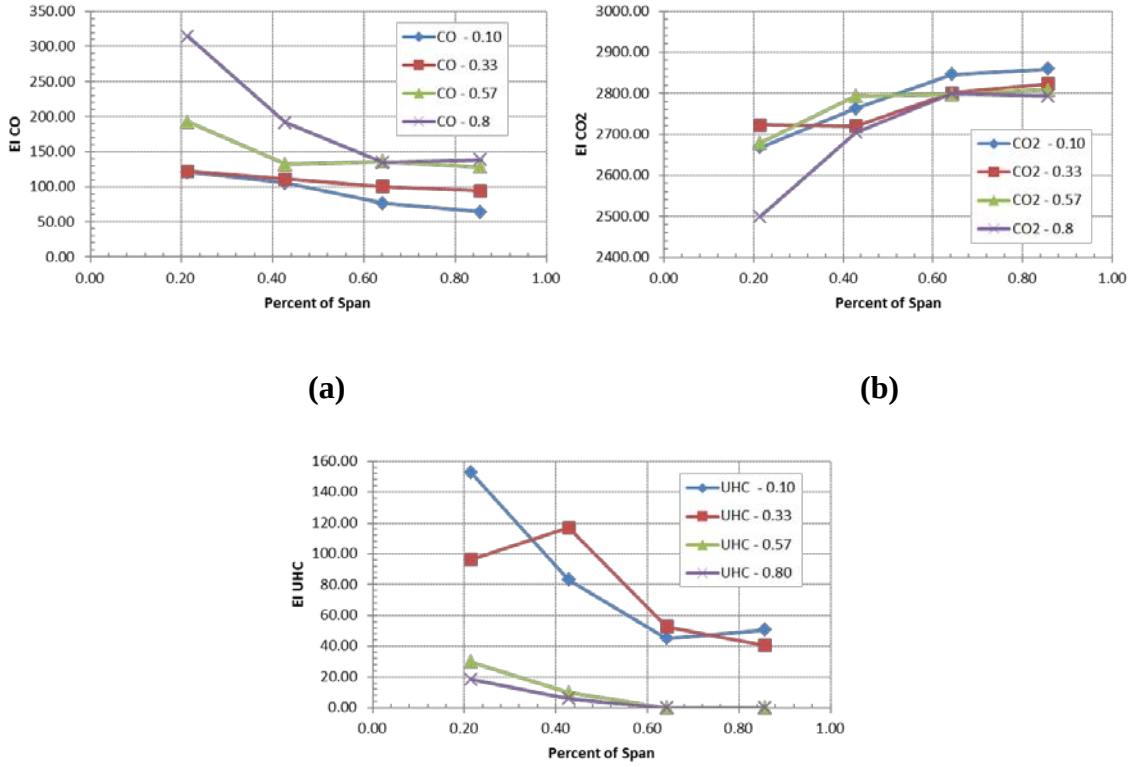

Figure 5.15: Emission Index for tiger claw at MFR = 0.1, g-loading = 1000 g's, and Φ = 2.2 for (a) CO, (b) CO2, and (c) UHC

Overall, the emissions characteristics at the MFR = 0.1 and 0.2 cases were very similar. The significant change in characteristics only occurred when MFR = 0.3. It was documented earlier that the HSV showed a widening of the flame in the core section with an increase in intensity along the bottom surface of the core section over the MFR = 0.2 and 0.1 scenarios (see Figure 5.7). The emissions data in conjunction with the HSV data

seems to indicate that there is an increased amount of mixing occurring at an MFR = 0.3 leading to an increase in CO blowout. The ending result is an increase in efficiency.

The centrifugal loading was also varied. The 500 g scenario was executed with most of the data following the same trends that have been seen in the other scenarios. Figure 5.16 highlights the results from the experiment. Since the experiment was operated at an MFR = 0.2 and Φ = 2.2, the results are very similar to that appearing in Figure 5.13.

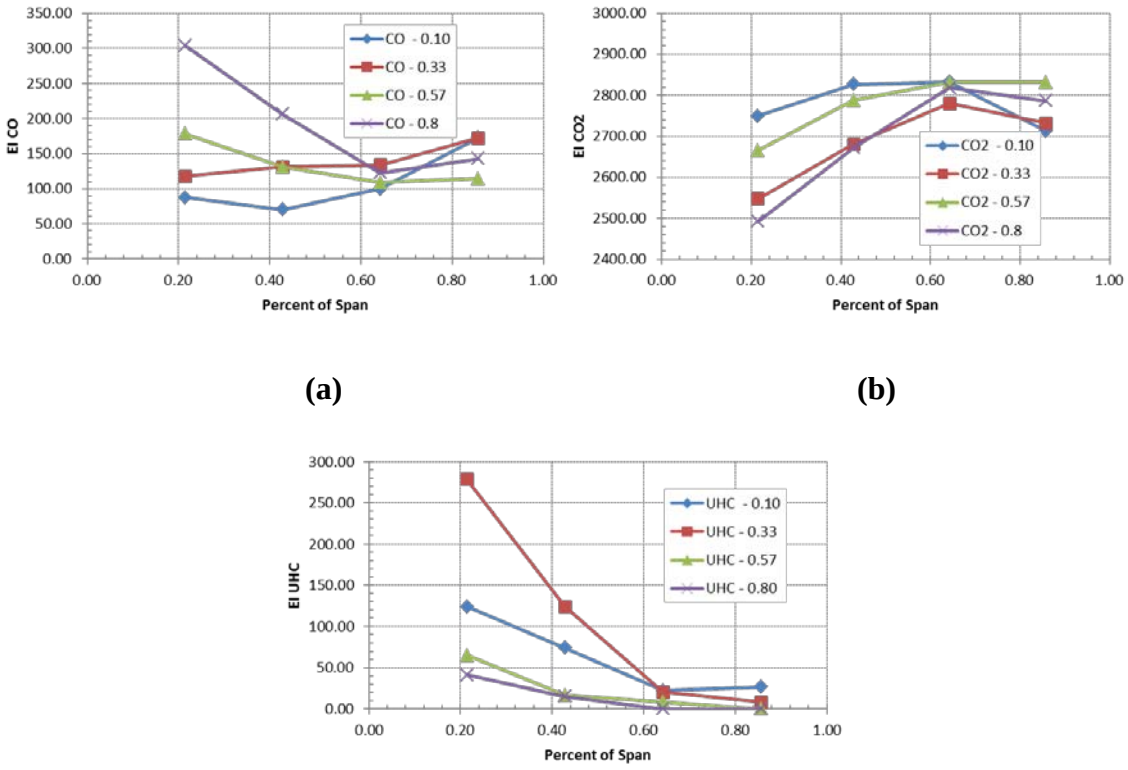

(a) **(b)**

(c)

Figure 5.16: Emission Index for tiger claw at MFR = 0.2, g-loading = 500 g's, and Φ = 2.2 for (a) CO, (b) CO2, and (c) UHC

5.3 Discussion

The first observation from the HSV and emissions data is the desensitization of the flame characteristics with operating parameters. Figure 5.7b and 5.7c along with the emissions results in Figures 5.13 and 5.15 easily show that the tiger claw distributes the flame and constituents across the span of the vane. The tiger claw is successful, though, only at MFR = 0.2 and 0.3. The tiger claw has difficulty in overcoming the increase in core mass flow rate at an MFR = 0.1. It is observed in both the HSV and emissions results that an MFR = 0.1 still significantly changes the behavior of the flame.

While it is apparent the tiger claw is desensitizing the flow, more work needs to be accomplished in order to successfully desensitize the flow at all operating conditions. One thing that may help is the addition of a film-cooling scheme similar to the one depicted by blue dots in Figure 5.17. The cooling scheme would serve three purposes. First, it would be used to keep the vane cool. This would extend testing times and enable better steady state emissions response. Second, the cooling would help keep the flow within the three channels in the tiger claw. Keeping the flow within the channels is important at higher MFR ratios where the circumferential flow may have enough momentum to travel across the channels if the cooling scheme was not in place. Third, the cooling jets will disrupt the cross flow. With an appropriate blowing ratio, the cooling jets should disturb the cross flow enough that at low MFR ratios, the circumferential flow will be able to enter the tiger claw channels. At low MFR ratios, the core flow has a significant momentum advantage which has a tendency to keep the circumferential flow from filling the core section. Therefore, a disruption of the core flow momentum would allow the circumferential flow to unabatedly fill the channels.

With the implementation of such scheme, the tiger claw should successfully desensitize the flame characteristics at all operating conditions.

Figure 5.17: Potential film-cooling scheme

The second observation is the variance in combustor efficient across the different operating parameters and vane geometries. It has been customary to compare the combustor efficiency results from the AFIT UCC test section to those gathered by Zelina et al. [2] on the AFRL full annulus. The experiments conducted on the AFIT UCC test section yielded combustor efficiencies between 93 and 97 %. This is less than the anticipated 99 % as reported by Zelina et al. One significant different between the two sets of data is where the emissions data was collected in relation to the main vane. The experiments conducted in this document measured the emissions at a quarter chord downstream of the main vane. Zelina et al. measured the emissions at a length greater than one chord downstream, giving the constituents almost an additional chord length to finish combusting. If the measurements had occurred at the same location downstream, the efficiencies would be even more similar.

Continuing to explore the combustor efficiency, Figure 5.18 graphs the combustor efficiency (in percent) for each vane geometry and operating condition. It was noticed that the tiger claw consistently produced the lowest combustor efficiency except at an MFR = 0.3. Each of the other airfoils produced a combustor efficiency in the high 96 %

range. An investigation into why the tiger claw efficiency was so low ensued. Looking at Figure 5.7c (tiger claw with MFR = 0.3), it was noted that in this scenario the flame in the core section had a similar shape and intensity to the flames for the RVC and solid vane. This led to the theory that the tiger claw was obstructing the mixing of the UCC flow with the core flow. Thus, CO was not being consumed and the combustor efficiency was remaining low.

One may recall that in Chapter 4, HSV results showed that the flame in the core section formed a helical structure as shown in Figure 4.2. Using the HSV results in the spanwise direction of Case 9 from Table 3.3, Figure 5.19 shows four consecutive images of the flame exiting the core section. It is noted that there is not a swirl component visible in the core section. It is the conclusion that the tiger claw is effective at desensitizing the flame's response to operating conditions because it turns the UCC flow axial. This turning restricts the UCC flow from hitting the ID endwall and creating the bulk swirl component seen in other configurations (see Figure 4.2). This bulk swirl component is critical in mixing the UCC section products with the fresh O_2 from the core air flow. Therefore, the desensitization of the flame characteristics come at the cost of decreased mixing leading to lower combustor performance.

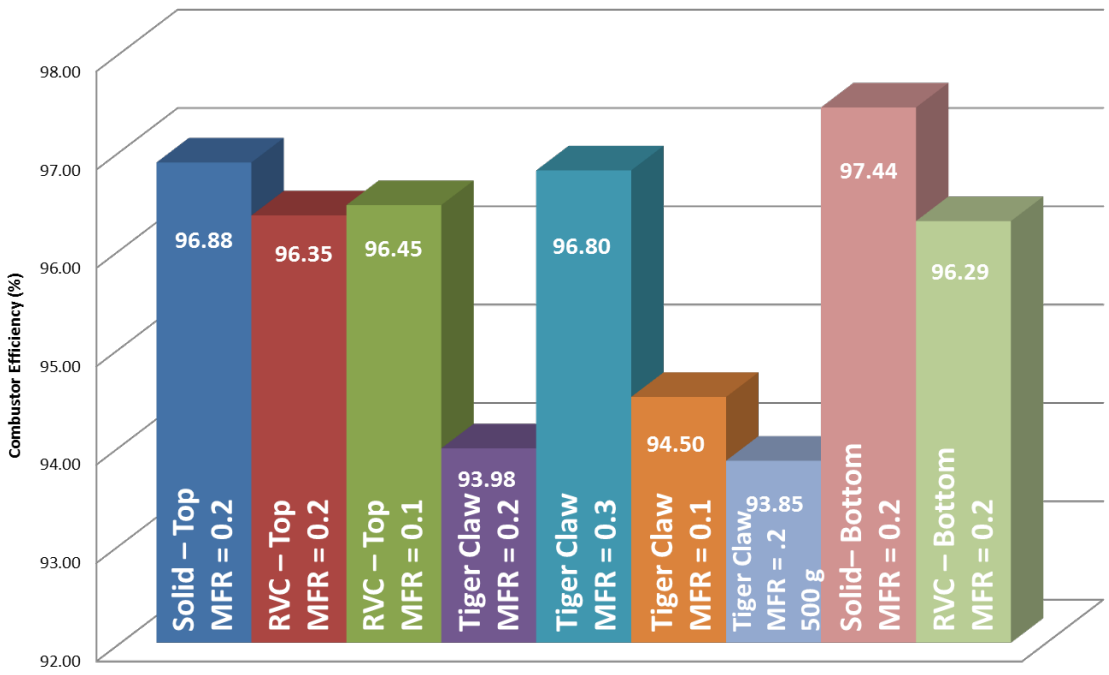

Figure 5.18: Combustor efficiency for each airfoil at a g-loading of 1000 g unless otherwise stated

The last observation to be discussed in this report has less of a conclusion to be drawn but more of a question for future research. It was observed that there was no noticeable change in combustor efficiency between the RVC located on the top versus the bottom of the core section. However, the solid vane on the bottom had the highest overall efficiency. This was contrary to what was expected. It was expected that the RVC on the top would have the highest combustor efficiency. This led to the question, is the vane on top of the core section drawing in more mass? If so, the constituents may not have the necessary time to finish reacting thus accounting for the decreased combustor efficiency. In a full annulus, the outlet products have to conform to conservation of mass; therefore, it is obvious that the mass is constant regardless of the vane being used. However, for the sectional rig with two possible exits, the amount of mass entering the core section does not have to be the same every time. Therefore, it is imperative for a

more accurate method of measuring mass transfer between the UCC and core section be established. This will allow for emissions data to be corrected or normalized based upon the amount of mass entering the core section.

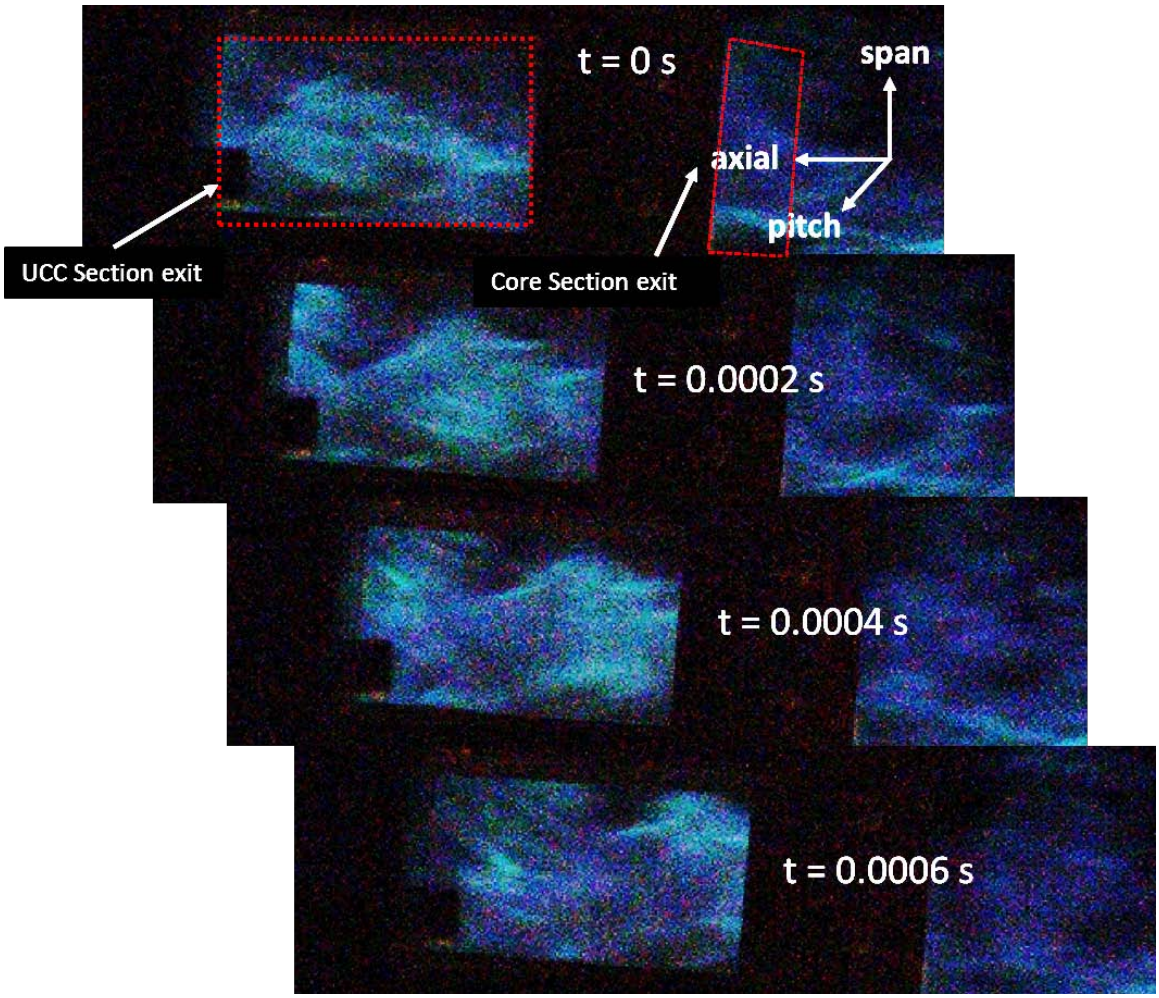

Figure 5.19: HSV results (bottom view) of the tiger claw at MFR = 0.2 showing no bulk flow in the core section

VI. Conclusions and Recommendations

6.1 Conclusions

The work presented in this document details an investigation into the AFRL UCC test section. The experimental investigation supported the main objective which was to show a desensitization of the flame characteristics in the core section to variations in operating parameters. Several modifications were made to the AFIT UCC test section in order to increase its ability to replicate the characteristics of a UCC full annulus. Once the modifications were complete, a baseline of the characteristics of the flame was well documented for a variety of configurations and operating parameters. Finally, a novel vane concept was implemented in an effort to reduce the flame's dependence on MFR and centrifugal loading, thus completing the objective of this work.

The modifications to the AFIT UCC test section were critical to completing the main objective. The most significant modification was fixing a u-channel into the seeder box to create a recirculation zone and ultimately a flame holder. This allowed the flame to consistently anchor itself in the seeder box. This modification had a three-fold effect. First, it allowed the division of fuel amongst the fuel injectors to accurately replicate that of a full annulus. As a consequence, this lowered the blowing ratio of the fuel injectors in the UCC section. Lowering the blowing ratio fixed a problem that had been noted in early experiments of the test section not replicating the efficiency of a full annulus. Through the lower blowing ratio and anchored flame, the AFIT UCC test section more accurately represented the characteristics of the AFRL full annulus. Third, the anchored flame caused the results to be very consistent. It removed a frequency in the flame that had been previously documented, and allowed for a more uniform combustion process to

occur. Ultimately, the anchoring of the flame in the seeder box was critical to the success of the objectives. Without having the anchored flame, a baseline of the flame characteristics (particularly the emissions characteristics) could not have been established and the desensitization could not have been shown.

There were minor changes to the flame characteristics when the vane was located on the top or bottom of the core section. However, it became apparent that there is a critical need to be able to accurately estimate the amount of mass transfer from the UCC to the core section. With this being an unknown quantity, it is difficult to describe the changes in flame characteristics when the vane was located on the top or bottom of the test section.

The implementation of the novel vane concept, the tiger claw, fulfilled the objective of this work. The tiger claw created an emissions profile that was more uniformly distributed across the span of the vane at multiple operating conditions. In addition, the HSV showed an even distribution of the flame intensity across the span of the vane at an MFR = 0.2 and 0.3. The tiger claw had difficulty in being able to desensitize the flame characteristics at an MFR = 0.1. It was also noted that the tiger claw desensitized the flame characteristics at the expense of combustor efficiency. This was attributed to the tiger claw removing the helical swirl motion typically present in the core section. The lack of this bulk movement decreased the mixing occurring in the core section and dropped the efficiency of the combustor. The tiger claw experiments successfully met the objective of the work and showed that desensitization of the flame occurred.

6.2 Recommendations

The work presented in this document took the initial step into normalizing the core sections exit plane characteristics. Further research is needed in order to develop the best solution to controlling the flow at all operating conditions. The first step should be to apply a cooling scheme to the current tiger claw vane. The cooling scheme should be in spirit with the one outlined in Chapter 5. The scheme should be experimentally tested to document any increases in combustor performance as well as the ability to better control the flames shape as it enters into the core section at low MFR ratios.

A numerical study should occur for various iterations on the tiger claw vane. This should include changing the channel heights, widths, number of channels, and the addition of film cooling holes. Distributing UHC across the span of the airfoil in addition to fully mixing it with the core flow is imperative to increasing the efficiency and providing uniform exit plane characteristics. It may be found that applying a channel characteristic allows for a simpler cooling scheme to be applied. The numerical study should provide a handful of concepts to be tested in the AFIT UCC sectional.

Several modifications can still be made to the current AFIT test section or applied to the future test section. First, every component junction needs to be sealed. Often during testing, flames would suddenly shoot out of the interface between two components. Because the designers of the first AFIT UCC section did not take into consideration the degradation of interfaces, the current rig leaks often. This caused numerous delays in just trying to get the components to seal correctly. In addition, for long periods of testing (i.e. when taking emissions measurements) the rig should be cooled. This would allow the rig to be brought up to a steady state temperature and

maintained for the duration of data collection, instead of having the shut off the rig every few minutes because of its bright red glow.

A more definitive method of calculating the mass transfer between the UCC and core sections needs to be developed. For the current research, there was not a validated method of determining if the vane located on the bottom of the core section brought in more or less mass than when the vane was on the top of the core section. In addition, it is important to quantify the amount of mass transfer to ensure the sectional model is accurately replicating the full annulus.

While in this work, the flame location and emissions results were used colloquially to show the trends in temperature distribution, it would greatly enhance the validity of the work to take temperature measurements that highlight a more even distribution over the span and pitch of the vane cavity. With the implementation of these four recommendations, future work on the AFIT UCC test section should accurately represent the AFRL full annulus and provide a critical step in integrating the UCC into a turbine engine.

Appendix A: COAL Laboratory Operating Procedures

I. Introduction:

In order to conduct a combustion experiment in the COAL Lab, be it with or without the operation of the UCC, it is necessary to understand the operation of several key lab systems. These essential systems include: Labview data acquisition software, mass flow controllers, fuel systems (propane in this case), imaging systems, and laser diagnostic systems such as, Particle Image Velocimetry (PIV) and Planar Laser Induced Fluorescence (PLIF). While the aforementioned processes are, by no means, a definitive list of the capabilities of the COAL Lab, they are fundamental to the conduction of many combustion experiments.

Note: Several of the following steps require up to an hour to complete; so, it is important, that if you need to test by a certain time, to start early.

Combustion experiments may create noise in high decibel ranges; be sure to wear ear protection when necessary.

Before conducting any Laser experiment, make certain to wear proper eye protection and to turn on laser warning light!

Final Shutdown procedures for the Lab are at the end of the document, XIV. Final Shut – Down

To follow is an outline of the various procedures mentioned above:

II. Preliminary Procedures – UCC

Prior to running experiments, a few steps must be completed.

a. Turn on the "Equip" switch (left) at the lab control station (see Figure A.1).

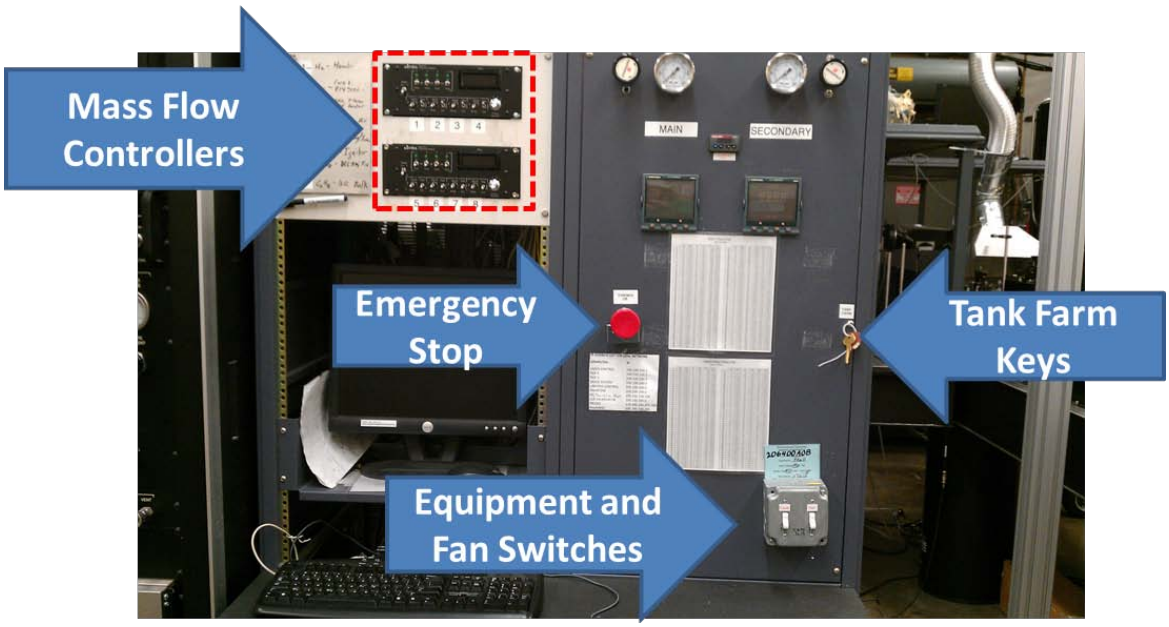

Figure A.1: Equipment located at the Lab control station: the "Equip" switch (left) for laboratory equipment and the main UCC hood ventilation "Fan" switch (right)

b. Turn on the Mass Flow Controllers (MFC's) (only main power switch on both units, see Figure 2, not each individual channel)

i. Approximately **one hour** must elapse prior to sending any mass flow through any line that is controlled by the MKS MFC's

****NOTE** Channels 1-4 are controlled through Labview while channels 5-8 are only read in Labview and must be controlled manually**

Figure A.2: MKS Manual Mass Flow Controllers (MFC's): switches 1-4 on the top MFC and channels 5-8 on the bottom MFC

c. *If conducting PIV experiments, follow the steps in* **V. Particle Image Velocimetry (PIV)** and then follow then return to **III. UCC Operation**

d. *If conducting PLIF experiments, complete the steps outlined in* **VI. Planar Laser Induced Fluorescence (PLIF)**

e. Follow steps for propane start - up in **VII. Fuel Procedures (C_3H_8 – Propane)**

f. Follow steps for **Ethylene and Air** start - up in **VIII. Other Tank Farm Procedures**

III. UCC Operation

a. Using the Labview Control computer (IP: 100.100.100.5), open the Labview file, *Parks.vi* (see Figure A.3) located on the desktop

b. Press the "run" button (an arrow) in the top left corner of the Labview window following one hour MFC warm up (see Figure A.3)

c. Error message will pop up; click "Continue"

Figure A.3: *Parks.vi* Labview file control panel

d. Open the manual valves on the Primary and Secondary air lines slowly
   i. If the airflow sound is persistent, check the main flow and/or secondary flow set points in Labview

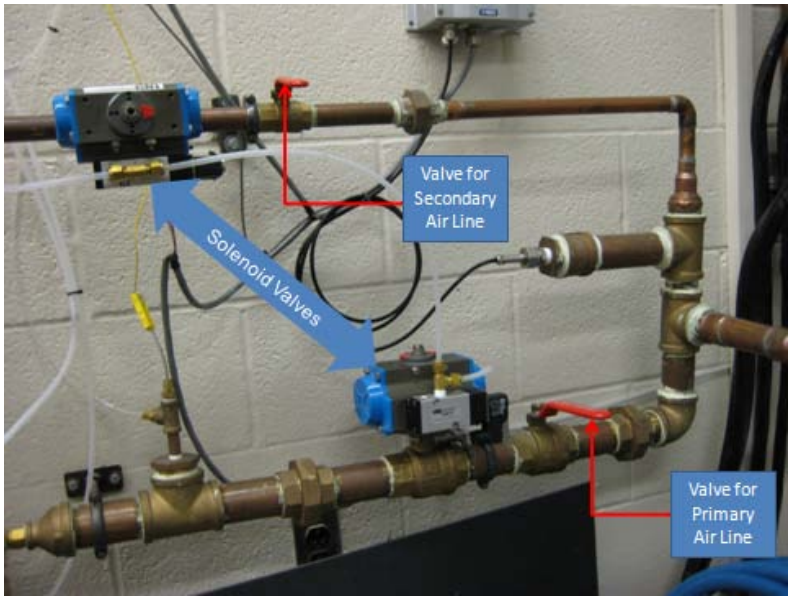

Figure A.4: Main and Secondary air supply lines with manual shut-off valves and pneumatic valves controlled by LABVIEW

e. On the Black Box (see Figure A.5), turn the switch for the HVOF to "off" and turn the switch for the UCC to "on"

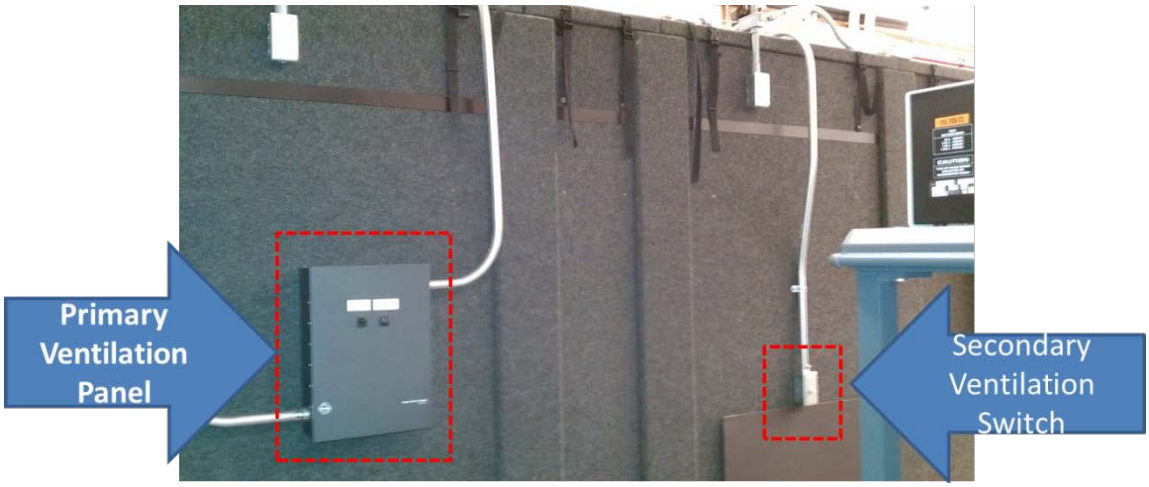

Figure A.5: Power supply for Primary (left) and Secondary (right) ventilation system

f. Turn the switch for the Fan system on (see Figure A.1), located at the lab control station
  - **i.** Turn on the Secondary ventilation system, located on the side of the Black Box (see Figure A.5)

g. **In Labview (Starting UCC) (Test Flame):**
  - **i.** Set air flow rates
    1. Main (Core Flow)
    2. Secondary (UCC Flow)
    3. Check air set points vs. air readings
    4. Set zero air and ethylene set points (Set Points 5 & 6 respectively, see Figure A.3)
       - **a.** Air: 14 lpm
       - **b.** Ethylene: 3 lpm
  - **ii.** Set the propane flow rates set points
    1. For set point 7 (curved section) and set point 8 (Seeder Box) (see Figure A.3)
  - **iii.** Open Solenoids from left to right (Nitrogen is not necessary for basic procedure)
    1. Air
    2. Ethylene
    3. Fuel
  - **iv.** Turn on air and ethylene (channels 5 & 6, see Figure A.3)
  - **v.** Turn igniter "On" (see Figure A.3)
  - **vi.** Turn on seeder box fuel (channel 8, see Figure A.3)
  - **vii.** Once seeder box fuel has ignited, turn igniter "Off"
  - **viii.** Turn on curved section fuel (channel 7, see Figure A.3)
  - **ix.** Turn off channels 5 & 6
  - **x.** Close ethylene and air Solenoids

h. *If conducting PIV experiments, complete the steps for* **Operation** *in* **V. Particle Image Velocimetry (PIV)**

i. *If conducting PLIF experiments, complete the steps for* **Operation** *in* **VI. Planar Laser Induced Fluorescence (PLIF)**

IV. UCC Shut – Down **NOTE It is important to shut the flame down between experiments or every ten minutes to allow for cooling.**

a. In Labview

i. Turn off fuel (channels 7,8)

ii. Turn off fuel solenoid

iii. Keep Main and Secondary Air flow rates at around 0.5 kg/min between tests in order to cool the UCC quickly.

iv. If more experiments are necessary, go back to **III. UCC Operation, g.**

v. See **XIV. Final Shut – Down** for procedures to shut the lab down after experiments are complete.

V. Particle Image Velocimetry (PIV)

a. Start - Up

i. Turn on the cooling unit for the Verdi V12 Laser (switch is located on right side near the bottom, see Figure A.6)

1. Set point should be 18.0 degrees Celsius

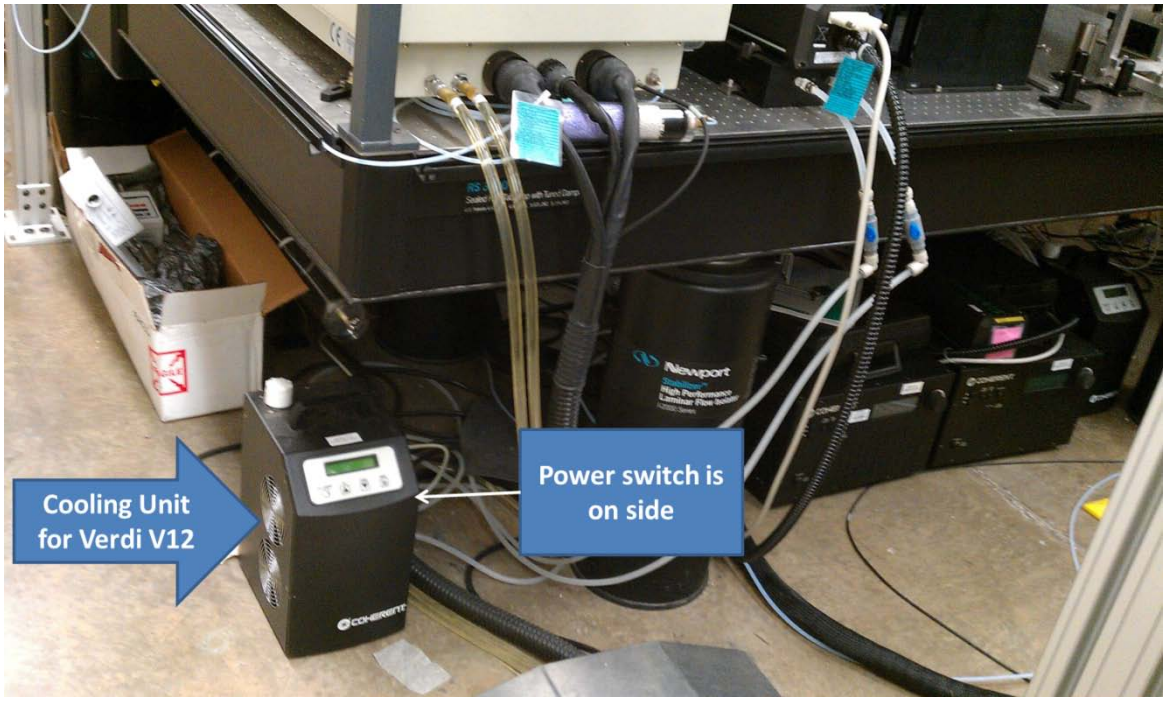

Figure A.6: Cooling Unit for the Verdi V12 Laser located beneath the Verdi V12 Laser

ii. Turn on Verdi V12 power supply (see Figure A.6), located beneath the Verdi V12 Laser to the right of the cooling unit (switch is located on back left side, just above power cord)

1. Will boot in "Current Control" (needs to be set to "Light Control")

a. On the power supply, push "menu select" button

b. "Menu" down 15 times to "Light/Current" control

c. "Menu select" twice
    i. Should read, "In Light Control Mode"
d. Menu exit twice

iii. Plug power in for the Phantom-Monochrome (4 pin B/C cord must be plugged into the back of Phantom-Monochrome)
    1. The camera takes about an **hour** to warm up.

iv. Warm up the laser for **30-45 min**

v. After the warm up period, on Verdi V12 Power Supply insert and turn the key from "standby" to "laser enable" (key is on top of power supply)

b. Operation

i. Commands

1. s=0: closes shutter
2. s=1: opens shutter
3. p=(enter number): sets the power level of the laser
4. ?p: displays current power level

****Note** Do not "backspace" in command prompt. If you do, hit enter and retype the command.**

ii. Remote desktop (see section **XI. Remote Desktop**) to "diode system" (IP: 100.100.100.4) using computer terminal to left of rig if at the back of the lab (see Figure A.7)

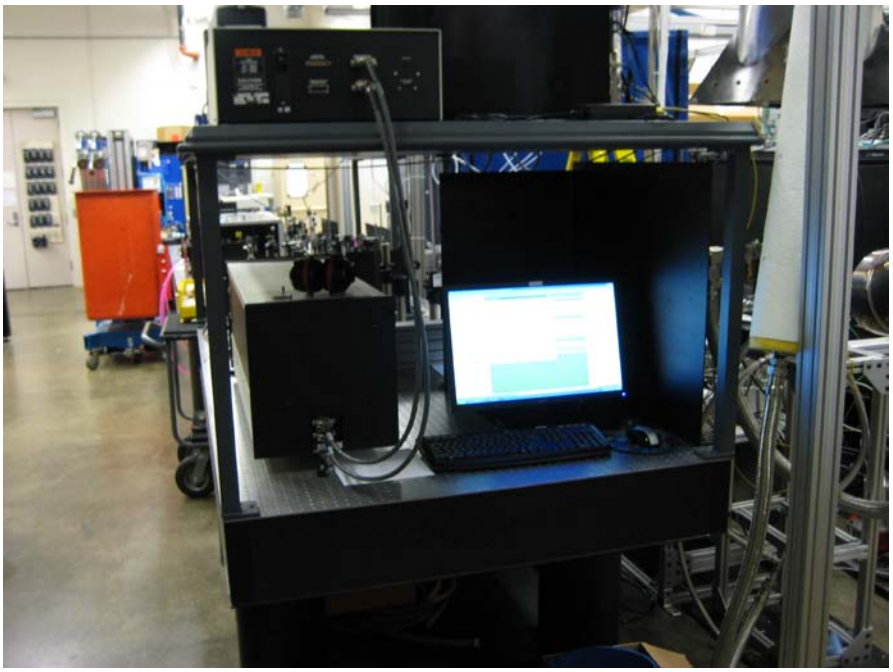

Figure A.7: Computer terminal to the left of the rig

iii. Open Verdi V12 Terminal program (command window will appear)

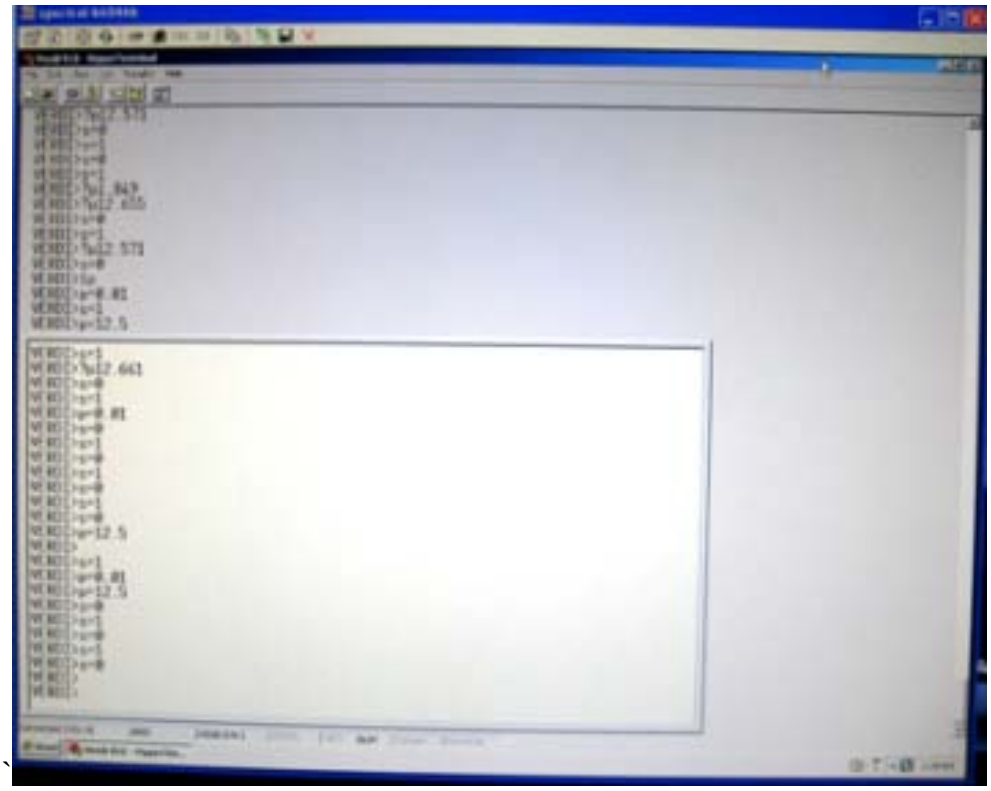

Figure A.8: Above, is the command window for the Verdi V12 Laser.

i. Open the shutter ("s=1") (shutter can also be controlled from the Verdi V12 power supply)
  1. Shutter should be closed at all times when not taking data
ii. Set the power level of the laser to 12.5 ("p=12.5")
iii. On the LABVIEW Control panel open the N_2 solenoid
iv. Turn on Manual MFC channels 2 and/or 3 depending on the airflow needed (see Figure A.2)

c. Seeding

i. Seeder Start - Up and Operation
  1. If seed particles are needed, unscrew the tops from each of the seed containers to clean the containers and insert more seed (see Figure A.9)
    a. Be sure to close shutter on laser (s=0)
    b. To clean seeder, see **IX. Seeder Cleaning/Maintenance**
    c. Re-attach the tops of the seed containers
ii. Open the Seeder Top Valve
iii. Open the Seeder Bottom Valve
iv. Close the Bypass Valve
v. Adjust vibration motor to achieve desired seeding, see Figure A.10 (About 50% power is usually sufficient)
  1. 20-60% power is acceptable for continuous running
  2. Any other power setting is subject to 50/50 duty load

vi. When seeding is sufficient, see section **XII. Imaging**

vii. Follow procedures for **Seeder Shut – Down** after each trial to conserve seed.

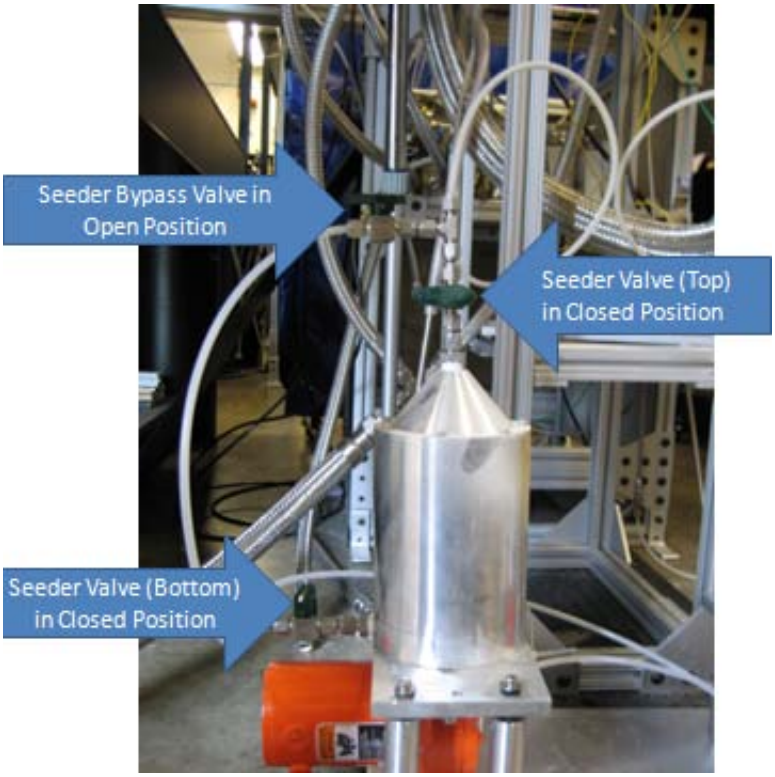

Figure A.9: One of two seeders for PIV Laser Flow Diagnostics in the UCC

Figure A.10: Control knob for one of the two vibrating motors attached to the seeders

viii. **Seeder Shut – Down**

ix. Open Bypass
x. Close Seeder Bottom Valve
xi. Close Seeder Top Valve
xii. Turn off vibration motors

d. Imaging (Phantom – Monochrome)

i. Refer to **XII. Imaging**

e. Shut – Down

i. Set power level of laser to zero ("p=0")
ii. Close the shutter ("s=0")
iii. Turn key on Verdi V12 Power Supply to "Standby"
    1. Remove and return key to the top of the power supply
iv. Turn off Verdi V12 Power Supply
v. Unplug the power for the camera
vi. Turn off cooling unit for Verdi V12

VI. Planar Laser Induced Fluorescence (PLIF)

a. Flushing and Refilling the Dye Laser

i. If needed, follow steps in **XIII. Flushing and Refilling the Dye Laser.**

b. Start – Up

i. Insert key into the YAG Laser Power Supply and turn it to the "on" position (See Figure A.11)
ii. Flip switch to the "on" position Spectra Physics YAG Laser Power Supply

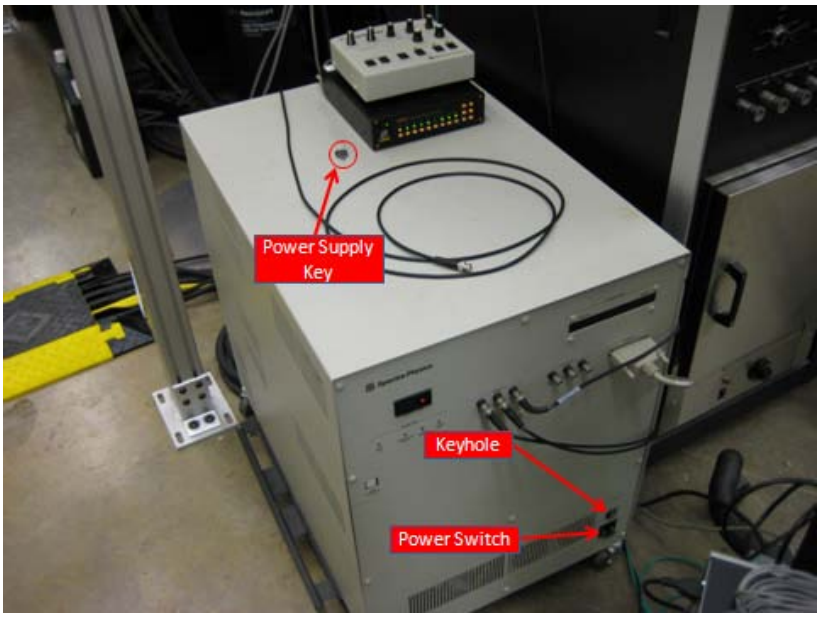

Figure A.11: YAG Laser Power Supply with Quanta-Ray timing box on top.

iii. Flip switch on the timing box, which is located on top of the power supply, to "enable" ****Note** OSC and AMP lamp energy should be in the "start" position**

iv. Turn on dye pumps by flipping switches located near the power cord on the back side of Abby and Betty.

v. Turn on both Princeton Instruments Camera Power Supplies, see Figure A.12 (located above Abby and Betty)

1. The power supplies will need an hour warm up time

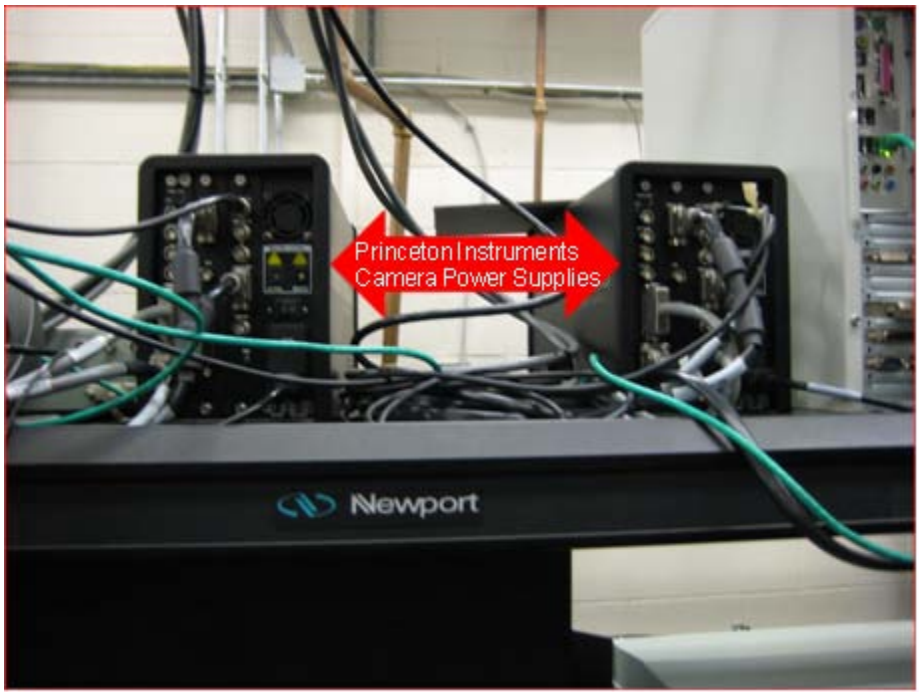

Figure A.12: Princeton Instruments Camera Power Supplies

vi. Open PLIF 1 and PLIF 2 Computers, via Remote Desktop (see **XI. Remote Desktop**) IP: 100.100.100.2 and 100.100.100.3, respectively

1. On PLIF 1 and PLIF 2, open "Winview"
2. Window will pop up
    a. Click on the option, "Restore last settings".
    b. Click "Ok"

vii. Slide shutters on Abby and Betty to closed position

viii. After the cameras and laser are warm (one hour for camera, 30 min for laser), turn "Lamp Energy" on the Timing Box (see Figure A.11) to 10

ix. Open the lid of each Dye Laser (Abby and Betty) and remove the beam block (see Figure A.13)

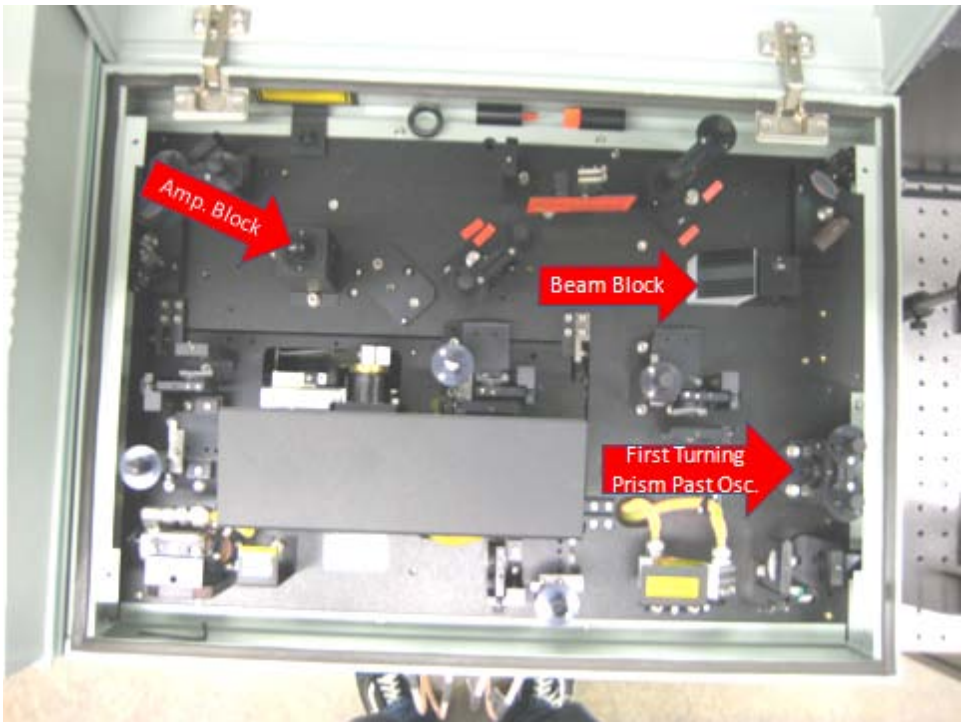

Figure A.13: Components inside a Dye Laser with Amp and Beam blocks highlighted

x. Lift Amp block (See Figure A.13)

xi. Open shutters when ready to start experiment.

c. Operation

i. Remote Desktop Laser Control (see **XI. Remote Desktop**) IP: 100.100.100.1

ii. Open "Trigger" program

1. Open file, "Dual Pulse YAG with Camera Sync 27_Oct_2010_Kenny"
2. Click on "Program"
   - **a.** Click on "Program all channels"

iii. Open Channel F (Camera 2)

1. Make sure that F is disabled

****NOTE** The following steps are to be completed in both Winview programs on both computers, PLIF 1 and PLIF 2.**

iv. Click on the "Acquisition" tab

1. Then click on "Experiment Setup"
   - **a.** Make certain to verify settings (*typical settings*):
     - **i.** number of images (*5000*)
     - **ii.** region of interest
     - **iii.** intensifier gain (*10*)
     - **iv.** Click "Ok"

v. Click on the "Setup" tab

1. Then click on "Pulsers"
2. Click on "Setup Pulsers"
3. Click on "Gating" tab

4. Click on “Setup”
    a. Verify settings
        i. Gate width
        ii. Delay
        iii. On – CCD Accumulation
    b. Click “Ok” three times

vi. Measure Dye Laser power before every trial; the power will vary.
1. Use laser power meter
    a. If power is below 120mW, adjust doubling crystal alignment to increase power or dye may need refilling see **XIII. Flushing and Refilling the Dye Laser**
2. Make certain that “Time Average” is off

vii. **Acquisition**
1. Click “Acquisition” tab
    a. Then click on “Acquire”
2. Instead of the above – mentioned technique, there is an acquire button, labeled, “Acq”
3. Start experiment so that the conditions in need of recording are attained
4. Click on the “File” tab and save images.
5. Repeat steps **viii.** and **ix.** as needed.

d. Shut – Down

i. Close Winview on both PLIF 1 and 2
ii. Turn lamp energy down on both “Amp” and “Osc”
iii. Stop the timing box
iv. Turn and remove key from power supply
v. Flip the power supply switch to the “Off” position
vi. Turn off Dye Laser Pumps
vii. Return Beam Block
viii. Shut Amp Block
ix. Close shutters
x. Refer to section **VII.** and **VIII.** for Propane and Bottled Gas shut – down
xi. Turn off both of the Princeton Instruments Camera Power Supplies

VII. Fuel Procedures (C_3H_8 – Propane)

a. Propane: Start - Up

i. Get keys for the Tank Farm from the Lab Control station (see Figure A.1) and unlock the padlock to the Tank Farm ****NOTE** The Tank Farm is to be <u>locked at all times</u>, unless you are in it!**

ii. Turn on the Vaporizer switch (see Figure A.14) with up being on

Figure A.14: Showing location of the power switch for the Vaporizer inside the Tank Farm.

iii. Completely open the valves on top of each of the three large propane tanks.

iv. Open the valves on the hoses from each propane tank (yellow handles)

v. Wait **15-30 minutes** (depending on outside air temperature) for the vaporizer to warm up before proceeding to the next step

vi. Open the valve immediately upstream (yellow) and immediately downstream (red) of the vaporizer (see Figure A.15)

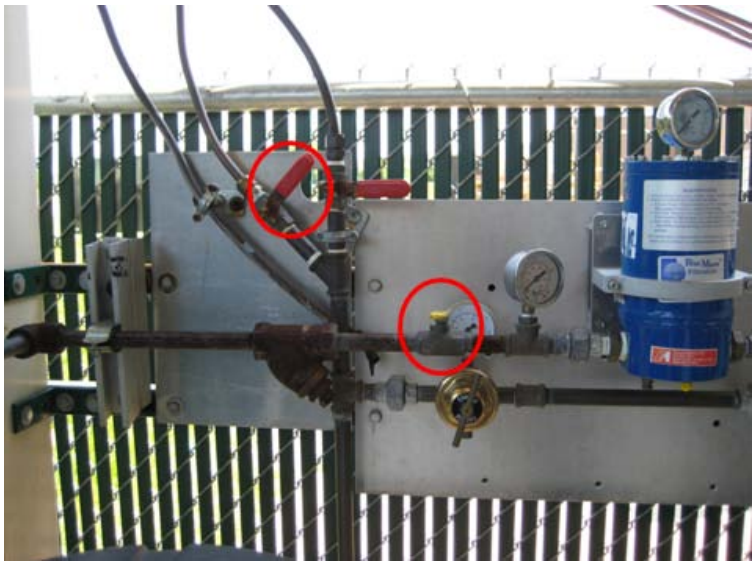

Figure A.15: Input (yellow) and Output (red) valves for the Propane Vaporizer, both "off"

vii. Open Propane valve in lab (see Figure A.16)

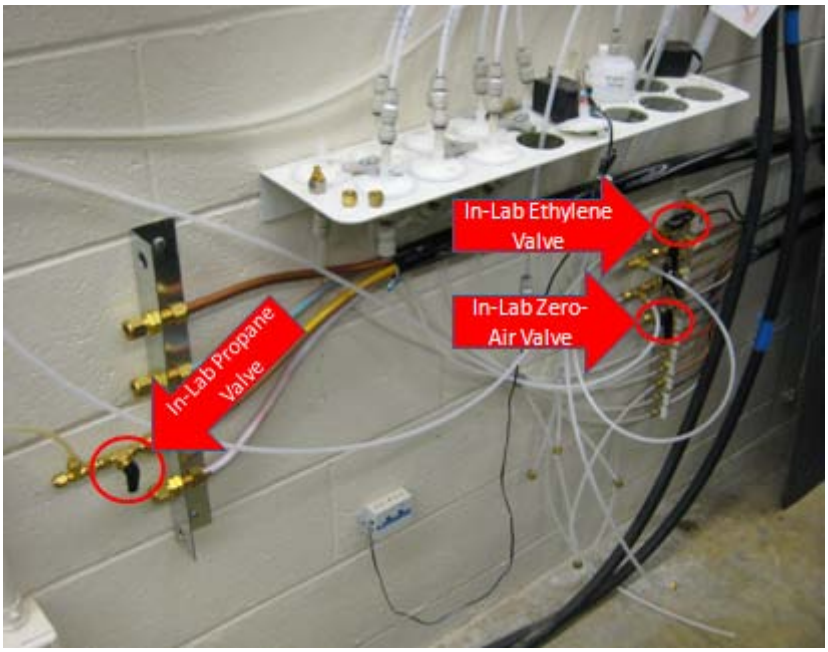

Figure A.16: Valve manifold for bottled gases and Propane on the East laboratory wall

b. Propane: Shut-Down and Bleed

- **i.** Close upstream (yellow) valve to the vaporizer (see Figure A.15)
- **ii.** Close valves on the three hoses from each Propane tank
- **iii.** Close completely the valves on top of each of the three large propane tanks
- **iv.** Flip the Vaporizer switch to the "off" position
- **v.** Open Fuel Solenoid
- **vi.** Steps **1-4** below are performed within to Bleed the Propane Lines
  1. Make certain that the ventilation fans are on.
  2. Set air flow rates for Main and Secondary lines to about .5-1 kg/min
  3. Turn on Fuel (MFC's #7,8)
  4. After Mass Flow for 7 and 8 reads approximately 0, complete the following steps
  5. Turn off Fuel (MFC's #7,8)
  6. Close Fuel Solenoid
- **vii.** Close Propane in-lab valve.
- **viii.** Close downstream (red) valve to the vaporizer (see Figure A.15)

VIII. Other Tank Farm Procedures

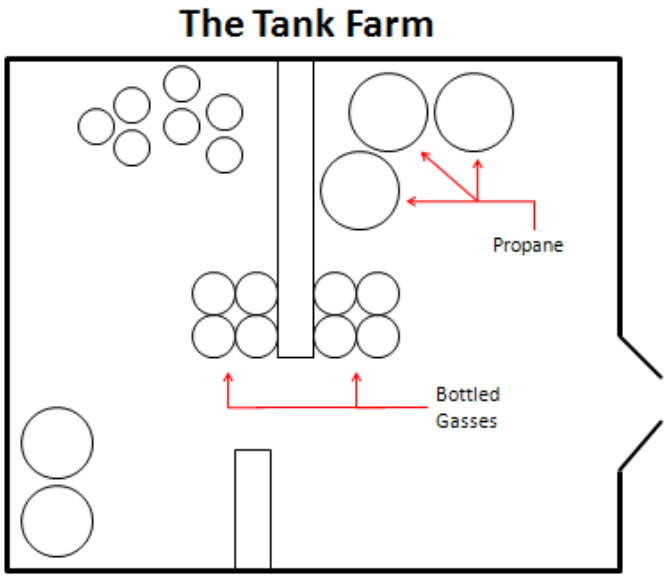

Figure A.17: Schematic of Tank Farm, showing location of the entrance, the three Propane Tanks, and bottled gas location

- **a. Bottled Gases in the Tank Farm, used by the COAL Lab**
  - **i.** Zero Air
  - **ii.** Ethylene
  - **iii.** Hydrogen
  - **iv.** Nitrogen
- **b. Bottled Gases: Start-Up**
  - **i.** Open valve directly on top of tank completely (do not change the current setting on the regulator)
  - **ii.** Open designated valve at the manifold (see Figure A.16)
- **c. Bottled Gases: Shut-Down**
  - **i.** Close valve completely
  - **ii.** Close designated valve at the manifold

IX. Seeder Cleaning/Maintenance

- **a.** Remove Seeder Containers from stand
- **b.** Remove the tops of each of the seeder containers
- **c.** Clean out any excess seed with a paper towel
- **d.** Remove the bottoms of each of the seeder containers
- **e.** Clean out each of the filters
  - **i.** May be necessary to shake or strike against inside of trash can
- **f.** Replace filters if necessary
- **g.** Check condition of each seeder containers o-rings
- **h.** Replace o-rings if necessary
- **i.** Put the seeder containers back together and reattach them to the stand

X. Translation Stage

- **a.** Turn on Power for the Translation Stage Controller

b. Open ESP control utility (on GC/Translation Stage computer IP: 100.100.100.100)

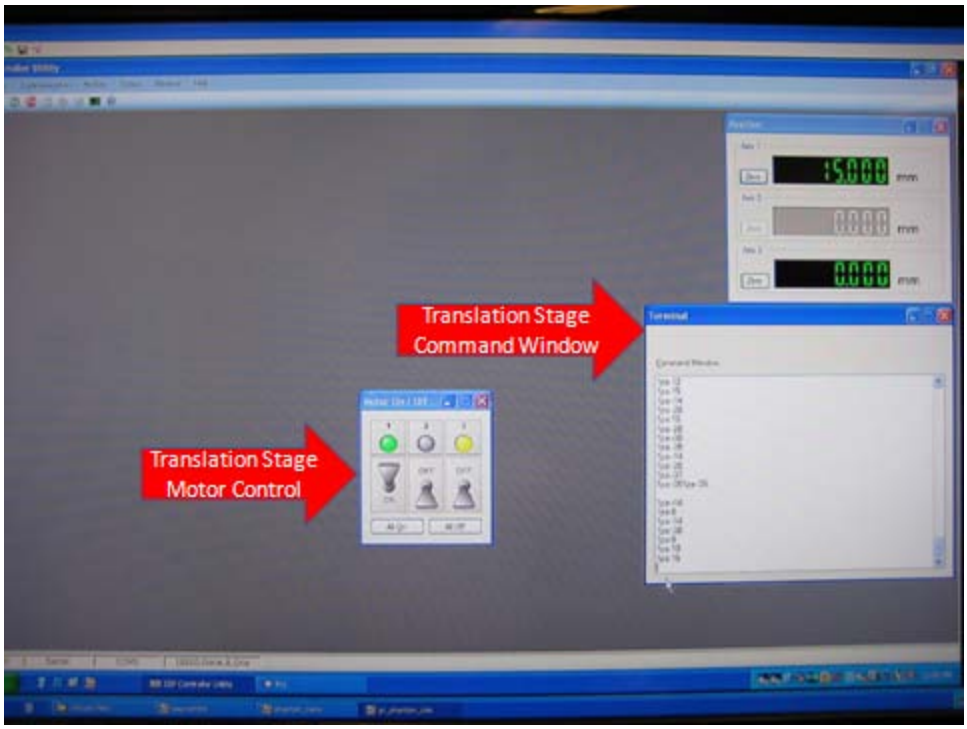

Figure A.18: Control windows for the UCC rig Translation Stage

c. Turn Motor 1 on
d. Type "1pa x"
- **i.** 1: axis
- **ii.** p: positive
- **iii.** a: absolute

****Note** If you turn Power for the Translation Stage Controller off, the position that it is in at the time of program termination becomes the new zero point.**

- **iv.** Return the stage to "0" before turning it off.

XI. Remote Desktop

a. Can access from any COAL Lab Network Computer
b. Open the TightVNC Viewer (In quick launch by the "Start" button
c. Type in IP Address for particular machine
- **i.** List of IP Addresses located at Lab Control Terminal

d. Password for Remote Desktop is, "password".

XII. Imaging

a. **Phantom Monochrome (#9575) and Color(#8531)** (Procedure is the same, just change the camera)
- **i.** Plug the power cable in for the camera.
- **ii.** Allow an **hour** to warm up
- **iii.** Open PCC 1.3 on computer next to test rig (in quick launch, next to "Start" button)
- **iv.** Click on "Live" tab

v. Choose camera from “Camera” pull down
    1. Phantom – Monochrome is 9575
vi. Set amount of images to be taken
vii. Perform Current Session Reference(CSR)
    1. Ensure lens cap is on Phantom
    2. Click CSR button
    3. Click “OK” on CSR popup
    4. Following CSR completion, remove lens cap
viii. Click “Capture”
ix. Click “OK”
x. **Camera is ready to image when desired flame and seed conditions have been met.**
    1. **Return to III. Operation to turn flame on**
    2. **Return to V. Particle Image Velocimetry (PIV) to seed flow**
xi. Click “Trigger” to record
    1. For images, “0” is when “Trigger” was clicked
xii. Click on “Play” tab
xiii. Click “Save Cine” to save
    1. Give the Cine an appropriate file name and location
    2. Set the range of frames to be saved
    3. Click “Save”
    4. Allow the save bar to finish saving before continuing

XIII. Flushing and Refilling the Dye Laser

a. Flushing

i. Drain existing dye out of the pumps using 1000 mL beaker (see Figure A.19)
ii. Tilt the pump, as practical, to aid in drainage
iii. Empty beaker with old dye into waste container using funnel
iv. Drain until leftover dye is gone
v. Attain Methanol from the Flame Locker in the COAL Lab
vi. Pour Methanol (roughly a few 100 mL’s)
vii. Open valve for the drain of the pump until clean Methanol can be seen exiting
viii. Close valves immediately so as to minimize methanol loss
ix. Use “Prime” switch for each pump independently to pump Methanol through the entire system
x. Repeat iv - ix until clean Methanol is observed in the entire system

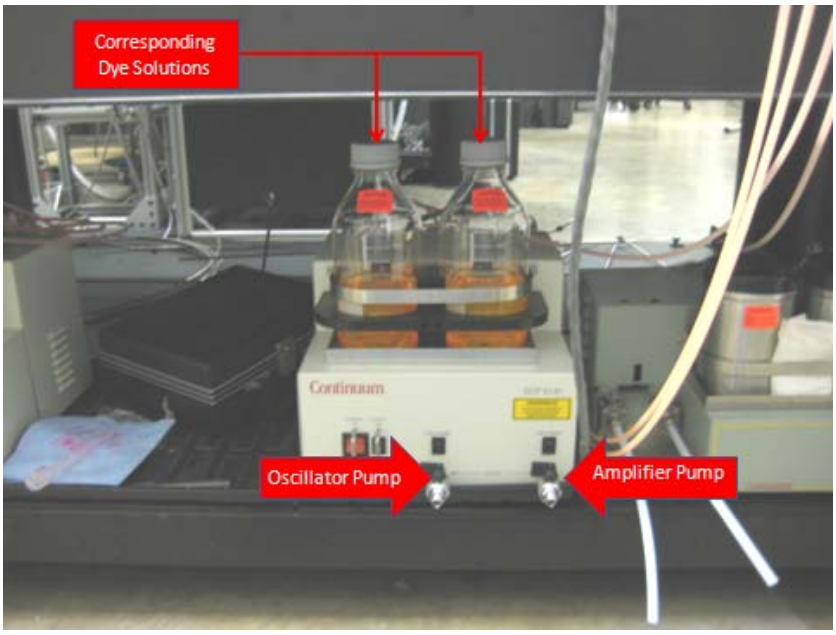

Figure A.19: Dye solution Oscillator and Amplifier reservoirs and pumps, below the Dye Lasers

b. Refilling

- **i.** Put 500 mL Methanol into each pump container (oscillator and amplifier pumps)
- **ii.** Drain until you see clean Methanol
- **iii.** Close valves immediately when clean Methanol is observed
- **iv.** Turn pumps on
- **v.** Attain dye concentrate from the Flame locker in the COAL Lab
- **vi.** **Mixing in the Dye**
  1. The dye is from a company called, *Exciton*
  2. They Recommend:
     - **a.** For oscillator: 120 mg/L (mg Dye Powder/Liter Methanol)
     - **b.** For amplifier: 50 mg/L
  3. **Use 500 mL for the dye laser so an adjustment is required:**
     - **a.** For oscillator: Start with 30 mL of concentrate
     - **b.** For amplifier: Start with 6 mL of concentrate
       - **i.** Add more dye carefully to both the oscillator and amplifier based on desired power output
- **vii.** Place a white business card in front of the first turning prism (see Figure A.13) coming out of the oscillator in order to monitor the color change of the laser beam (starts as green from the YAG, but as dye is added, becomes yellowish-green).
- **viii.** Remove card from in front of the first turning prism coming out of the oscillator and use it to view the beam at the exit of the laser.

ix. Adjust the doubling crystal alignment wheel (see Figure A.20) in order to better align the doubling crystal and create a more focused beam

1. Focus the blue beam (UV)

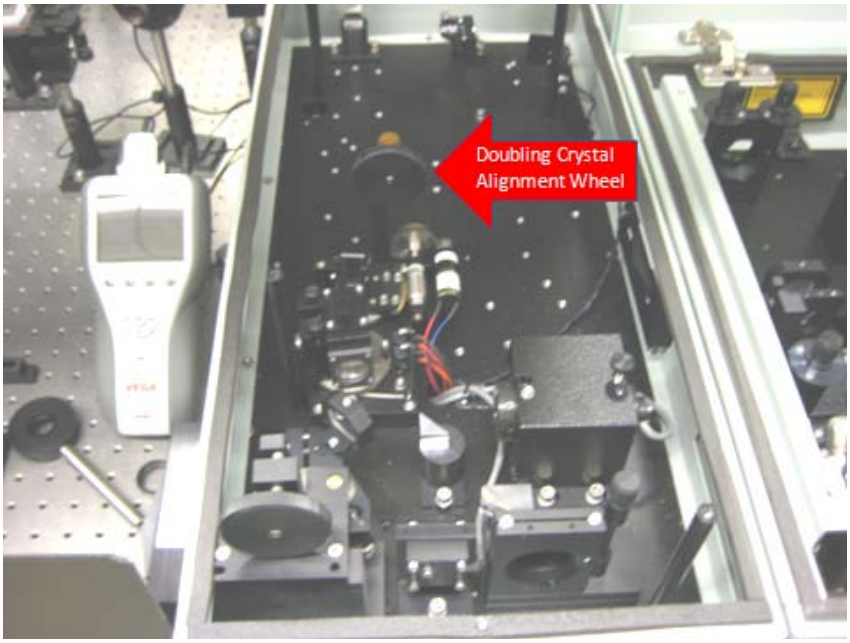

Figure A.20: Inside the dye laser, highlighted is the Doubling Crystal Alignment Wheel, used to focus the UV beam

x. Laser is ready for use

XIV. Final Shut – Down

a. Follow steps in either **V.** or **VI.** for the appropriate Laser **Shut- Down** procedure

b. Follow shut-down steps in **VII. Fuel Procedures (C_3H_8 – Propane)**

c. Follow shut-down steps in **VIII. Other Tank Farm Procedures**

d. In Labview

i. Close the three solenoids

1. Leave the Nitrogen solenoid on

ii. Ensure air flow rates are set to zero

iii. Ensure MFC's are off.

iv. Leave Main and Secondary Air solenoids **Open**

e. Shut off ventilation fans

f. Stop current Labview program.

g. Close Manual Valves on Primary and Secondary Air Lines.

h. Shut off Manual MFC's

i. Shut off "Equip" switch at Lab Control Station

XV. Calibration of Flow Controllers

a. Plug in the BIOS^{TM} Definer 1020 flow calibrator

i. If calibrating a flammable gas, connect nitrogen to the purge connectors as shown in Figure A.21

b. Connect the supply line to the sample inlet of the calibrator

c. Connect the exhaust line to the sample exhaust of the calibrator
d. Connect shop air (80 psig) to the back of the calibrator
e. Turn on the BIOS™ Definer 1020 calibrator and go to single sample
f. In the Labview program, enter in the desired flow amount
    i. Ensure the desired flow amounts cover the anticipated measurement range
g. Record the measured value from the calibrator
h. Once all of the desired flow amounts and the corresponding measure values have been record, create a trend line in Excel from the data
    i. The slope of the trend line is the new calibration constant
    ii. Take the slope and multiply the old calibration constant – giving the new Labview input

Figure A.21: BIOS™ Definer 1020 Flow Calibrator

XVI. California Analytical Instruments, Inc emissions measurements

a. Details about each of the analyzers can be found in their corresponding manuals
b. Prepare the facility to be run as according to the previous sections
    i. Open the calibration gases in the tank farm
c. Turn on the MOKON oil cooler
    i. Set temperature to 350 and allow to heat up
d. Turn on the CAI rack (power button at the top)
    i. Allow to warm up for at least 1 hour
        1. Temperature set points can be found in the analyzer manual
        2. Turn on the oven – set Temp control to 10
e. Open N_2 at the gas manifold on the Laboratory wall
    i. Flip the toggle switch on the bottom (back side) of the CAI rack for N_2 – this will purge the system during warm-up

ii. Turn hand valves to “zero”

f. After warm-up, open the remaining gases at the manifold on the Laboratory wall

i. Flip remaining toggle switches on the bottom (back side) of the CAI rack

g. Press the ignite button on the UHC analyzer

i. It may take several minutes for the analyzer to light and then reach operating temperature

h. If measure NO_X, press the NO/NO_X button on the analyzer

i. To calibrate

i. Set UHC and NO analyzers to zero or span

1. Zero will be set with N_2 and span is set with the calibration gas

ii. Turn hand valves to either “zero”, “span 1”, or “span 2”

1. Use the appropriate setting for calibrating either the span or zero set point for each analyzer

iii. Calibration gas concentrations can be found on the calibration gas certificates

iv. Calibrate every analyzer every two hours

j. To measure

i. Turn on rack pump (bottom located on top front of rack)

1. Adjust sample pressure to be 8-10 psig
2. Adjust sample sight glass so each sample is flow at 1 lpm

ii. Allow for sample to reach analyzers and stabilize (roughly 30-90 seconds)

iii. Can adjust sample location by moving the rig using the electronic translation stage (see Section X)

Appendix B: Flow Calibration Curves

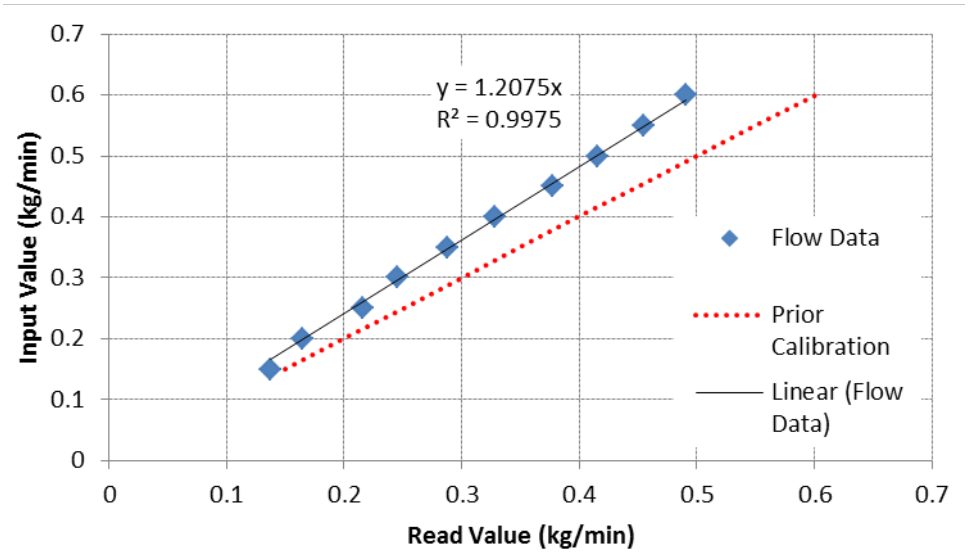

Figure B.1: Calibration curve for the core section air showing old calibration curve, the corrected calibration curve, and the correlation coefficient

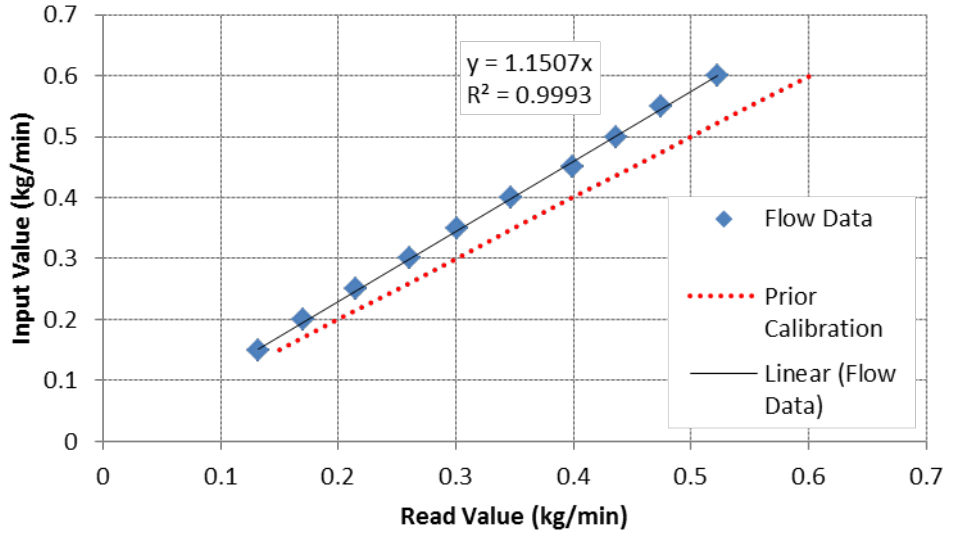

Figure B.2: Calibration curve for the UCC section air showing old calibration curve, the corrected calibration curve, and the correlation coefficient

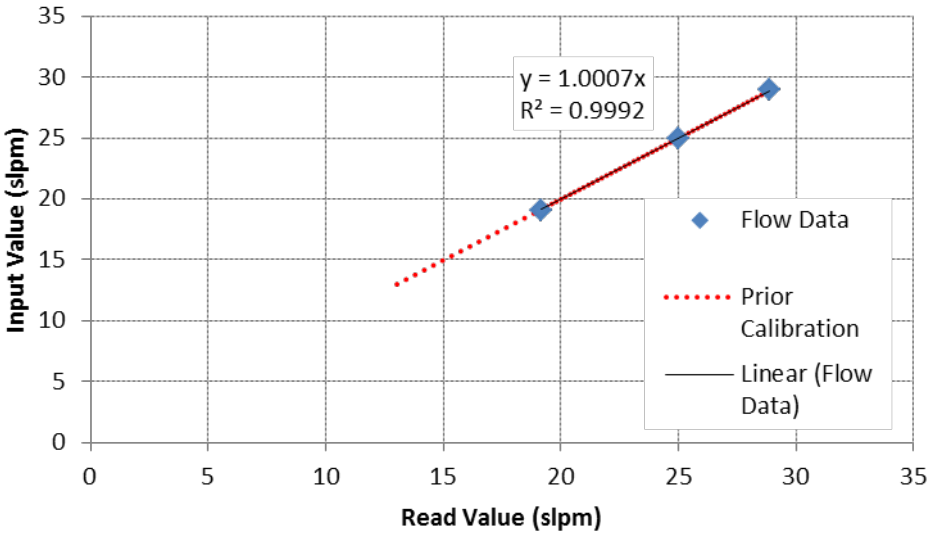

Figure B.3: Calibration curve for propane showing old calibration curve, the corrected calibration curve, and the correlation coefficient

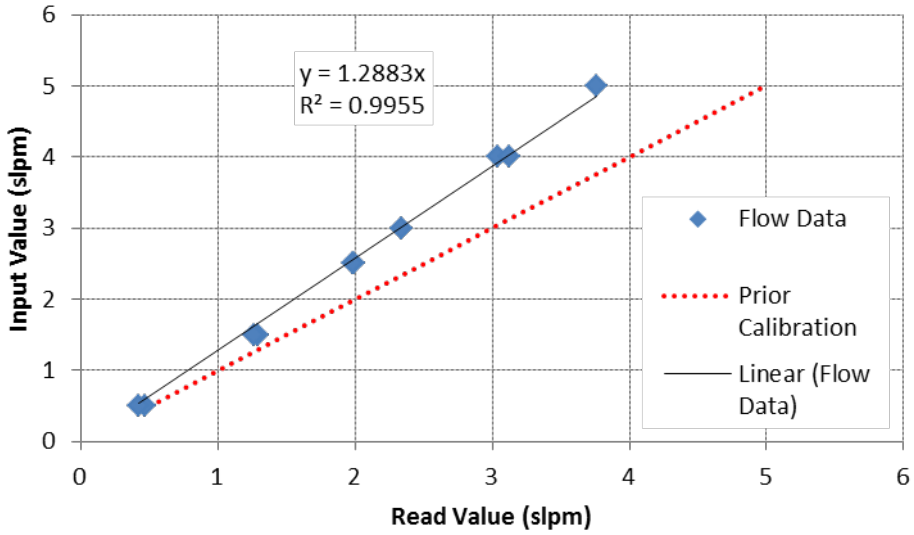

Figure B.4: Calibration curve for the igniter ethylene showing old calibration curve, the corrected calibration curve, and the correlation coefficient

Appendix C: MATLAB Analysis Code

```
%% Combination of rotating, cropping, calibration, image averaging, and
frequency analysis for HSV images

%close all; clear all; clc;
Y=1; N=0;

% Filename to be processed
filename = 'Case 4.tif';
FN = filename;
info = imfinfo(FN);

% Size of image, frequency of image capture, and number of images to be
processed
columns = 800;
rows = 200;
frequency = 5000;
% (Hz)
num_images = 4000;
% Number of images to be processed
fig = 1;

%% Choose Analysis Options

use_cal = N;
% Use calibration image file
use_image = N;
% Show image
use_inst = N;
% Show instantaneous image intensity
use_filter = N;
% Filter minimum and maximum signals
use_ave = N;
% Average image intensities
use_stdev = N;
% Compute standard deviation in image intensities
use_freq_vert = N;
% Compute frequency PSD analysis
use_freq_hor = N;
use_rot = N;

min_sig = 5;
% Minimal signal intensity for filtering
max_sig = 250;
% Maximum signal intensity for filtering

% Calibration file for the image to be processed
filename = 'Cal - UCC Core cavity.tif';
CAL = filename;
cal_info = imfinfo(CAL);
cal_images = numel(cal_info);
```

```
A = imread(CAL,1);

%% Show Calibration image for conversion of pixels to mm
if (use_cal == Y)
    figure(fig);
    imtool(A)
    axis equal;
    fig = fig + 1;
end
%% Complete the following information based on calibration image
inch = 4/(679 - 150);
% Using imtool, record the pixels associated with 1 inch (in/pixel)
spatial_cal = inch*25.4;
% Convert 1 inch to mm (mm/pixel)
dx = spatial_cal;
% (mm/pixel)
dy = spatial_cal;
% (mm/pixel)
rotate = atand(-2/(679-150));
% arctan(number of pixels up or down moved divided by number of
horizontal pixels) in degrees
location = 319;
% Location for strip of pixels to be used in the analysis.  Because the
frequency image is not flipped vertically, the pixel location (Rows and
Columns) shown in the calibration image are the location wanted for the
frequency analysis
close all
%% Convert pixels to length

x = zeros(1,columns); y = zeros(1,rows);
% Create x and y vector the length of the image dimensions
for i = 1:rows
    y(i) = (i-1)*dy;
% Convert pixels to length (height)
end
for j = 1:columns
    x(j) = (j-1)*dx;
% Convert pixels to length (width)
end

%% Open Video and save R+G+B in time @ location

images = zeros(rows,columns,3);
% Create 3 dimensional image matrix (y-direction, x-direction, number
of images)
z = zeros(rows,columns,3);
% Creates a 3 dimensional zero matrix
figure(fig)
if (use_image == Y)
    imshow(FN,1)
    fig = fig+1;
end

%% Rotate image
if (use_rot == Y);
    for k=1:num_images;
```

```
        z=imread(FN,k);
        z=imrotate(z,-rotate,'crop');
% Code to manually rotate image if image is tilted, negative rotates
clockwise, crops image to original size
        z1 = z(:,:,3);
        images(:,:,k) = z1;
    end
end
clear z;
x = x(1:columns);
y = y(1:rows);
figure(fig)
imagesc(x,y,images(:,:,1));
axis equal;
axis([0 max(x) 0 max(y)]);
set(gca,'YDir','normal');
colorbar
fig = fig +1;

%% Flip image vertically
use_flipv = Y;
% Flips image vertically
if (use_flipv == Y);
    for k = 1:num_images;
        z1 = images(:,:,k);
        images(:,:,k) = flipud(z1);
    end
    figure(fig)
    imagesc(x,y,images(:,:,1));
% Check to see if image is in correct orientation
    axis equal;
    axis([0 max(x) 0 max(y)]);
    set(gca,'YDir','normal');
    colorbar
    fig = fig +1;
end

%% Flip image horizontally
use_fliph = N;
% Flips image from left to right
if (use_fliph == Y);
    for k = 1:num_images;
        z1 = images(:,:,k);
        images(:,:,k) = fliplr(z1);
    end
    figure(fig)
    imagesc(x,y,images(:,:,1));
% Check to see if image is in correct orientation
    axis equal;
    axis([0 max(x) 0 max(y)]);
    set(gca,'YDir','normal');
    colorbar
    fig = fig +1;
end

%% Compute Time and Frequency Values
```

```
dt = 1/frequency;
t = (0:num_images-1)*dt;

%% Compute Time Average of Images
if(use_ave == Y)
    img_avg = zeros(rows,columns);
% Create zero matrix of image average
    img_avg = mean(images,3);
% Computes averages in time (3 denotes time)
end

%% Filter for Min Signal
if(use_filter == Y)
    for i = 1:rows
        for j = 1:columns
            if(img_avg(i,j) < min_sig)
                img_avg(i,j) = 0;
% If image intensity is less than the minimum signal, it is zeroed
            end
        end
    end
end
for i = 1:rows
    for j = 1:columns
        if(img_avg(i,j) > max_sig)
            img_avg(i,j) = 0;
% If image intensity is more than the maximum signal, it is zeroed
        end
    end
end

%% Compute Standard Deviation of Images
if(use_stdev == Y)
    img_std = zeros(rows,columns);
% Create zero matrix for image standard deviation

    for i = 1:rows
        for j = 1:columns
            img_std(i,j) = std(images(i,j,:));
% Computes standard deviation from the time average at each spatial
location
        end
    end
end

%% Output figures (For images from the side, up is +y-direction, left
to right is +x-direction, +z is into the page) (For images from above,
+z is up, left to right is +x-direction, -y-direction is into the page)

if(use_inst == Y)
    figure(fig);
    imagesc(x,y,images(:,:,1));
    axis equal;
    axis([0 max(x) 0 max(y)]);
```

```
    set(gca,'YDir','normal');
    xlabel('x position (mm)');
    ylabel('y position (mm)');

    fig=fig+1;
end

figure(fig);
imagesc(x,y,img_avg);
axis equal;
axis([0 max(x) 0 max(y)]);
set(gca,'YDir','normal');
xlabel('x position (mm)');
ylabel('y position (mm)');

fig=fig+1;


if(use_stdev == Y)
    figure(fig);
    imagesc(x,y,img_std);
    axis equal;
    axis([0 max(x) 0 max(y)]);
    set(gca,'YDir','normal');
    xlabel('x position (mm)');
    ylabel('y position (mm)');

    fig=fig+1;
end

%% Frequency Analysis for Vertical Strip

if (use_freq_vert == Y)
    TimeImage = zeros(rows,num_images);
% Create 2-D zero matrix to store strip of data over time
    for k = 1:num_images
        z = imread(FN,k);
        TimeImage(:,k) =
z(:,location,1)+z(:,location,2)+z(:,location,3);
        P(k) = k;
    end

    if (use_filter == Y)
% Filter for minimum signal
        for i = 1:rows
            for k = 1:num_images
                if(TimeImage(i,k) < min_sig)
                    TimeImage(i,k) = 0;
                end
            end
        end
    end

    df = (frequency)/num_images;
    f = (0:num_images-1)*df;
```

```
% Set frequency matrix
    FreqImage = fft2(TimeImage);

    for i = 1:rows
        for k = 1:num_images
            FreqImage(i,k) = FreqImage(i,k)*conj(FreqImage(i,k));
        end
    end

    profile = zeros(num_images,1);
    f_range = zeros(num_images,1);

    for k = 1:num_images
        profile(k) = mean(FreqImage(:,k));
        f_range(k) = (k-1)*df;
% Sets the frequency range based on the number of images and
acquisition frequency - basically the x-coordinate
    end

    profile = profile(2:.5*num_images);
% only showing have the frequency range due to not being able to
accurately detect frequencies at less than 2 times the acquisition
frequency and a discontinuity at 1 Hz
    f_range = f_range(2:.5*num_images);
% only showing have the frequency range due to not being able to
accurately detect frequencies at less than 2 times the acquisition
frequency and a discontinuity at 1 Hz

    profile = profile/max(profile);
% Normalizing the frequency profile based on the intensity of the most
common frequency

    %  (For images from the side, up is +y-direction, left to right is
+x-direction, +z is into the page)
    %  (For images from above, +z is up, left to right is +x-direction,
-y-direction is into the page)

    figure(fig);
    imagesc(P,y,TimeImage)
% Plots the intensity of the strip of interest versus time
    axis equal;
    axis([0 max(P) 0 max(y)]);
    set(gca,'YDir','normal');
    xlabel('Image Number');
    ylabel('y position (mm)');
    title('Strip intensity versus time');
    colormap(jet);
    colorbar;
    fig = fig +1;

    figure(fig);
% Should plot the FFT of the image
    imagesc(FreqImage);
    axis equal;
    axis([0 num_images 0 max(y)]);
```

```
    set(gca,'YDir','normal');
    xlabel('Frequency (Hz)');
    ylabel('y position (mm)');
    title('Strip frequency versus time');
    colormap(jet);
    colorbar;
    fig = fig +1;

    figure(fig)
% Plots the flame frequency observed in the flow
    plot(f_range,profile);
    xlabel('Frequency (Hz)');
    ylabel('Normalized Intensity');
    title('Most common flame frequency observed')
    fig = fig +1;
end

%% Frequency Analysis for Horizontal Strip
if (use_freq_hor == Y)
    TimeImage = zeros(num_images,columns);
% Create 2-D zero matrix to store strip of data over time
    for k = 1:num_images
        z = imread(FN,k);
        TimeImage(k,:) =
z(location,:,1)+z(location,:,2)+z(location,:,3);
        P(k) = k;
    end

    if (use_filter == Y)
% Filter for minimum signal
        for i = 1:columns
            for k = 1:num_images
                if(TimeImage(k,i) < min_sig)
                    TimeImage(k,i) = 0;
                end
            end
        end
    end

    df = (frequency)/num_images;
    f = (0:num_images-1)*df;
% Set frequency matrix
    FreqImage = fft2(TimeImage);

    for i = 1:columns
        for k = 1:num_images
            FreqImage(k,i) = FreqImage(k,i)*conj(FreqImage(k,i));
        end
    end

    profile = zeros(num_images,1);
    f_range = zeros(num_images,1);

    for k = 1:num_images
        profile(k) = mean(FreqImage(k,:));
```

```
        f_range(k) = (k-1)*df;
% Sets the frequency range based on the number of images and
acquisition frequency - basically the x-coordinate
    end

    profile = profile(2:.5*num_images);
% only showing have the frequency range due to not being able to
accurately detect frequencies at less than 2 times the acquisition
frequency and a discontinuity at 1 Hz
    f_range = f_range(2:.5*num_images);
% only showing have the frequency range due to not being able to
accurately detect frequencies at less than 2 times the acquisition
frequency and a discontinuity at 1 Hz

    profile = profile/max(profile);
% Normalizing the frequency profile based on the intensity of the most
common frequency

    %  (For images from the side, up is +y-direction, left to right is
+x-direction, +z is into the page)
    %  (For images from above, +z is up, left to right is +x-direction,
-y-direction is into the page)



    figure(fig);
    imagesc(P,y,TimeImage);
% Plots the intensity of the strip of interest versus time
    axis equal;
    axis([0 max(P) 0 max(y)]);
    set(gca,'YDir','normal');
    xlabel('Image Number');
    ylabel('z position (mm)');
    title('Strip intensity versus time');
    colormap(jet);
    colorbar;
    fig = fig +1;

    figure(fig);
% Should plot the FFT of the image
    imagesc(FreqImage);
    axis equal;
    axis([0 num_images 0 max(y)]);
    set(gca,'YDir','normal');
    xlabel('Frequency (Hz)');
    ylabel('z position (mm)');
    title('Strip frequency versus time');
    colormap(jet);
    colorbar;
    fig = fig +1;

    figure(fig)
% Plots the flame frequency observed in the flow
    plot(f_range,profile);
    xlabel('Frequency (Hz)');
    ylabel('Normalized Intensity');
```

```
    title('Most common flame frequency observed')
    fig = fig +1;
end
```

Bibliography

1. Mattingly, J. D., Heiser, W. H., Pratt, D. T., *Aircraft Engine Design*, AIAA, Reston, Virginia, 2002.

2. Zelina, J., Sturgess, G., Shouse, D., "The Behavior of an Ultra-Compact Combustor (UCC) Based on Centrifugally Enhanced Turbulent Burning Rates," 2004, AIAA-2004-3541.

3. Bohan, B., *Analysis of Flow Migration in an Ultra-Compact Combustor*, Master thesis, Air Force Institute of Technology, Wright-Patterson Air Force Base, Ohio, 2010.

4. Lewis, G. D., "Swirling Flow Combustors – Fundamentals and Applications," *Presented at AIAA/SAE 9th Propulsion Conference, Las Vegas, Nevada*, November 1973, AIAA-1973-1250.

5. Zelina, J., Sturgess, G., Hancock, R., "Ultra-Compact Combustors for Advanced Gas Turbine Engines," *Proceedings of ASME Turbo Expo '04*, June 2004, 2004-GT-53155.

6. LeBay, K., Polanka, M., Branam, R., "Characterizing the Effect of Radial Vane Height on Flame Migration in an Ultra Compact Combustor," *Proceedings of ASME Turbo Expo 2011*, June 2011, GT2011-45919.

7. Forney, A. K., "Engine Exhaust Emission Levels," *Journal of Aircraft*, Vol. 10, No. 12, 1973, pp. 716 – 719.

8. Kilpatrick, D. A., "Calculation Methodology for Basic Engine Exhaust Gaseous Emission Parameters," *National Gas Turbine Establishment Memorandum M81002*, February, 1981.

9. Society of Automotive Engineers (SAE), "Procedure for the Analysis and Evaluation of Gaseous Emissions from Aircraft Engines," *Aerospace Recommended Practice*, ARP1533, Warrendale, Pennsylvania, 1996.

10. Sirignano, W. A., Delplanque, J. P., Liu, F., "Selected Challenges in Jet and Rocket Engine Combustion Research," *33rd AIAA/ASME/SAE/ASEE Joint Propulsion Conference, Seattle, Washington*, 1997, AIAA-97-2701.

11. Anthenien, R. A., Mantz, R. A., Roquemore, W. M., Sturgess, G. J., "Experimental Results for a Novel, High Swirl, Ultra Compact Combustor for Gas Turbine Engines," 2nd Joint Meeting of the U.S. Sections of the Combustion Institute, Oakland, California, March, 2001.

12. Mawid, M.A, Thornburg, H., Sekar, B., Zelina, J., "Performance of an Inter-Turbine Burner (ITB) Concept with Three-Different Vane Cavity Shapes," *42nd AIAA/ASME/SAE/ASEE Joint Propulsion Conference and Exhibit, Sacramento, California*, July, 2006.

13. Anderson, W., Radtke, J., King, P., Thornburg, H., Zelina, J., Sekar, B., "Effects of Main Swirl Direction on High-g Combustion," *44th AIAA/ASME/SAE/ASEE Joint Propulsion Conference and Exhibit, Hartford, Connecticut*, July, 2008, AIAA-2008-4954.

14. Drenth, A. C., *Laser-Induced Fluorescence and Synthetic Jet Fuel Analysis in the Ultra Compact Combustor*, Master thesis, Air Force Institute of Technology, Wright-Patterson Air Force Base, Ohio, 2009.

15. Thomas, L. M., *Flow Measurements Using Particle Image Velocimetry in the Ultra Compact Combustor*, Master thesis, Air Force Institute of Technology, Wright-Patterson Air Force Base, Ohio, 2009.

16. Radtke, J.T., *Efficiency and Pressure Loss Characteristics of an Ultra-Compact Combustor with Bulk Swirl*, Master Thesis, Air Force Institute of Technology, Wright-Patterson Air Force Base, Ohio, 2007.

17. LeBay, K. D., *Characterization of Centrifugally-Loaded Flame Migration for Ultra-Compact Combustors*, Doctoral dissertation, Air Force Institute of Technology, Wright-Patterson Air Force Base, Ohio, 2011.

18. Turns, S. R., *An Introduction to Combustion*, McGraw-Hill, Inc., New York, 1996, 2nd Edition.

19. Baldouf, S., Shulz, A., Wittig, S., "High-Resolution Measurements of Local Effectiveness from Discrete Hole Film Cooling," *Journal of Turbomachinery*, Vol. 123, 2001.

20. Thole, K.A., Sinha, A.K., Bogard, D.G., and Crawford, M.E. "Mean Temperature Measurements of Jets with a Crossflow for Gas Turbine Film Cooling Application." *Proceedings of the Third International Symposium on Transport Phenomena and Dynamics of Rotating Machinery.* April, 1990.

21. Polanka, M.D., Zelina, J., Anderson, W.S., Sekar, B., Evans, D.S., King, P.I., Thornburg, H.J., Lin, C., Stouffer, S.D. "Heat Release in Turbine Film Cooling Part 1: Experimental and Computational Comparison of Three Geometries." *Journal of Propulsion and Power*, 2010.

22. Stojkovic, B.D., Fansler, T.D, Drake, M.C., Sick, V., "High-speed Imaging of OH* and Soot Temperature and Concentration in a Stratified-Charge Direct-Injection Gasoline Engine," *Proceedings of the Combustion Institute*, Vol. 30, Iss. 2, 2005.

23. Cross, C., Fricker, A., Shcherbik, D., Lubarsky, E., Zinn, B., "Dynamics of Non-Premixed Bluff Body-Stabilized Flames in Heated Air Flow," *Proceedings of ASME Turbo Expo 2010,* June 2012, GT2012-23059.

24. Cross, C., Lubarsky, E., Shcherbik, D., Bonner, K., Klusmeyer, A., Zinn, B., "Determination of Equivalence Ratio and Oscillatory Heat Release Distributions in Non-Premixed Bluff Body-Stabilized Flames Using Chemiluminescence Imaging," *Proceedings of ASME Turbo Expo 2011*, June 2011, GT2011-45579.

25. Venkata, N.N., Seitzman, J.M., "Chemiluminescence Measurements and Modeling in Syngas, Methane and Jet-A Fueled Combustors," *45th AIAA Aerospance Sciences Meeting, Reno, Nevada*, January, 2007, AIAA-2007-0466.

26. Anderson, W.S., *Design, Construction, and Validation of the AFIT Small Scale Combustion Facility and Sectional Model of the Ultra-Compact Combustor*, Master thesis, Air Force Institute of Technology, Wright-Patterson Air Force Base, Ohio, 2007.

27. Koether, S.J., *Validation of the AFIT Small Scale Combustion Facility and OH Laser-Induced Fluorescence of an Atmospheric Laminar Premixed Flame*, Master Thesis, Air Force Institute of Technology, Wright-Patterson Air Force Base, Ohio, 2007.

28. CHEMKIN™, CHMEKIN 10101, Reaction Design: San Diego, 2010.

29. Smith, G.P., Golden, D.M., Frenklach, M., Moriarty, N.W., Eiteneer, B., Goldenberg, M., Bowman, C.T., Hanson, R.K, Song, S., Gardiner, W.C., Lissianski, V.V., Qin, Z., *GRI-Mech 3.0*, February 2000, http://www.me.berkeley.edu/gri_mech/GriMECH 3.0 files.

30. Briones, A.M., Sekar, B., Thornburg, H., Zelina, J., "Effect of Vane Notch and Ramp Design on the Performance of a Rectangular Inter-Turbine Burner," *48th AIAA Aerospance Sciences Meeting, Orlando, Florida*, January, 2010, AIAA-2010-0581.

Vita

Captain Adam K. Parks graduated Greensburg Community High School in Greensburg, Indiana in 2003. Upon graduation, he attended the United States Air Force Academy to pursue a degree in Mechanical Engineering. In 2007, he completed his undergraduate work and was commissioned as a Second Lieutenant in the United States Air Force.

His first assignment was to the Air Force Research Laboratory at Wright-Patterson Air Force Base, Ohio. He was assigned to the Air Vehicles Directorate, Structures Division, Analytical Mechanics Branch as a developmental engineer. He worked on structural life enhancement and prediction through finite element analysis for current and future aircraft. He was married to Megan Marie Daihl on 18 January 2008. In August 2008, he received a permanent change of assignment to the Propulsion Directorate, Energy, Power, and Thermal Division, Fuels Branch where he worked as a fuels research engineer. His main focus was developing the ability for the Fuel Branch to fabricate research quantities of aviation quality synthetic fuel.

In August 2009, he entered the Graduate School of Engineering and Management at the Air Force Institute of Technology to pursue a Master's Degree in Aeronautical Engineering. Upon graduation, Captain Parks will return to the United States Air Force Academy, Colorado as an Engineering Mechanics Department Instructor.

REPORT DOCUMENTATION PAGE

Form Approved
OMB No. 0704–0188

1. REPORT DATE (DD–MM–YYYY)	2. REPORT TYPE	3. DATES COVERED *(From — To)*
22-03-2012	Master's Thesis	August 2010 – March 2012

4. TITLE AND SUBTITLE
Desensitizing Flame Structure and Exhaust Emissions to Flow Parameters in an Ultra-Compact Combustor

5a. CONTRACT NUMBER
5b. GRANT NUMBER
5c. PROGRAM ELEMENT NUMBER

6. AUTHOR(S)
Adam K. Parks, Capt, USAF

5d. PROJECT NUMBER
5e. TASK NUMBER
5f. WORK UNIT NUMBER

7. PERFORMING ORGANIZATION NAME(S) AND ADDRESS(ES)
Air Force Institute of Technology
Graduate School of Engineering and Management (AFIT/ENY)
2950 Hobson Way
WPAFB OH 45433-7765

8. PERFORMING ORGANIZATION REPORT NUMBER
AFIT/GAE/ENY/12-M33

9. SPONSORING / MONITORING AGENCY NAME(S) AND ADDRESS(ES)
AFRL/RZTC
Dr. Joseph Zelina
joseph.zelina@wpafb.af.mil
(937) 255-7487
Bldg 490, Rm 116,
1790 Loop Road, N
Wright-Patterson AFB, OH 45433

10. SPONSOR/MONITOR'S ACRONYM(S)
AFRL

11. SPONSOR/MONITOR'S REPORT NUMBER(S)

12. DISTRIBUTION / AVAILABILITY STATEMENT
APPROVED FOR PUBLIC RELEASE; DISTRIBUTION UNLIMITED

13. SUPPLEMENTARY NOTES This material is declared a work of the U.S. Government and is not subject to copyright protection in the United States.

14. ABSTRACT

A major thrust of turbine engine research is to improve both efficiency and thrust-to-weight ratio of the engine. A promising solution to this challenge is the Ultra-Compact Combustor (UCC). The UCC shortens the axial length of the combustor by performing combustion circumferentially on the outer diameter of the engine. The reduction in axial length yields significant weight savings and increases the thrust-to-weight ratio. The design also increases combustion efficiency by performing the combustion in a centrifugally loaded environment which allows unreacted particles to remain in the combustor sufficiently long enough to become combustion products. The Air Force Institute of Technology (AFIT) and the Air Force Research Laboratory (AFRL) have been jointly researching the fundamental dynamics of the UCC. To aid in integrating the UCC into a turbine engine, the current objective is to desensitize the exhaust characteristics of the combustor to changes in operating parameters. The following report documents modifications to the AFIT sectional test rig to improve its replication of the AFRL full annulus. High speed video was captured to document flame shape, location, intensity, and stability within the core section. Carbon monoxide, carbon dioxide, oxygen, nitrous oxides, and unburnt hydrocarbon emissions measurements were recorded to quantify the combustors exhaust constituents. A novel vane concept was implemented to desensitize the flame shape, location, intensity, and its exhaust products with changes in operating parameters. The design represents the next step toward creating a UCC vane that can migrate the flow effectively and consistently from the UCC cavity into the core flow. Furthermore, this vane concept represents the first attempt at a design that can be effectively cooled for application in a realistic turbine engine.

15. SUBJECT TERMS
Combustion, Combustor, Experimental, High Speed Video, Emissions, Ultra-Compact Combustor

16. SECURITY CLASSIFICATION OF:			17. LIMITATION OF ABSTRACT	18. NUMBER OF PAGES	19a. NAME OF RESPONSIBLE PERSON
a. REPORT	b. ABSTRACT	c. THIS PAGE			Dr. Marc D. Polanka, ENY
U	U	U	UU	178	19b. TELEPHONE NUMBER (Include Area Code) (937)255-3636, ext 4714

Standard Form 298 (Rev. 8–98)
Prescribed by ANSI Std. Z39.18